SCIENCE ▪ PASSION ▪ TECHNOLOGY

TU Graz

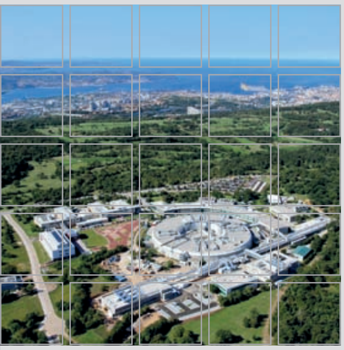
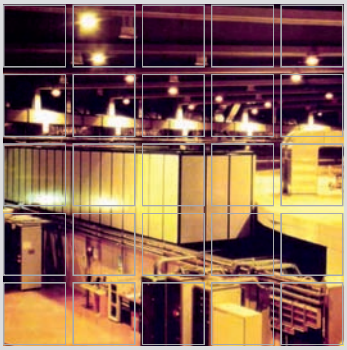
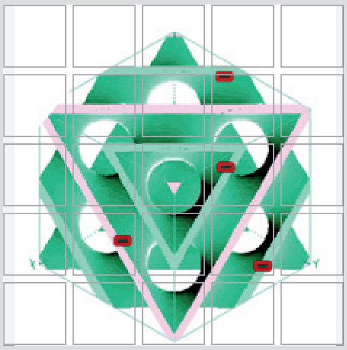
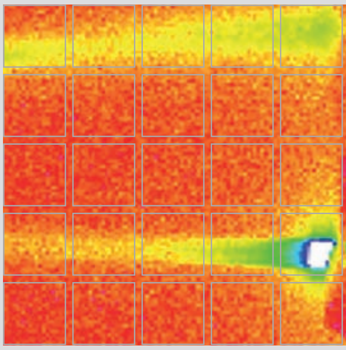

TCVB


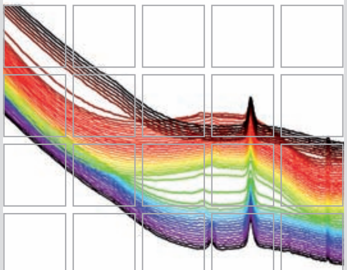
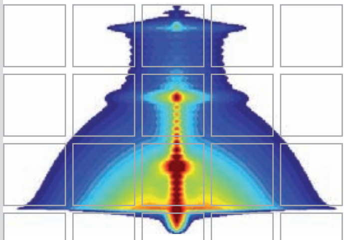

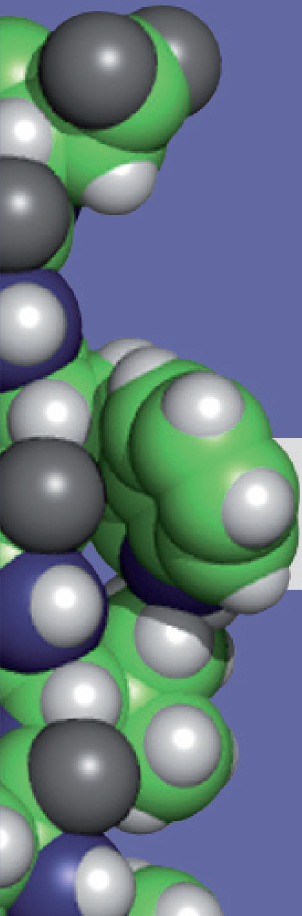

ANNUAL REPORT 2012

Austrian SAXS Beamline at Elettra Sincrotrone Trieste

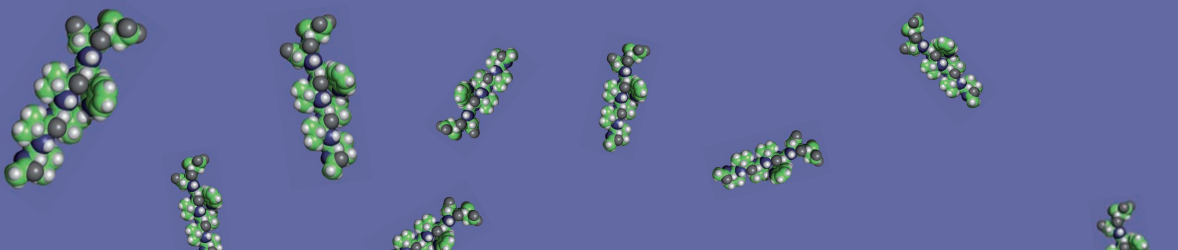

Austrian Small Angle X-ray Scattering (SAXS) Beamline at ELETTRA

Annual Report 2012

Compiled by Sigrid Bernstorff & Heinz Amenitsch

Cover pictures taken from the user contributions:

K. Kornmueller et al., pages 84-85 (front cover: background picture, and middle-right down)

A. Yaghmur et al., pages 95-97 (front and back cover: middle-right up)
A. Pinna et al., pages 105-106 (front cover: right up)
V. Valeš et al., pages 68-69 (front and back cover: right down)
P. Dubček et al., pages 48-49 (back cover: right up)
N. Akhtar et al., pages 41-43 (back cover: middle right down)

Table of Contents

› **Preface**

› **Experimental Possibilities at the SAXS-beamline**

› **User Contributions**

Preface

Frank Uhlig
Dean of
Institute for Inorganic Chemistry,
Graz University of Technology

2012 was the year of great changes and therefore also a year of great challenges for the Austrian Beamlines at ELETTRA. The last few months before transfer to the Graz University of Technology took place were months of uncertainty for all the people of the former Institute Biophysics and Nanosystems Research of the Austrian Academy of Sciences. Nevertheless, with the final step in October 2012 by the signing their new contracts as now employees of the Institute for Inorganic Chemistry of the TU Graz the process came to a successful and satisfying end.

However, the transfer to the Graz University of Technology carries also its own opportunities, new environment, new colleagues, and thus new scientific challenges resulting finally into new projects. I´m sure the team in Triest will handle all these new challenges highly motivated and highly committed. As Graz University of Technology we are able to significantly increase the quality of the scientific equipment and hence the quality of the scientific output of the Austrian Beamlines at ELETTRA in the near future.

I want to thank especially our Italian partners at ELETTRA for their outstanding support during the above mentioned transitional period. For all of the former users as well as all potential users of the future I´d like to point out, that also with the “new management” we, as Graz University of Technology, will do everything to retain the ranking of both, the SAXS beamline and Deep X-ray Lithography beamline, in the leading group of the synchrotron community worldwide.

Alfonso Franciosi
Chief Executive Officer
Elettra-Sincrotrone Trieste S.C.p.A.

It is a real pleasure to welcome the Technical University of Graz (TUG) among the main partners of our institution. On November 21, 2013, new formal agreements between TUG and Elettra have been signed transferring responsibility for the Austrian programs involving the SAXS and DXRL beamlines at Elettra from the Austrian Academy of Sciences to TUG. Elettra has now found a new and enthusiastic partner in TUG and looks forward to a fruitful collaboration in the years to come. In the past three years Austrian researchers have achieved an 80% success rate in their beamtime applications at Elettra, a score that almost doubles the average success rate and that is among the highest of any national research community at Elettra. This testifies both to the quality of Austrian science, and to the effectiveness of the SAXS personnel service to the Austrian community. More than 130 publications in prestigious international journals in the last three years resulted from this.

Last year the users of Elettra were able to take full advantage of the increase in machine stability and reproducibility resulting from the top-up operating mode, the realignment of all magnetic components and the introduction of beam-based alignment. In particular, the increase in thermal stability of the different machine components deriving from the full-energy injection yielded a drastic reduction in component failures. The overall machine uptime reached 96.1%, the highest ever recorded at Elettra. The new beam-based alignment system was routinely used to control the electron beam position with a relative accuracy of 10 microns. The circulating current at 2.4 GeV was successfully increased by 33% to 200 mA thanks to a number of improvements in the vacuum chamber cooling system.

The superconductive wiggler that will provide photon energies up to 25 keV to the second diffraction beamline for structural biology (XRD2) and the new beamline for high pressure diffraction studies (XPRESS) - under construction in collaboration with the Indian Institute of Science in Bangalore - was refurbished to make it compatible with top-up operations and successfully tested on the storage ring. The development of XRD2 and XPRESS, together with the implementation of the new x-ray fluorescence beamline in collaboration with the International Atomic Energy Agency, will substantially extend the range of facilities available to Elettra users.

In the last year the FERMI project attained a number of ambitious goals. The FEL-1 laser line achieved and surpassed the design specifications thanks to the implementation of the X-band fourth harmonic linearization system together with the laser heater, which allowed a substantial increase in the charge stored within the electron bunches. Peak currents of 500-600 A were achieved with a constant time profile of a typical 500 fs duration. This, together with the exploitation of the two new high-energy RF deflectors to optimize the electron trajectories, enabled FEL-1 to achieve energies of several hundreds μJ/pulse. Design specifications for FEL-1 where achieved or surpassed throughout the operating wavelength range and down to the minimum design wavelength of 20 nm, and useful intensities from FEL-1 were produced down to 10 nm.

The FEL-1 facility was officially opened to external users and - as a result of the first two calls - a total of 75 proposals were received from 14 countries. Based on the proposal assessment by the international FERMI peer-review panel, beamtime was allocated to 34 proposals. Several users have indicated that the intensity, wavelength and linewidth stability of FERMI made their experience in Trieste the best ever for them at any FEL facility worldwide.

Commissioning of the two-stage FEL-2 facility, designed to cover the 20-4 nm wavelength range, was expected to be a more complex task than commissioning of the single-stage FEL-1. Also, it could be performed only during the shutdown periods of the FEL-1 user facility. However, first coherent radiation for the first stage of FEL-2 was obtained at 52 nm in May 2012. Coherent radiation from the second stage was obtained at 14.4 nm in October 2012, corresponding to the sixth harmonic of the seed laser (43 nm) in the first stage seeding the second stage at the third harmonic, using the same electron bunch, but a portion of the bunch that was not involved in the first stage seeding process, thanks to a delay line.

The validity of such a technique, denominated Double Stage Cascade High Gain Harmonic Generation (HGHG) with fresh bunch technique, was demonstrated for the first time worldwide in the EUV range at FERMI. Intensities up to 50μJ/pulse were obtained at 10.8 nm (using the 8th harmonic of the seed laser in the first stage and the 3rd harmonic of the first stage radiation in the second stage. Shorter wavelengths will require routine linac operations at 1.5 GeV, which has just been achieved.

An important recent institutional development was the approval of the Central European Research Infrastructure Consortium (CERIC) by the European Research Infrastructure Consortium (ERIC) Committee of the European Commission. The ERIC legal framework has been designed to facilitate the establishment and operation of research infrastructures of European interest with the involvement of several European countries. An ERIC is a legal entity with legal personality and full legal capacity recognised in all EU Member States. It should be noted that the ERIC is a legal tool which is appropriate only for high-profile research infrastructures with a European dimension. Therefore, only a limited number of ERICs are expected to be set up in the coming years.

CERIC will be a distributed research facility, proposed as an ERIC by nine Countries (Austria, Croatia, Czech Republic, Hungary, Italy, Poland, Romania, Serbia, Slovenia), but open to users from all other interested countries. Its goals will be to support excellent research in the field of nanolevel analysis and synthesis of materials while at the same time speeding-up the alignment between Eastern and Western EU countries. The initial statutory seat will be in Trieste at Elettra and CERIC activities will be based on in-kind contributions from the Partner Facilities designated by the Member States.

The Italian contribution will be based on the Elettra laboratory, and will initially provide access to X-ray Diffraction and Absorption beamlines, to IUVS as well as to X-ray microscopy beamlines, which are complementary to the foreseen contributions by other partners. The Austrian contribution will be based on instrumentation owned by the TUG, namely the SAXS Beamline at Elettra and a national support laboratory in Graz consisting of a complete sample preparation and offline characterization laboratory (Dynamic Light Scattering, offline SAXS, etc.).

The Czech contribution is foreseen to be the Materials Science Beamline at Elettra, run by a research group of the Charles University, together with a national support laboratory in Prague consisting of a complete surface science laboratory (XPS, STM, DLEED, SIMS). The Slovenian contribution was selected at the national level and will be based on the NMR center in Ljubljana, which offers, among others, protein structural determination, complementary to small angle scattering (SAXS and SANS) and to x-ray diffraction methods.

The Hungarian contribution is foreseen to be initially based on a set of instruments at the Budapest Neutron Cente including the Small Angle Neutron Scattering (SANS) facility (complementary to SAXS), the Prompt Gamma Activation Analysis, PGAA, the Neutron-Induced Prompt-gamma Spectroscopy (NIPS) and the GINA polarized-neutron reflectometer. The Romanian contribution is foreseen to start with a set of instruments at the National Center for Materials Physics (INFIM), including two state of the art Trasmission Electron Microscopes (TEM) with subnanometer resolution (complementary to diffraction and to x-ray microscopy), a campus XAFS apparatus and an Electron Spin resonance facility. Discussions are ongoing with Poland and Croatia to define the corresponding CERIC Partner Facilities. Serbia is expected to invest a large amount of EU structural funds for a major nanotechnology center.

Elettra and TUG, with their well-established framework of collaborations, will have to show the way to the other CERIC partners. CERIC is to offer to the international user community a common entry point for the available services, so that interested users will be able to apply for access to several complementary analytical, processing and nanofabrication techniques with a single proposal. A single evaluation system will be put in place to provide free and open access by quality selection only. Challenges include to become globally attractive and offer unique services, increase EU and national value by introducing direct cooperation and global competition, learn how to account for real costs and be transparent for different uses (VAT, industry, governments, EU), coordinate new investments and upgrades with complementarity in mind, and develop joint IPR, industrial, educational, communication and development activities.

Some of the new strategic directions opening up for us and for our partners will be addressed by the thematic workshops that will take place as part of the XXI Elettra Users' Meeting: "Coherent x-ray spectroscopy: the dream", and "New challenges for research on graphene: from growth and state-of-the-art characterization towards industrial applications". Such workshops will serve the purpose of engaging a broader user community, and our partner institutions will have prominent roles in the above events.

We take this opportunity to thank our Austrian partners for their professionalism and steady dedication over the years. We at Elettra look forward to expanding the scope and depth of our collaboration and exploring together the frontiers that the new upgraded Elettra, FERMI and CERIC will open for all of us.

The SAXS Group

SCIENTISTS: Heinz Amenitsch 1)

e-mail: amenitsch@elettra.eu

Sigrid Bernstorff 2)

e-mail: bernstorff@elettra.eu

Benedetta Marmiroli 1)

e-mail: benedetta.marmiroli@elettra.eu

Michael Rappolt 1)

e-mail: michael.rappolt@elettra.eu

POST DOCS: Fernando Cacho 1)

e-mail: fernando.cacho@elettra.eu

SCIENTIFIC ASSISTANT: Barbara Sartori 1)

e-mail: barbara.sartori@elettra.eu

TECHNICIAN: Christian Morello 2)

e-mail: christian.morello@elettra.eu

1) Until 30.9.2012: Institute for Biophysics and Nanosystems Research, Austrian Academy of Sciences, Schmiedlstraße 6, 8042 Graz, Austria

Since 1.10.2012: Institute of Inorganic Chemistry, Graz University of Technology, Faculty of Technical Chemistry, Chemical and Process Engineering, Biotechnology - TCVB, Stremayrgasse 9/IV, 8010 Graz, Austria
Tel 0043-316-873 32145
Fax 0043-316-873 32102
WEB: http://ac.tugraz.at

and: Institute Outstation c/o Elettra - Sincrotrone Trieste

2) Elettra - Sincrotrone Trieste, Strada Statale 14, km 163.5, 34149 Basovizza (TS), Italy
Tel 0039-040-375 8572
Fax 0039-040-938 0902
Web: www.elettra.eu

The SAXS-Beamline in General

Small Angle X-ray Scattering has become a well known standard method to study the structure of various objects in the spatial range from 1 to 1000 Å, and therefore instruments capable to perform such experiments are installed at most of the synchrotron research centers. The high-flux SAXS beamline at ELETTRA is mainly intended for time-resolved studies on fast structural transitions in the sub-millisecond time region in solutions and partly ordered systems with a SAXS-resolution of 10 to 1400 Å in real-space.
The photon source is the 57-pole wiggler whose beam is shared and used simultaneously with a Macromolecular Crystallography beamline. The wiggler delivers a very intense radiation between 4 and 25 keV of which the SAXS-Beamline accepts 3 discrete energies, namely 5.4, 8 and 16 keV. The beamline optics consists of a flat double crystal monochromator and a double focusing toroidal mirror.
A versatile SAXS experimental station has been set-up, and an additional wide-angle X-ray scattering (WAXS) detector monitors simultaneously diffraction patterns in the range from 1 to 9 Å. The sample station is mounted move-able onto an optical table for optimising the sample detector distance with respect to SAXS resolution and sample size.
Besides the foreseen sample surrounding the users have the possibility to install their own specialised sample equipment. In the design phase, besides technical boundary conditions, user friendliness and reliability have been considered as important criteria.
The optimisation of the beamline with respect to high-flux and consequently high flux density, allows to perform the following experiments:

- Low Contrast Solution Scattering
- Grazing Incidence Scattering and Surface Diffraction
- Micro-Spot Scanning
- X-ray Fluorescence Analysis
- Time-Resolved Studies ≥ 11 μs
- Simultaneously Performed Small- and Wide-Angle Measurements (SWAXS) on:
    - Gels
    - Liquid Crystals
    - (Bio) Polymers
    - Amorphous Materials
    - Muscles

Furthermore, using 5.4 and 16 keV energies, the beamline is widely applicable also to very thin, e.g. single muscle fibers, and optically thick (high Z) specimen, as often used in e.g., material science and solid state physics.

THE INSERTION DEVICE

The wiggler for the SAXS beamline consists of three 1.5 m long segments, each having 19 poles. The device can work with a minimum gap of 20 mm, which corresponds to K=20 at 2 GeV. The main parameters of the wiggler are:

- Critical Energy 4.1 keV
- Radiation Power 8.6 kW
- Flux 3.5×10^{14} ph/s/mrad/0.1%BW (at 400 mA)

The wiggler radiation cone has a horizontal width of 9 mrad. From this the SAXS-beamline accepts vertically 0.3 mrad, and horizontally +/-0.5 mrad at a 1.25 mrad off-axis position. The resulting source size for 8 keV photons is 3.9 x 0.26 mm^2 (horiz. x vert.).

THE OPTICS

The optics common with the diffraction beamline consists of:

- C-Filter and Beryllium window assembly to reduce the power load on the first optical elements by a factor of 2 and to separate the beamline vacuum from the storage ring.
- Beam defining slit chamber which allows to define the SAXS beam on three sides before the monochromator in order to reduce the straylight in the downstream beamline sections.

The SAXS beamline optics consists of:

- A double-crystal monochromator consisting of four individual chambers, in which three interchangeable asymmetric Si(111) crystal pairs are used to select one of three fixed energies. Each of the crystal pairs is optimised for the corresponding energy to accomplish a grazing angle of 2°. The energy resolution $\Delta E/E$ of the monochromator is in the range of 0.7 - 2.5 10^{-3}.
- A baffle chamber after the monochromator is used as an adjustable straylight fenditure.
- A segmented toroidal mirror focuses the light in horizontal and vertical direction with a 1/2.5 magnification onto the SAXS-detector.
- An aperture slit reduces the straylight after the monochromator and the toroidal mirror.
- A guard slit defines the illuminated region around the focal spot. The spot size on the detector is 1.6 mm horizontally and 0.6 mm vertically. The calculated flux at the sample is in the order of 10^{13} ph/s at 400 mA. For a maximum sample size of 5.4 x 1.8 mm^2 correspondingly a flux density of 10^{12} ph/s/mm^2 has been calculated.

SAMPLE STAGE

The multipurpose sample stage allows to perform fast time-resolved relaxation studies based on temperature- or pressure-jumps as well as stopped flow experiments. Shear jump relaxation experiments are planned. Specifically, T-jumps can be induced by an infra-red light pulse (2 ms) from an Erbium-Glass laser, raising the temperature about 20 °C in an aqueous sample volume of 10 μl. A hydrostatic pressure cell with a maximal accessible angular range of 30° for simultaneous SAXS and WAXS measurements is available. P-jumps are realised by switching fast valves between a low and a high pressure reservoir, increasing or decreasing the hydrostatic pressure in the range from 1 bar to 2.5 kbar within a few ms. A Differential Scanning Calorimeter (DSC) allows for DSC-scans simultaneously to SWAXS measurements. In an overview, the following sample manipulations are possible (for further details, see pages 30-38):

- Temperature Manipulations: Ramps, Jumps and Gradient Scans
- Pressure Manipulation: Scan and Jumps
- Stopped Flow Experiments
- SWAXS Measurements Applying Mechanical Stress
- Calorimetric measurements

<table>
<tr><td>Scientific Applications</td><td>Low Contrast Solution Scattering, Grazing Incidence Surface Diffraction, Micro-Spot Scanning, X-ray Fluorescence Analysis, Time-Resolved Studies $\geq 11\ \mu s$ and Simultaneously Performed Small- and Wide-Angle Measurements (SWAXS) on:
Gels
Liquid Crystals
(Bio) Polymers
Amorphous Materials
Muscles</td></tr>
<tr><td>Source characteristics</td><td>Wiggler (NdFeB Hybrid):
<table>
<tr><td>Period</td><td>140 mm</td></tr>
<tr><td>No. full poles</td><td>57</td></tr>
<tr><td>Gap</td><td>20 mm</td></tr>
<tr><td>B_{max}</td><td>1.607 T</td></tr>
<tr><td>Critical Energy ε_c</td><td>4.27 keV</td></tr>
<tr><td>Power (9 mrad)</td><td>8.6 kW</td></tr>
<tr><td>Effective source size FWHM</td><td>3.9 x 0.26 mm^2(h x v)</td></tr>
</table></td></tr>
<tr><td>Optics</td><td>
<table>
<tr><td>Optical elements:</td><td><i>Double crystal monochromator</i>:
Si (111) asym. cut, water cooled.</td><td><i>Mirror</i>:
two–segment,toroidal, Pt coated.</td></tr>
<tr><td>Distance from source:</td><td>18.4 m</td><td>26.5 m</td></tr>
</table>
<table>
<tr><td>Acceptance</td><td>1 mrad/0.3 mrad (h x v)</td></tr>
<tr><td>Energy (3 selectable)</td><td>5.4, 8, 16 keV (0.77, 1.54, 2.3 Å)</td></tr>
<tr><td>Energy resolution $\Delta E/E$</td><td>0.7-2.5 x 10^{-3}</td></tr>
<tr><td>Focal spot size FWHM</td><td>1.2 x 0.6 mm^2 (h x v)</td></tr>
<tr><td>Spot at Sample FWHM</td><td>5.4 x 1.8 mm^2(h x v)</td></tr>
<tr><td>Flux at sample</td><td>7.5 x 10^{12} ph s^{-1}(2 GeV, 300 mA, 8 keV)</td></tr>
</table></td></tr>
<tr><td>Experimental apparatus</td><td>Resolution in real space: 10-1400 Å (small-angle), 1- 9 Å (wide-angle)

Sample stage: temperature manipulations: ramps, jumps and gradient scans, pressure manipulation: scan and jumps, stop flow experiments, SWAXS measurements applying mechanical stress, SWAXS measurements applying magnetic fields. In-line calorimetric measurements simultaneously with SWAXS.

Detectors: 1D gas-filled detectors for simultaneous small- and wide-angle (Gabriel type), 2D CCD (Photonic Science) and Mar300 Image Plate for small-angle, Vantec-1D (Bruker AXS), Pilatus 2D detector.</td></tr>
<tr><td>Experiment control</td><td>Beamline control: Program-units written in LabView for Windows
1 D detector control: PC-card and software from Hecus X-ray Systems GmbH, Graz.
2 D detector control: Software from corresponding detector system.</td></tr>
</table>

CURRENT STATUS

The beamline has been built by the Institute for Biophysics and Nanosystems Research (IBN), Austrian Academy of Science in collaboration with staff members from Sincrotrone Trieste, and is in user operation since September 1996. The set-up of the beamline started at the beginning of January 1995 with the installation of the support structure. Until the end of 1995, the 8 keV single energy system had been realised. The upgrade to the full three energy system was finished in spring 1998. Time resolved experiments require fast X-ray detectors and data acquisition hard- and software. Depending on the desired resolution in time and in reciprocal space, on isotropic or anisotropic scattering of the sample, one-dimensional position sensitive (delay-line type) or two-dimensional CCD detectors are employed.

In August 2002 our chemistry and X-ray laboratory went into operation. The chemistry unit serves mainly for sample preparation and analysis for both, in house research and external user groups, whereas the X-ray laboratory allows on-site testing of samples before moving on to the SR beamline (see page 38).

In May 2008 we extended about 3 m also our experimental hutch. It is now possible to increase the sample to detector distance and therefore improve our minimum SAXS resolution or maximise the flux density at sample position for certain experiments.

On 1st October 2012 the beamline was transfered from the Institute of Biophysics and Nanosystems Research, Austrian Academy of Sciences, to the Institute of Inorganic Chemistry, Graz University of Technology.

Application for Beamtime at ELETTRA

1. Beamtime Policy at SAXS beamline

According to the agreement from March 2001 regarding the co-operation between the Austrian Academy of Sciences and Sincrotrone Trieste, at the Austrian SAXS-beamline the available beamtime of about 5000 hours/year is distributed as follows:

- 35% for Austrian Users, type: "CRG" (Collaborating Research Group)
- 35% for Users of Sincrotrone Trieste (General Users (GU))
- 30% is reserved for beamline maintenance and in-house research

In both user beamtime contingents also any industrial, proprietary and confidential research can be performed according to the "General User Policy" of Sincrotrone Trieste.

To apply for CRG and GU user beamtime proposals must be submitted according to the rules of Sincrotrone Trieste. The international review committee at ELETTRA will rank the proposals according to their scientific merit assessment. Based on this decision beamtime will be allocated according to the specific quotes for the beamtimes (CRG/GU) either for the following semester ("normal application") or for the next two years ("long term application"). However, at the moment no more than a maximum of 10% of the beamtime will be assigned to "long term" projects.

2. How to apply for beamtime

There are two deadlines each year for proposals, namely August 31st and February 28th. Accepted proposals will receive beamtime either in the then following first or second half year period, respectively. The Application Form must be completed on-line according to the following instructions.

ELETTRA USERS OFFICE
Strada Statale 14 - km 163.5
34012 Basovizza (Trieste), ITALY
Tel: +39 040 375 8628 / 8538- fax: + 39 040 375 8565
e-mail: useroffice@elettra.trieste.it

INSTRUCTIONS GIVEN BY THE USERS OFFICE

(see also http://www.elettra.trieste.it/userarea/apbt.html)

1. Read carefully the General Guidelines.

2. Connect to the Virtual Unified Office: https://vuo.elettra.trieste.it/pls/vuo/guest.startup using your favorite browser with JavaScript enabled.

3. Select the Virtual Unified Office link. Login with your ID and password. If you are a new user fill in the registration form with your data and choose your institution with the search button; in case your institution does not appear in the list, please contact useroffice@elettra.trieste.it giving all the details about it. When registered, you will receive an acknowledgment with your ID and password. You can change your password, if you wish. In case you forget your password, please don't register again but contact useroffice@elettra.trieste.it. At any moment you can select the help button and view more detailed instructions. By inserting your ID and password you will be able to continue.

4. Select the proposals button in the User functions group.

5. Select add and fill in on-line the proposal form. Please, type your proposal in English. Repeat this procedure for each proposal you intend to submit.

6. In case of continuation proposal: a) attach the experimental report of previous measurements; b) give your previous proposal number.

7. When finished, submit the proposal electronically, selecting the save button.

8. Print all safety forms (related to your proposal form).

9. Sign the safety form(s).

10. Mail all printed and signed safety form(s) to the (real) Users Office.

NOTE:

For administrative questions related to the proposal submission, contact useroffice@elettra.trieste.it

For scientific or technical questions related to the possibility of performing a given experiment, contact bernstorff@elettra.eu or amenitsch@elettra.eu

Users and institutes performing experiments in 2012

Australia

Commonwealth Scientific and Industrial Research Organisation (CSIRO), Division of Materials Science & Engineering, Clayton South MDC, Victoria

FALCARO Paolo

Austria

Laboratory of Polymer Engineering LKT-TGM, Vienna

FISCHER Christopher

Laboratory of Polymer Engineering LKT-TGM and University of Vienna, Faculty of Physics, Group of Physics of Nanostructured Materials

WILHELM Harald

Graz University of Technology, Institute of Inorganic Chemistry

AMENITSCH Heinz
CACHO-NERIN Fernando
KRIECHBAUM Manfred
MARMIROLI Benedetta
RAPPOLT Michael
SARTORI Barbara

Johannes Kepler University, Institute of Semiconductor and Solid State Physics, Linz

HEISS W.

Medical University of Graz, Institute of Biophysics

KORNMUELLER Karin
PRASSL Ruth
VONACH Caroline

Montanuniversity Leoben, Department of Physics

LECHNER Rainer T.
PARIS Oskar
PREHAL Christian
SHARIFI RAJABI Parvin

NanoTecCenter Weiz Forschungsgesellschaft mbH, Weiz

LIST-KRATOCHVIL E. J. W.
NAU S.
SAX S.

University of Graz, Biophysics Division, Institute of Molecular Science

KOLLMITZER Benjamin
HEFTBERGER Peter
PABST Georg

University of Vienna, Faculty of Physics, Group Physics of Nanostructured Materials

POLT Gerald
SCHAFLER Erhard
SPIECKERMANN Florian
ZEHETBAUER Michael J.

Belgium

Université de Namur, Department of Physics, Namur

BUSBY Yan
PIREAUX J.-J.

Croatia

Institute of Physics, Zagreb

SALAMON Krešimir

"Ruđer Bošković" Institute, Zagreb

BOGDANOVIĆ-RADOVIĆ Ivancica
BULJAN Maya
DUBČEK Pavo
GAJOVIĆ Andreja
GRACIN, Davor
JANICKI V.
JAKSIC, Milko
JURAIĆ Krunoslav
KARLUŠIĆ Marko
PIVAC Branko
RADIĆ Nikola

University of Split, Faculty of Chemistry and Technology, Dept. of Organic Technology, Split

BANOVAC Irena

University of Split, Faculty of Chemistry and Technology, Department of Inorganic Technology, Split

JOZIĆ Dražan

Czech Republic

Academy of Sciences of the Czech Republic, Institute of Macromolecular Chemistry, Prague

DE LOS SANTOS PEREIRA Andres
JAGER Alessandro
JAGER Eliezer
RODRIGUEZ-EMMENEGGER Cesar
SKODOVA Michaela
SURMAN Frantisek

ŠTĚPÁNEK Petr

Charles University, Faculty of Mathematics and Physics, Prague

ENDRES Jan
HOLY Václav
VALEŠ Václav

University of Pardubice, Institute of Applied Physics and Mathematics, FCHT; and Academy of Sciences of the Czech Republic, Institute of Macromolecular Chemistry, Prague

STEINHART Milos
STEINHARTOVA Tereza

Denmark

University of Copenhagen, Department of Pharmacy, Faculty of Health and Medical Sciences, Copenhagen

LARSEN C.
ØSTERGAARD J.
WENG LARSEN S.
YAGHMUR Anan

France

Institut Galien-UMR CNRS 8612, Châtenay-Malabry

FAIVRE Vincent
LESIEUR S.

Institut Galien-UMR CNRS 8612, Châtenay-Malabry, and SANOFI, Ambarès

SEQUIER Floriane

SANOFI, Ambarès

DASTE G.
RENOUARD M.

Université de Paris-sud, Faculté de Pharmacie, UMR CNRS, Chatênay-Malabry

BOURGAUX Claudie
LEPELTIER Elise

Germany

Eberhard Karls Universität Tübingen, Institute of Applied Physic

BANERJEE Rupak
NOVÁK Jiri
SCHREIBER F.
SORARUF Daniel

Iran

Hakim Sabzevari University, Department of Materials and Polymer Engineering, Sabzevar

OVEISI Hamidreza

Italy

C.N.R. - Istituto di Biofisica (I.B.F.), Unita' di Genova

GALENO Lauretta
MORAN Oscar

CNR (National Research Council), Institute of Biophysics, Palermo

BULONE Donatella
MARTORANA Vincenzo
SAN BIAGI P.
VILASI Silvia

Elettra - Sincrotrone Trieste S.C.p.A., Trieste

BERNSTORFF Sigrid
CASALIS Loredana
DE MARCH Matteo
KRASTANOVA Ivet
MORELLO Christian
ONESTI Silvia Caterina Elvira
PARISSE Pietro

IMM-CNR, Istituto per la Microelettronica e i Microsistemi, Bologna

FERLAUTO Laura
LISCIO Fabiola
MILITA Silvia

ISMN-CNR, Istituto per lo Studio del Materiali Nanostrutturati, Bologna

CAVALLINI M.
GENTILI D.

SISSA (International School for Advanced Studies), Trieste

IANESELLI Luca

Università Bicocca - Scienze dei Materiali, Milan

D'ARIENZO Massimiliano

University of Cagliari, Department of Electrical and Electronic Engineering, Cagliari

BONFIGLIO A.
CASULA G.
COSSEDDU Piero

University of Messina, Department of Inorganic, Analytical and Physical Chemistry

CAMPAGNA S.
LA GANGA G.

PUNTORIERO F.

Università di Milano, Dipartimento di Fisica & CIMaINa, Milano
DEVETTA Michele
PISERI Paolo

University of Padova - Department of Chemical Sciences, Padova
BONCHIO M.
CARRARO Mauro
SARTOREL A.

Università di Palermo, Department BIONEC, Palermo
CAPELLO F.

Università Politecnica delle Marche, Depart. Science of Life and Environment, Ancona
MARIANI Paolo
ORTORE Maria Grazia
SPINOZZI Francesco

Università di Sassari, Laboratorio di Scienza dei Materiali e Nanotecnologie (LMNT-D.A.D.U.), and CR-INSTM, Alghero
INNOCENZI Plinio
MALFATTI Luca
MARONGIU Daniela
PINNA Alessandra

University of Trieste, Department of Chemical and Pharmaceutical Sciences, Trieste
BONASERA Aurelio
MARANGONI Tomas
PRATO Maurizio
SYRGIANNIS Zois

University of Trieste, Dep. of Engineering and Architecture, Trieste
TACCANI Rodolfo
VALLE Francesco

Japan

Osaka Prefecture University, Graduate School of Engineering, Sakai
TOKUDOME Yasuaki

Morocco

Faculté des Sciences et Techniques, Physics Department, Tanger
CHAHBOUN Adil

Netherlands

Zernike Institute for Advanced Materials, University of Groningen

AKHTAR Naureen
AQEEL Aisha
PALSTRA T.T.M.
POLYAKOV A.O.
RUDOLF Petra

Portugal

University of Minho, Department of Chemistry, Braga

BIERNACKI Krzysztof
FONSECA António Mauricio Costa
KUZNIARSKA-BIERNACKA Iwona

University of Minho, Department of Physics, Braga

GOMES Maria J.M.
KHODOROV Anatoli
LEVICHEV Sergey
ROLO Anabela G.
SEKHAR Koppole Chandra
VIEIRA Eliana M. F.

Singapure

Institute of Materials Research and Engineering, Agency for Science, Technology and Research

SONAR P.

Slovenia

Institute of Mathematics, Physics and Mechanics, Ljubljana; and University of Maribor, Faculty of Natural Sciences and Mathematics

JAGODIČ Marko

Jožef Stefan Institute, Department for Nanostructured Materials, Ljubljana

ČEH Miran

Jožef Stefan Institute, Condensed Matter Physics Department, Ljubljana

CORDOYIANNIS Georgios
JESENEK Dalija
LAVRIČ Marta

Jožef Stefan Institute, Materials Synthesis Department, Ljubljana

GYERGYEK Saso

Jozef Stefan International Postgraduate School, Ljubljana

PUC Uros

Jožef Stefan Institute, Condensed Matter Physics Department, Ljubljana, and Jožef Stefan International Postgraduate School Ljubljana, and University of Maribor, Faculty of Natural Sciences and Mathematics, Maribor

ZIDANŠEK Alexander

University of Ljubljana, Biotechnical Faculty

BOLJTE Sabina
DRASLER Barbara
DROBNE D.
KONONENKO Veno
OTRIN Lado
SIMON Martin

Spain

Laser Processing Group, Optics Institute, CSIC, Madrid

MARTÍN-SÁNCHEZ Javier

Universidad Complutense de Madrid

ROLDAN M.A.

Universidad de Cádiz, Departamento de Ciencia de los Materiales e Ing. Metalúrgica y Q. I., Cádiz

MOLINA S.I.

Switzerland

Ecole Polytechnique Fédérale de Lausanne, Faculté des Sciences de Base, Lausanne

MOGLIANETTI Mauro

EMPA-Swiss Federal Laboratories for Materials Science and Technology, Dübendorf

YAREMA M.

Turkey

Middle East Technical University, Department of Metallurgical and Materials Engineering, Çankaya

GENC Ayse
KALAY Yunus Eren
YAGMURLU Bengi
YILDIRIM Can

United Kingdom

Imperial College London, London

CARRONI M.
PATWARDHAN A.

University College London, Department of Chemistry, Christopher Ingold Labs
BATTAGLIA Giuseppe

University of Cambridge, Cavendish Laboratory
KULKARNI Chandrashekhar V.

University of Sheffield, Department of Biomedical Science
CECCHIN Denis
PEARSON Russell
VISWANATHAN Priyalakshmi

USA

Oak Ridge National Laboratory, Materials Science and Technology Division,Oak Ridge, Tennessee
VARELA M.
PENNYCOOK S.J.

The University of Texas, Microelectronics Research Centre, Austin
DODABALAPUR A.

List of Performed Experiments

2012 (first half year)

Proposal	Proposer	Institute	Country	Title	Research Field
20115014	MORAN Oscar	C.N.R. - Istituto di Biofisica (I.B.F.)	Italy	Structural modifications of the CFTR regulatory domain by phosphorylation and potentiators	Life Sciences
20115058	KORNMUELLER Karin	Austrian Academy of Sciences (AAS), Inst. of Biophysics and Nanosystems Research (IBN), Graz	Austria	Studies on the membrane-activity of surfactant-like designer-peptides	Life Sciences
20115063	FONSECA Antonio Mauricio	Univ. of Minho, Chemistry Depart.	Portugal	SAXS characterization of drug encapsulate on zeolites	Materials Science
20115123	KALAY Yunus Eren	Middle East Techn. Univ., Depart. of Metallurgical and Materials Engineering	Turkey	Local structural orders in Al based metallic glasses	Materials Science
20115233	BULJAN Maja	Ruder Bošković Insitute, Zagreb	Croatia	Self-assembled Ge quantum dots on Si substrates: a regular ordering achieved by magnetron sputtering	Materials Science
20115244	HOLY Vaclav	Charles University, Prague	Czech Republic	Structure of TiO_2/Fe_2O_3 nano-crystals in silica matrix	Materials Science
20115246	MILITA Silvia	C.N.R., Inst. IMM, sez. Bologna	Italy	Real time investigation of crystallization and aggregation dynamics in ambipolar semiconductive polymer during thermal annealing	Materials Science
20115315	JOZIC Drazan	Faculty of Chemical Technology, Dept. of Physics, Split	Croatia	In-situ characterization of the developing microstructure in geopolymers under different experimental preparation conditions by simultaneous SAXS/WAXS	Chemistry
20115320	PARISSE Pietro	Sincrotrone Trieste	Italy	Enzymatic reaction on DNA modified gold nanoparticles	Life Sciences
20115334	BOURGAUX Claudie	C.N.R.S., Univ. of Paris Sud	France	Nanostructured self-assemlies of squalene-based nucleolipids	Life Sciences
20115341	GOMES Maria	Departamento de Fisica Universidade do Minho	Portugal	GID and GISAXS investigations of flash memory structures based on semiconductor nanocrystals	Materials Science
20115363	MARMIROLI Benedetta	AAS- IBN, Graz	Austria	Sub 10 millisecond time-resolved SAXS studies of calcium carbonate formation in presence of additives	Chemistry
20115375	MALFATTI Luca	University of Sassari	Italy	In-situ time-resolved study of self-assembled silica films with hierarchical porosity	Chemistry
20115397	PISERI Paolo	Dep. of Physics, Univ. of Milan	Italy	SAXS from free metal clusters in a molecular beam	Materials Science
20115409	JAGER Alessandro	Academy of Sciences, Inst. of Macromolecular Chemistry, Prague	Czech Republic	Kinetic effects on the properties of particles formed by nanoprecipitation	Materials Science
20115417	AMENITSCH Heinz	AAS, IBN, Graz	Austria	In situ titration experiment to resolve the influence of inhibition polymers on the early stages of CaCO3 growth in situ with SWAXS	Materials Science

20115434	MARMIROLI Benedetta	AAS- IBN, Graz	Austria	Degradation in high temperature PEM fuell cells	Materials Science
20115436	GRACIN Davor	Ruder Bošković Insitute, Zagreb	Croatia	Nano-structures in thin film solar cells materials	Materials Science
20115440	AMENITSCH Heinz	AAS, IBN, Graz	Austria	In situ study of the assembly of water-rich mesoporous materials and mesoporous nanoparticles in the areosol phase	Materials Science
20115446	AMENITSCH Heinz	AAS, IBN, Graz	Austria	Interaction of striped gold nanoparticles with model membrane systems	Life Sciences
inhouse research	AMENITSCH Heinz & TORMEN Massimo	AAS, IBN, Graz & CNR, Istituto Officina dei Materiali	Austria & Italy	Effects of co-solvents on the morphology of spin-coated P3HT:PCBM bulk heterojunction by GISAXS/GIWAXD for application to polymer solar cells	Materials Science
inhouse research	AMENITSCH Heinz & D'ARIENZO Massimiliano	AAS- IBN, Graz & Univ. Bicocca, Materials Science	Austria & Italy	Growth Mechanism of Shape Controlled TiO2 Nanocrystals: the role of capping agents in determining the morphology evolution	Materials Science
inhouse research	BERNSTORFF Sigrid & GOMES Maria	Sincrotrone Trieste & Departamento de Fisica Universidade do Minho	Italy & Portugal	GID and GISAXS investigation of Co- doped ZnO nanocrystals in silica and alumina matrices	Materials Science
inhouse research	AMENITSCH Heinz & ONESTI Silvia	AAS- IBN, Graz & Sincrotrone Trieste S.C.p.A.	Austria & Italy	Structural analysis of human proteins involved in DNA replication	Life Sciences
inhouse research	BERNSTORFF Sigrid & DUBCEK Pavo	Sincrotrone Trieste & Ruder Bošković Insitute, Zagreb	Italy & Croatia	Structural investigation of Si and Ge inclusion into refractory metal thin films	Materials Science
inhouse research	AMENITSCH Heinz & SYRGIANNIS Zois	AAS- IBN, Graz & Univ. of Trieste, Dep. of Pharmaceutical Science	Austria & Italy	Stability measurements for perylene-tetracarbocylic acid bisimides (PDIs) nano-aggregates suitable for electronics	Chemistry

2012 (second half year)

Proposal	Proposer	Institute	Country	Title	Research Field
20120034	PABST Georg	Inst. of Molecular Sciences, Biophysics Div., Univ. of Graz	Austria	Kinetics of Domain Formation in Lipid Bilayers	Life Sciences
20120073	HOLY Vaclav	Charles Univ., Prague	Czech Republic	Structure of core-shell semiconductor nanocrystals: GISAXS study	Materials Science
20120150	ZIDANSEK Aleksander	Jožef Stefan Institute, Ljubljana	Slovenia	SAXS in soft nanocomposites, magnetoelectrics and elastomers	Materials Science
20120160	FAIVRE Vincent	Institute Galien, UMR CNRS 8612, Châtenay-Malabry	France	Impact of polyoxylglyceride-based excipients on API release from lipid particles: focus on API crystallinity and polyoxylglyceride hydration	Life Sciences
20120161	RODRIGUEZ-EMMENEGGER Cesar	Academy of Sciences, Inst. of Macromolecular Chemistry, Prague	Czech Republic	Influence of supramolecular arrangement of polymer brushes on their resistance to blood plasma fouling	Materials Science
20120184	MARMIROLI Benedetta	Inst. of Inorganic Chemistry (IIC), Univ. of Technology (TU), Graz	Austria	Degradation in high temperature PEM fuell cells	Materials Science
20120217	BULJAN Maja	Rudjer Boskovic Institute, Zagreb	Croatia	Determination of ion track radii in amorphous matrices	Materials Science

20120219	SPIECKERMANN Florian	Nanostructured Materials group, Univ. of Vienna	Austria	The impact of the amorphous phase on the deformation induced formation of dislocations in iPP	Materials Science
20120224	RAPPOLT Michael	IIC, TU Graz	Austria	Effects of carbon based nanoparticles on model lipid membranes	Life Sciences
20120232	RAPPOLT Michael	IIC, TU Graz	Austria	Effect of Hydrodynamic Pressure on Nanostructured Lipid Particles	Life Sciences
20120239	ORTORE Maria Grazia	Depart. of Life and Environmental Sciences, Marche Polytechnic Univ. and CNISM, Ancona	Italy	The controversial role of Hsp60: an extensive in solution SAXS study	Life Sciences
20120244	NOVAK Jiri	Inst. of Applied Physics, Eberhard Karls Univ., Tübingen	Germany	Hybrid films of metal nano-particles embedded in organic semiconductor matrices for non-volatile memories	Materials Science
20120349	GOMES Maria	Physics Depart., Univ. of Minho	Portugal	Structural and electrical characterization of nanostructures based on SiGe nanocrystals embedded in Al2O3 matrix	Materials Science
20120378	AKHTAR Naureen	Zernike Institute for Advanced Materials, Univ. of Groningen	Netherlands	Ultra-thin organic-inorganic hybrid films based on conducting magnets	Materials Science
20120389	LECHNER Rainer T.	Inst. of Physics, Montanuniv. Leoben	Austria	In-situ investigation of the self-assembled growth of nanocrystal solids with SAXS	Materials Science
20120390	D'ARIENZO Massimiliano	Univ. Bicocca, Materials Science, Milan	Italy	Growth mechanism of shape controlled TiO_2 nanocrystals: the crucial role of capping agents in determining the morphology evolution	Materials Science
20120422	GRACIN Davor	Rudjer Boskovic Institute, Zagreb	Croatia	Influence of thermal annealing on nano-structures in thin film solar cells materials	Materials Science
20120437	MARMIROLI Benedetta	IIC, TU Graz	Austria	GISAXS study of the confined growth of calcium carbonate in nano-channels made of mesoporous silica	Chemistry
20120469	WANG Linge	Univ of Sheffield, Depart. of Biomedical Science	UK	Biocompatible Polymersome Nanostructure: Phase diagram and self-assembly mechanism of the PMPC-PDPA block copolymer polymersome	Life Sciences
Inhouse	AMENITSCH Heinz & ONESTI Silvia	IIC, TU Graz & Elettra-Sincrotrone Trieste	Austria & Italy	Structural analysis of human proteins involved in DNA replication	Life Sciences
Inhouse	BERNSTORFF Sigrid & DUBCEK Pavo	Elettra-Sincrotrone Trieste & Rudjer Boskovic Institute, Zagreb	Italy & Croatia	Silver nano particles for future photovolataic applications	Materials Science
Inhouse	AMENITSCH Heinz	IIC, TU Graz	Austria	Characterization of supramolecular aggregations based on polyaromatic-core molecule.	Materials Science
Inhouse	BERNSTORFF Sigrid & SCHAFLER Erhard	Elettra- Sincrotrone Trieste & Nanostructured Materials Group, Univ. of Vienna	Italy & Austria	In-situ thermal treatment of ultrafine-grained metals produced by severe plastic deformation II	Materials Science
Inhouse	SAXS-group & OVEISI Hamidreza	Depart. of Materials & Polymer Engineering, Hakim Sabzevari Univ., Sabzevar	Austria & Italy & Iran	Cryogenic system-assisted self assembly process in highly ordered mesostructured thin films	Chemistry

User Statistics

1. Number of submitted proposals and assigned shifts from 1995 until December 2013

The Austrian SAXS-beamline at ELETTRA opened to users in September 1996. Since then many experiments have been performed related to the fields of life science, materials science, physics, biophysics, chemistry, medical science, technology and instrumentation.

The assignment of beamtime at this beamline is done separately for the group of "General Users" (GU) and the "Collaborating Research Group" (CRG), i.e., the Austrian users. Beamtime was assigned to the proposals of each group in the order of the rating received by the Scientific Committee, and up to the maximum number of shifts available to each group according to the contract between "The Austrian Academy of Sciences" and the "Sincrotrone Trieste". Until December 1997 up to 30 % of the beamtime was given to CRG, up to 55 % to GU, and 15% was reserved for maintenance purposes. From January 98 to June 2001 the quota for beamtime was up to 35 % for CRG, up to 50 % for GU, and again 15% reserved for maintenance purposes. From July 2001 on the two contingents for user proposals from CRG and GU receive up to 35% of the beamtime each. The remaining 30 % of beamtime are used for inhouse research projects as well as for maintenance purposes.

Figure 1 gives an overview of the numbers of received proposals, the numbers of requested and assigned shifts, as well as the percentage between assigned and requested shifts during the last years. As can be seen in Fig.1, the request for beamtime at the SAXS-beamline increased strongly until the first half year of 1999. Then, probably due to the high rejection rates, the number of submitted proposals decreased somewhat during 2001, which resulted in a better ratio of accepted / rejected proposals. This oscillating behaviour of beamtime request can also be seen for the period 2002 – 2013 where after higher numbers of submitted proposals slightly reduced request periods follow. The numbers for the second semester of 2007 and first of 2008 reflect also that, due to the long shut-down from 1.10.2007 to 3.03.2008 (for the new booster-electron-injector installation) less proposals were submitted, and less beamtime was available.

In 2012, in total 75 proposals (12 from CRG, and 63 from GU) were submitted. From these 3 CRG and 6 GU proposals were submitted by "new" usergroups, i.e. groups which so far had never beamtime at the SAXS beamline. From these, 3 GU and all 3 CRG proposals were accepted by the review committee.

Figure 1 (Next page). The statistical information about the beamtime periods since end of 1995 are given for the groups "CRG", and "GU" separately, as well as for both together ("Total"). Shown are, for all beamtime periods (from top to bottom):

● Number of received proposals, ● Number of requested shifts,
● Number of assigned shifts, and ● Relation between assigned and requested shifts

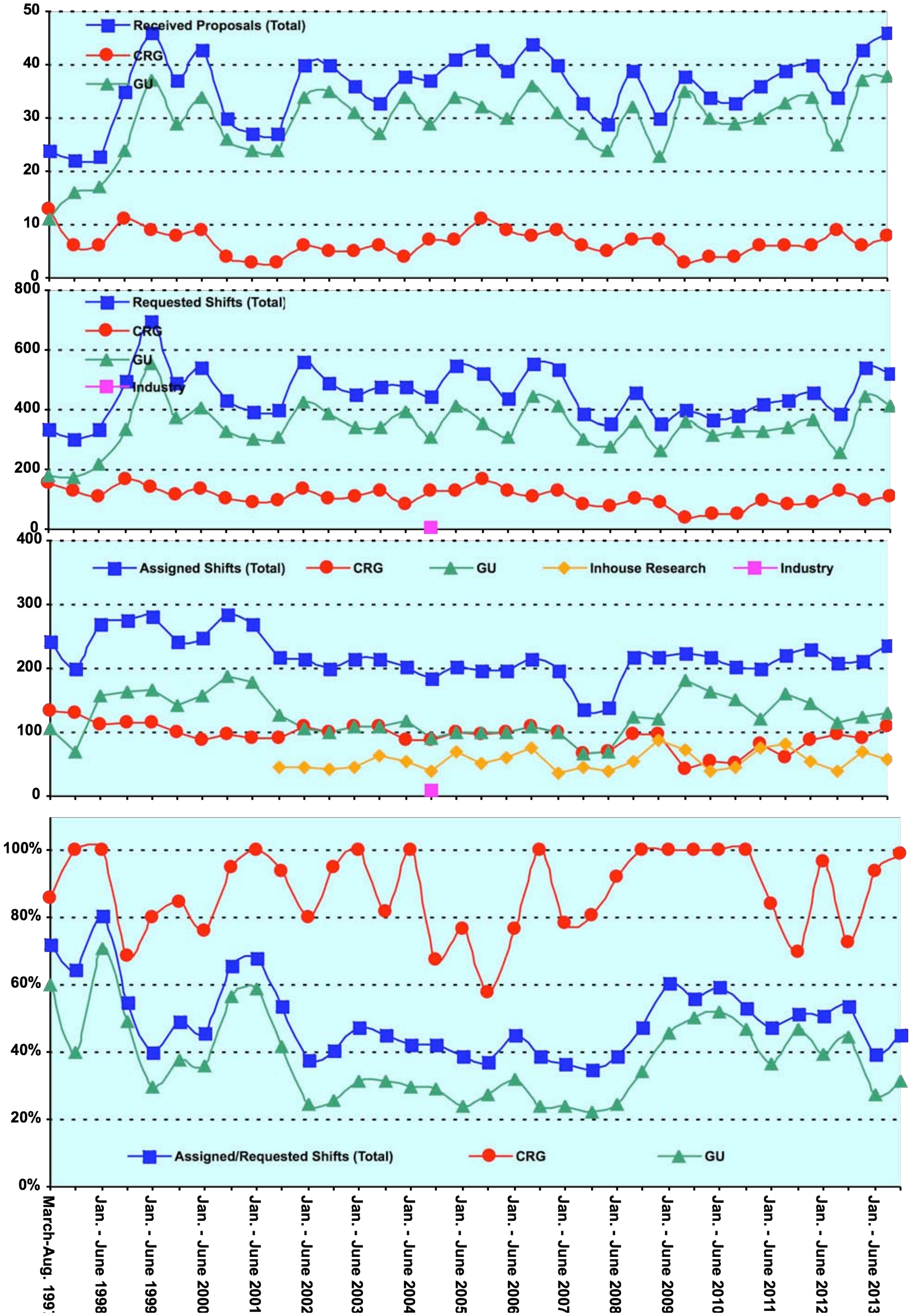
Received Proposals (Total)
CRG
GU
50
40
30
20
10
0
Requested Shifts (Total)
CRG
GU
Industry
800
600
400
200
0
Assigned Shifts (Total)
CRG
GU
Inhouse Research
Industry
400
300
200
100
0
100%
80%
60%
40%
20%
0%
Assigned/Requested Shifts (Total)
CRG
GU
March-Aug. 199
Jan. - June 1998
Jan. - June 1999
Jan. - June 2000
Jan. - June 2001
Jan. - June 2002
Jan. - June 2003
Jan. - June 2004
Jan. - June 2005
Jan. - June 2006
Jan. - June 2007
Jan. - June 2008
Jan. - June 2009
Jan. - June 2010
Jan. - June 2011
Jan. - June 2012
Jan. - June 2013

2. Provenience of users

During 2012, 167 users from 66 institutes in 21 countries have performed experiments at the SAXS beamline. In Fig. 2 are shown both the provenience of these users, and of their respective institutes. Each user or institute was counted only once, even though many users performed experiments in both beamtime periods of 2012.

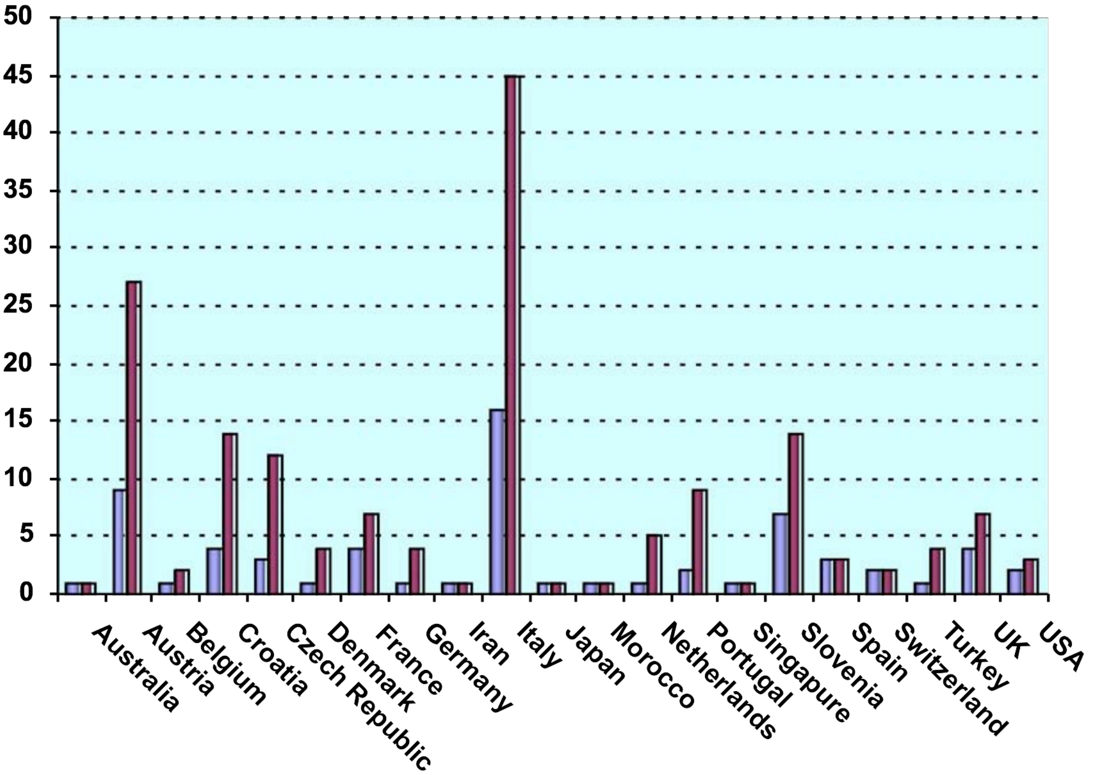

Figure 2. Nationality of the Austrian SAXS beamline users in the year 2012. The number of users (red) and the corresponding number of institutes (blue) are shown for each country.

3. Documentation of experimental results

As could be expected, with the start of user-operation at the SAXS-beamline the number of contributions to conferences started to increase strongly. With a delay of one year - the average time needed for paper publications - also the number of publications increased accordingly, as can be seen in Fig. 3.

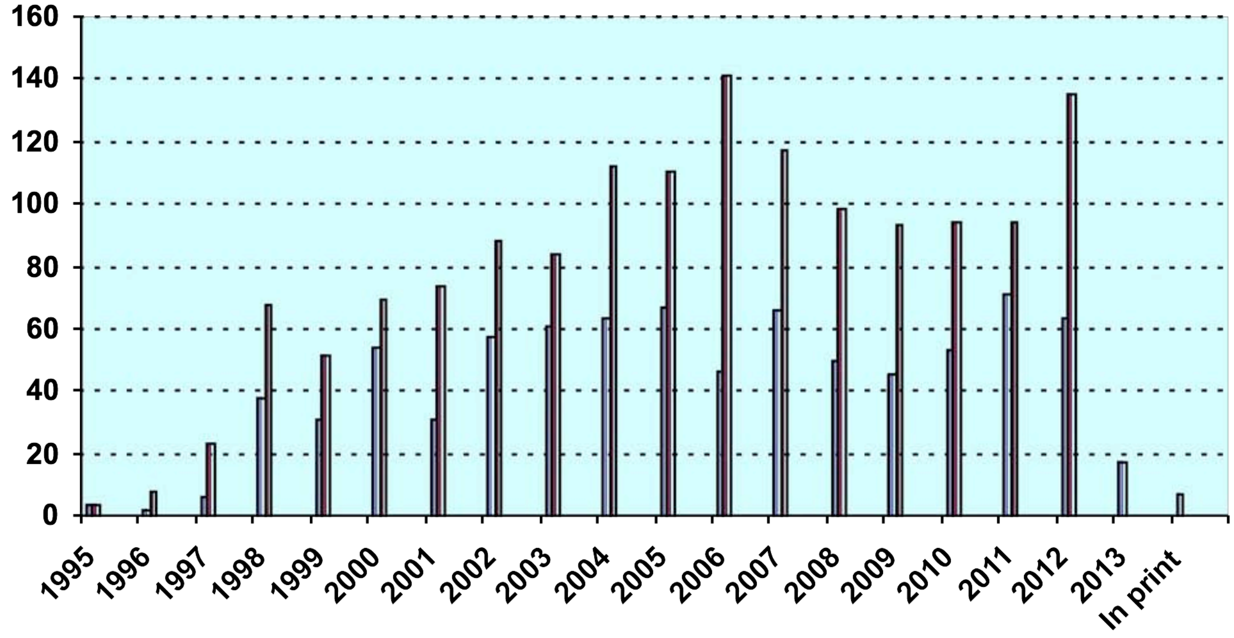

Figure 3. Number of conference contributions (blue) and of refereed paper publications (red) for the years 1995-2012. Also contributions, which have been published until August 2013 as well as those in print at that time are included.

In addition, from 1995 until August 2013, the following documentations based on instrumentation of the SAXS-beamline, or on data taken with it, have been produced:

Technical Reports on Instrumentation: 5
Contributions to Elettra Newsletters: 15
Contributions to Elettra Highlights: 44
Habil Thesis: 4
PhD Thesis: 96
Master Thesis: 42

Experimental Possibilities at the SAXS-beamline

1. NEW DEVELOPMENTS AND INSTRUMENTATION

Domed hot stage

A domed hot stage (model DHS1100 from Anton Paar, Graz, Austria) for in-situ temperature studies was recently bought. It operates in a temperature range from 25 to 1100°C, and gas connections allow sample measurements in vacuum or inert gas to avoid oxidation or other chemical reactions of the sample at high temperatures.

The special, dome-shaped X-ray window is made of graphite, which exhibits an excellent combination of good mechanical properties, high temperature resistance and X-ray transmission. Moreover a custom made cover with Kapton windows has been constructed which allows GISAXS measurements at lower temperatures with reduced window background. This cell allows e.g. for variable humidity environment or inert gas flow. Below 200 °C heater temperature, the instrument can be run without dome.

The hot stage is light weight, and can be mounted onto our goniometer craddle for GISAXS measurements on thin films or surfaces, as well as on the XY stage for transmission measurements. A transmission cell for 1.5 mm diameter capillaries has been constructed.

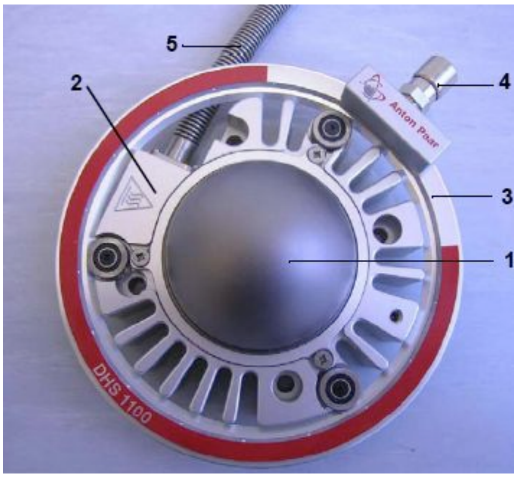

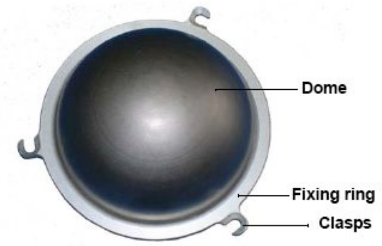

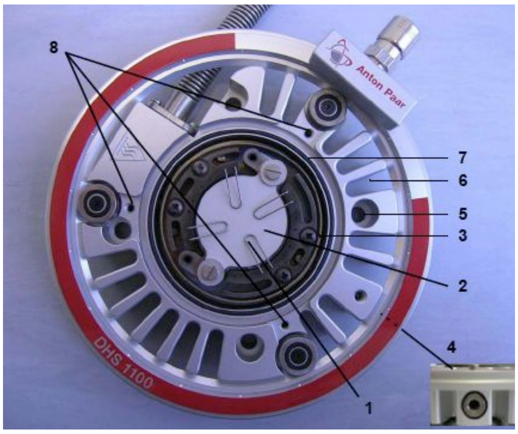

Figure 1: the hot stage and its components:

top left: 1: dome, 2: housing, 3: turnable cooling ring with outlets for cooling air, 4. quick coupling connection for cooling air supply, 5: supply hose for gas/vacuum and temperature control

bottom left: 1: springs for fixing the sample, 2: sample plate, 3: temperature shieldings, 4: pressure relief valve, 5: bore holes for mounting the DHS 1100, 6: cooling fins, 7: O-ring for the dome, 8: fixing screws for the dome

top right: dome

Due to the design of dome, heater and sample fixing, very low angles of incidence can be reached and the following types of X-ray measurements can be carried out:

-grazing incidence small angle scattering
-pole figures
-grazing incidence diffraction
-grazing incidence in-plane diffraction

The main applications for the DHS 1100 are to investigate the temperature dependence of

-crystalline textures
-crystal stress and strain
-temperature-induced phase transitions
-structural properties of thin films

Spectrometers

Two spectrometers are now available in the X-ray lab:

UV-VIS spectrometer

Besides a standard 10 mm path length cuvette holder, the UV-VIS spectrophotometer (Cary 60, Agilent Technologies) (Fig. 2) is equipped with a Slide-Mounted External Specular Reflectance accessory which allows specular reflectance measurements to be made at a fixed angle of 30°. This accessory is suitable for studies of the film thickness on metallic substrates and measurements of epitaxial film thickness. Interchangeable masks for examining small samples or small areas of large samples are provided (3 mm, 6 mm and 13 mm diameters).
The instrument can also be used for *in situ* measurement on liquid samples, through two optic fibers: a Torlon fiber probe, diameter 10 mm, for aggressive solutions, and a µprobe, 3.5 mm diameter, 10 mm fixed path length, for smaller volumes (approx. 500 µl) (Fig. 3).

Figure 2

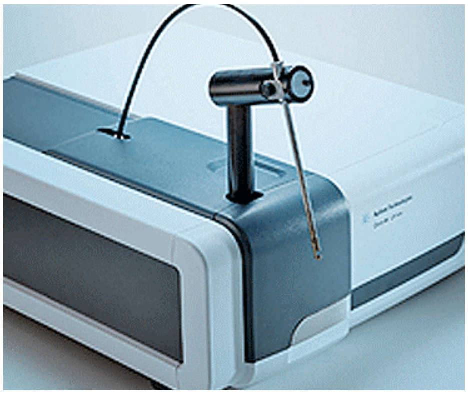

Figure 3

Specifications:

- double beam Czerny-Turner monochromator
- wavelength range 190–1100 nm
- fixed spectral bandwidth 1.5 nm
- minimum scan rates of 24,000 nm/min (full wavelenght scan time <3s)
- maximum measurement rate 80 data points/sec

FT-IR spectrometer

FT-IR spectroscopy is a widespread and powerful tool for the identification and characterization of a diverse range of materials. Molecular structures and components are identified via their typical infrared absorption bands. FT-IR spectroscopy can be applied for the qualitative characterization of materials, as well as for their quantification. In recent years, FT-IR spectroscopy has increasingly been employed to analyze the surfaces of materials and objects.
The FT-IR specrometer (Alpha-T, Bruker Optics) is equipped with two modules for the analysis of different types of samples:

1. standard sample holder for transmission measurements,

2. single reflection diamond ATR sampling module for powder and solid analysis (Fig 4), which, due to the wide free working area around the crystal (approx. 350°), allows the analysis of large samples.
   Specifications:
   - One reflection Diamond crystal
   - Spectral range: 375 - 7,500 cm^{-1}
   - Ergonomic one-finger clamp mechanism
   - Working distance (max. sample height): >20 mm

3. sampling module for contactless reflection measurements in front of the spectrometer.
   Specifications:
   - Spectral range: 375-7,500cm^{-1}
   - Measurement spot: 6mm diameter, appr. 15 mm in front of the spectrometer

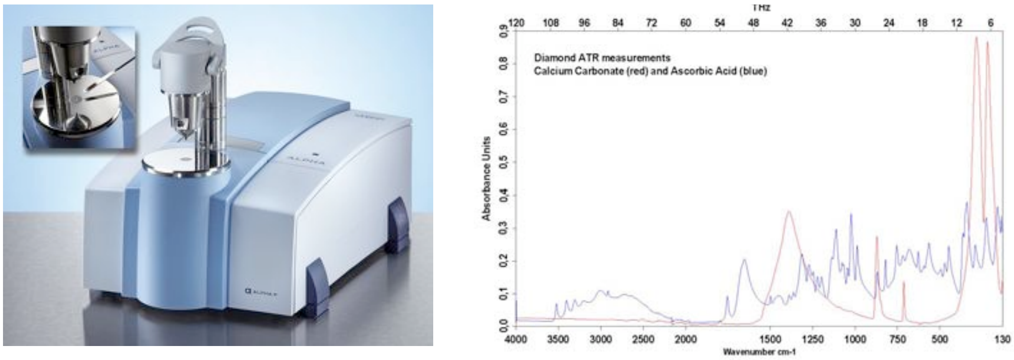

Figure 4

New Pilatus3 1M detector system ordered

A PILATUS3 1M Detector System has been ordered from Dectris Ltd. (Baden, Switzerland), and will most probably be available for users by the end of 2013. It has similar features as our currently available Pilatus 100K Detector System (see page 36), but will have a much larger area (168.7 x 179.4 mm^2 instead of only 83.8 x 33.5 mm^2). The main Pilatus3 1M detector features will be:

Number of detector modules	2 x 5
Total sensitive area [mm^2]	168.7 x 179.4
Pixel size [μm^2]	172 x 172
Number of pixels	981 x 1043 = 1 023 183
Point-spread function [FWHM]	1 pixel
Dead area/gap between modules	7.2%
Dynamic range [Bits]	20
Counting rate per pixel	10^7 photons/sec (incoming X-rays)
Readout time [ms]	0.95
Maximum frame rate [Hz]	500

2. ACCESSIBLE SAXS AND WAXS RANGES

The accessable **SAXS-range** depends on the requirements of each specific experiment: the required SAXS resolution (minimum q-value needed) defines the minimum possible sample-to-detector distance, which in turn limits the maximum reachable q-value due to the limited detector and vacuum-tube sizes. Also the required time-resolution can limit the effectively accessable SAXS-range, depending of the active size of the most suitable detector from our pool (see pages 27-28, 37-38). Therefore, first-time users should contact their local contact in usefull time before coming to ELETTRA in order to design their experiment accordingly.
Generally, the sample-to-detector distance can vary between a minimum of ca. 20 cm, and a maximum of 3 m. Thus, depending on the photon energy, maximum SAXS resolutions of 2000 Å (5.4 keV), 1400 Å (8 keV) or 630 Å (16 keV) are available.

Simultaneous SAXS- and WAXS-measurements can be performed using two different detectors at the same time. The accessable **WAXS-range** depends also on the requirements for each specific experiment, namely on the size of the required WAXS-detector, and the vacuum chambers needed for the SAXS-range. Maximum angles (2θ) of about 80° are possible.

A specially designed vacuum chamber (SWAXS-nose, see Annual Report of 1996/97, p. 32) allows to use both scattering areas below (for SAXS) and above (for WAXS) the direct beam, respectively. The overall length of the SWAXS-nose in the horizontal direction, measured from the sample position, is 512 mm and the fixed sample to WAXS-detector distance is 324 mm. With a SAXS camera-length of $\leq$ 1.25 m an overlap in the d-spacings covered by the SAXS- and WAXS-detectors, respectively, is possible: then, the common regime lies around 9 Å d-spacing.

3. CALIBRATION OF THE S-AXIS AND FLAT FIELD CORRECTION

At the SAXS beamline various standards are used for the angular (s-scale) calibration of the different detectors:

- Rat tail tendon for the SAXS detector - high resolution (rtt*.dat)
- Silver behenate for the SAXS detector – medium and low resolution (agbeh*.dat)
- Para-bromo benzoic acid for the WAXS detector – WAXS range 1 and 2 (pbromo*.dat)
- Combination of Cu, Al foils and Si powder for the WAXS detector – WAXS range 2 and higher

In Figure 1 a typical diffraction pattern of rat tail tendon is shown, depicting the diffraction orders (from the first to the 14th order) measured with a "high" resolution set-up (2.3 m) and the delay-line gas detector. The d-spacing is assumed to be 650 Å, but this value can vary depending on humidity up to 3%. Thus, the rat tail tendon is often used only to determine the position of the direct beam (zero order), while the absolute calibration is performed using the diffraction pattern of Silver behenate powder. Fig. 2 depicts a diffraction pattern of Silver behenate measured with "medium" resolution set-up (1.0 m) from the first to the 4th order (repeat spacing 58.4 Å) [1].

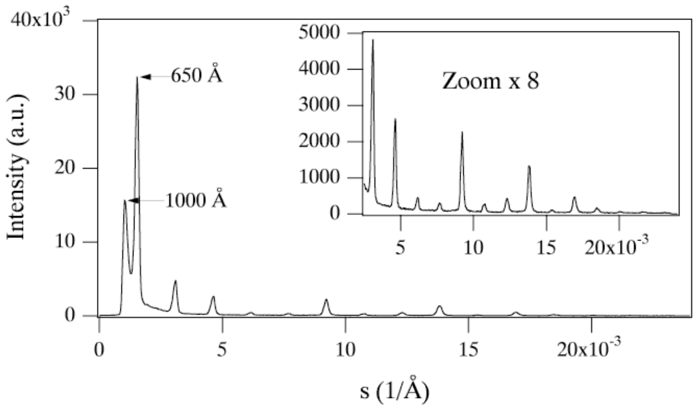

Figure 1. SAXS diffraction pattern of the collagen structure of rat tail tendon fibre at a distance of 2.3 m

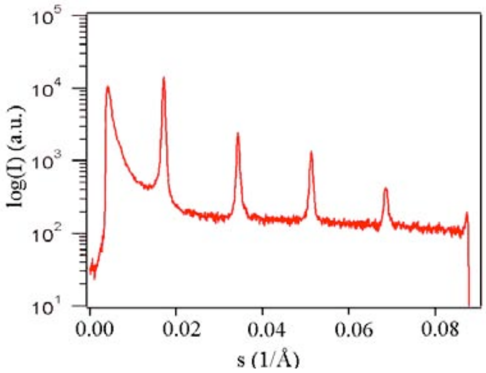

Figure 2. SAXS diffraction pattern of Ag behenate powder at a distance of 1.0 m

In Figure 3 a typical WAXS pattern of p-bromo benzoic acid is shown. The diffraction peaks are indexed according to the values given in Table 2, taken from [2].

d-spacing/Å	rel. intensity	d-spacing/Å	rel. intensity
14.72	18000	4.25	490
7.36	1200	3.96	2380
6.02	330	3.84	10300
5.67	980	3.74	26530
5.21	6550	3.68	1740
4.72	26000	3.47	760

Table 2. d-spacings and relative intensities of p-bromo benzoic acid according to [2].

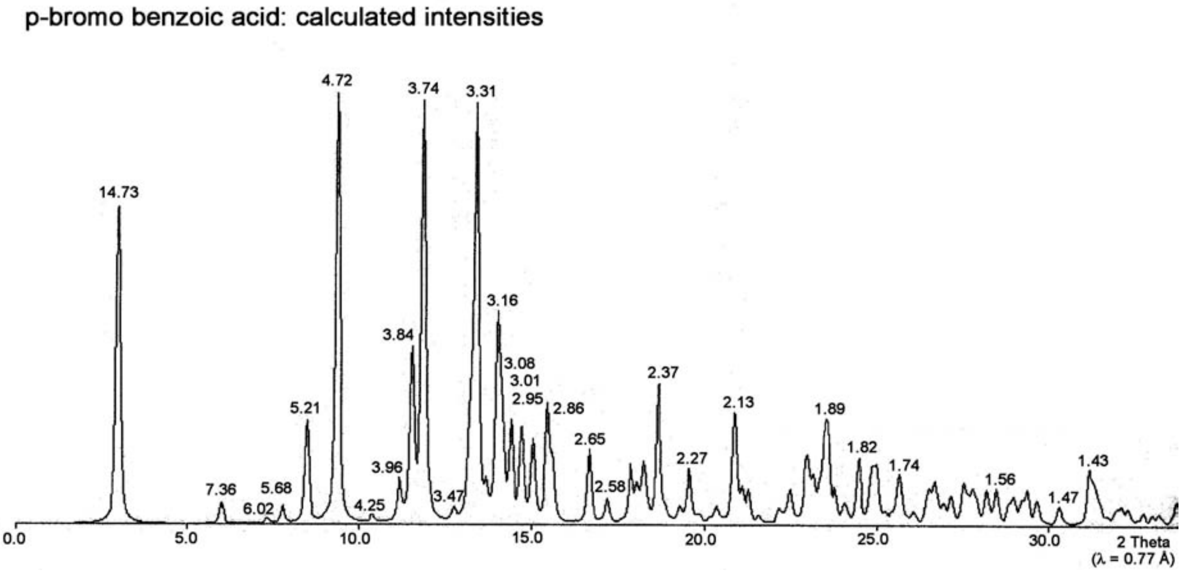

Figure 3. Calculated diffraction pattern of p-bromo benzoic acid. d-spacings are given in Å.

The s-scale for both, the SAXS and the WAXS range, can be obtained by linear regression, i.e., the linear relation between the known s-values of the calibrant versus the measured peak positions has to be found.

A further correction is regarding the flat field response (efficiency) of the detectors. For this correction, the fluorescence light of various foils are used to illuminate the detectors rather homogeneously:

At 8 keV: iron foil (100 μm thick), fluorescence energy: 6.4 keV K_α, 7.1 keV K_β (effic*.dat)
At 16 keV: copper foil (> 100 μm thick), fluorescence energy: 8.028 keV $K_{\alpha2}$, 8.048 keV $K_{\alpha1}$, 8.905 keV K_β (effic*.dat)

The measured scattering pattern are corrected for the detector efficiency simply by dividing them by the fluorescence pattern. Note: The average of the detector efficiency data should be set to unity and a small threshold should be applied to avoid any division by zero.

[1] T.N. Blanton et. al., Powder Diffraction 10, (1995), 91
[2] K. Ohura, S. Kashino, M. Haisa, J. Bull. Chem. Soc. Jpn. 45, (1972), 2651

4. AVAILABLE SAMPLE MANIPULATIONS STAGES

1. General

Usually the sample is mounted onto the sample alignment stage which allows the user to place the sample into the beam with a precision of 5µm (resolution: 1µm). In Fig. 5 the ranges for vertical and horizontal alignment as well as the maximum dimensions of the sample holders are given. The maximum weight on the sample stage is limited to 10 kg. In case the envelope dimensions of a sophisticated sample station provided by the users are slightly larger than those given in Fig. 5, the user can ask the beamline responsible for a check up of his space requirements. If it does not fit at all to these specifications, user equipment can also be mounted directly onto the optical table, which allows much larger spatial dimensions.

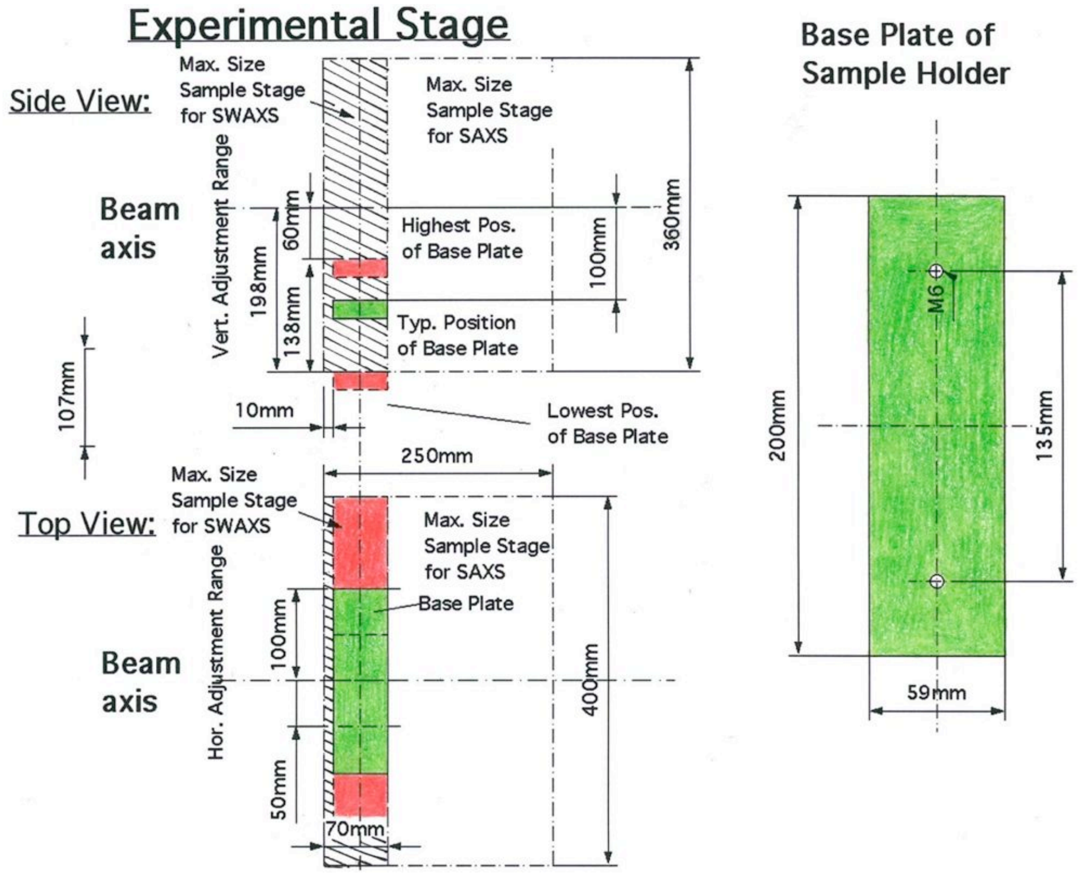

Figure 5. Maximum dimensions and alignment range of the sample holder to be mounted via a base-plate onto the standard alignment stage (left), and dimensions of the base-plate (right).

2. Sample Holders

As standard equipment for liquid samples Paar capillaries (diameter: 1 and 2 mm) are used thermostated with the KPR (Peltier heating/cooling) sample holders (Anton Paar, Graz, Austria). For use in these sample holders flow through capillaries and Gel holders are standard equipment. Temperature scans can be performed with KPR (-30-70 °C). Typically the precision and the stability of this systems is 0.1 °C. Additionally thermostats for temperature control or cooling proposes can be used at the beamline (-40 - 200 °C). Helium and Nitrogen gas bottles are available at the beamline, for other gases please contact the beamline responsible.

Multiple-sample holders can be mounted onto the standard sample manipulator. At present holders are available for measuring in automatic mode up to 30 solid samples at ambient temperature or up to 4 liquid or gel samples in the temperature range 0 – 95 °C.

3. Online Exhaust System

At the experimental station is available a custom-built fume cover and chemical exhaust system for toxic gases. Thus it is possible to e.g. study in-situ chemical reactions, during which toxic gases might develop.

4. Stopped Flow Apparatus

A commercial stopped flow apparatus (manufactured by Bio-Logic, Paris, France), especially designed for Synchrotron Radiation SAXS investigations of conformation changes of proteins, nucleic acids and macromolecules, is available. The instrument consists of a 4-syringe cell with 3 mixer modules manufactured by Bio-Logic. Each syringe is driven independently from the others by an individual stepping-motor, which allows a high versatility of the mixing sequence (flow-rate, flow duration, sequential mixing). For example, injection sequences using one or up to 4 syringes, unequal filling of syringes, variable mixing ratio, reaction intermediate ageing in three- or four-syringe mode etc.. The solution flow can be entirely software-controlled via stepping motors, and can stop in a fraction of a millisecond.

The software allows the set-up of the shot volumes of each of the 4 syringes in a certain time interval. Up to 20 mixing protocols can be programmed. Additionally macros for the repeated execution of individual frames can be defined. Furthermore, the input and output trigger accessible for user operation can be programmed. In the usual operation modus the start of rapid mixing sequence is triggered from our X-ray data-acquisition system (input trigger).

After the liquids have been rapidly mixed, they are filled within few ms into a 1 mm quartz capillary - situated in the X-ray beam- , which is thermostated with a water bath. Depending on the diffraction power of the sample time resolutions of up to 10 ms can be obtained.

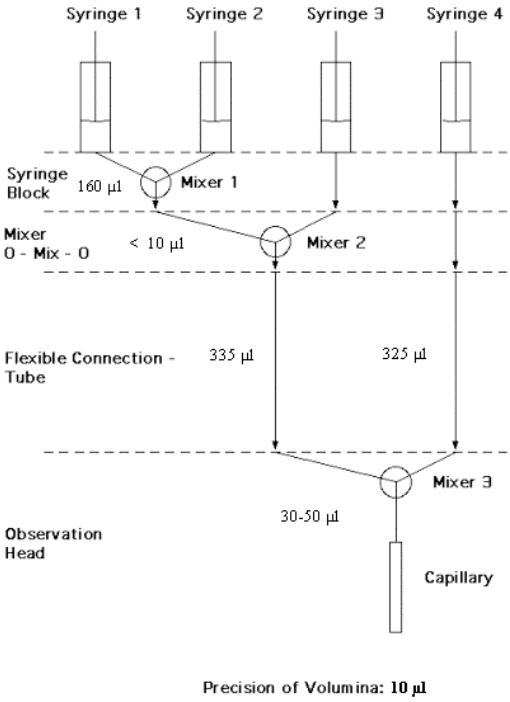

Figure 6. Sketch of the stop flow system.

The main parameter of the system are:

- Thermostated quartz capillary (1 mm)
- Temperature stability 0.1 °C
- Total sample used per mixing cycle (shot volume): 100 µl
- Maximum 2θ angle of 45°
- Total Volume 8 ml
- Dead volume 550 µl
- Flow rate: 0.045 – 6 ml/s
- Duration of flow 1 ms to 9999 ms/Phase
- Dead time: 1 ms
- Reservoir volume: 10 ml each

Further information can be found at the webpage: http://www.bio-logic.fr/

5. Grazing Incidence Small Angle X-ray Scattering

Grazing incidence studies on solid samples, thin film samples or Langmuir-Blodget-films can be performed using a specially designed sample holder, which can be rotated around 2 axes transversal to the beam. Furthermore the sample can be aligned by translating it in both directions transversal to the beam. The precisions are 0.001 deg for the rotations and 5 µm for the translations. Usually the system is set to reflect the beam in the vertical direction. According to the required protocol and the actual assembly of the rotation stages ω, θ, 2θ and φ scans can be performed.

6. Temperature Gradient Cell

A temperature gradient cell for X-ray scattering investigations on the thermal behaviour of soft matter manybody-systems, such as in gels, dispersions and solutions, has been developed. Depending on the adjustment of the temperature gradient in the sample, on the focus size of the X-ray beam and on the translational scanning precision an averaged thermal resolution of a few thousands of a degree can be achieved.

7. Flow-through Cell

The flow through cell works in a simple manner: Special quartz capillaries (Glas Technik & Konstruktion, Schönwalde/Berlin) of 1.5 mm diameter and wide openings of about 3 mm at each end, can be inserted into the standard Anton Paar sample holder, which allows various temperature treatments (T-range 25-300 or –30-70 °C, respectively). Thin tubes are connected directly to the capillary ends and a constanst flow is achieved by a peristaltic pump.

8. IR-Laser T-Jump System for Time-Resolved X-ray Scattering on Aqueous Solutions and Dispersions

The Erbium-Glass Laser available at the SAXS-beamline (Dr. Rapp Optoelektronik, Hamburg, Germany) delivers a maximum of 4 J per 2ms pulse with a wavelength of 1.54 µm onto the sample. The laser-beam is guided by one prism onto the sample, which is filled in a glass capillary (1 or 2 mm in diameter) and Peltier or electronically thermostated in a metal sample holder (A. Paar, Graz, Austria). With a laser spotsize of maximal 7 mm in diameter a sample-volume of maximal 5.5 µl or 22 µl, respectively, is exposed to the laser-radiation. In a water-solutions/dispersions with an absorption coefficient of A = 6.5 cm^{-1} T-jumps up to 20°C are possible.

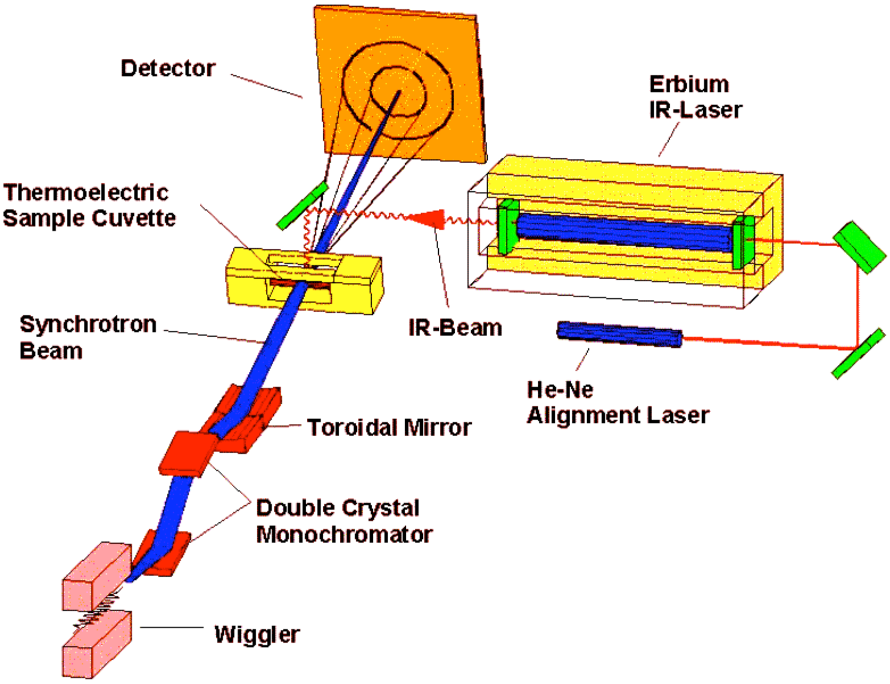

Figure 7. Sketch of the T-jump set-up.

9. High Pressure Cell System

SWAXS measurements of samples under pressure can be performed from 1 to 2500 bar, from 0 to 80 °C in the scattering angle region up to 30 degrees, both in the static or time-resolved mode, e.g. p-jump or p-scan, with a time-resolution down to the ms range. Precise pressure scans of any speed within a broad range (e.g. ca. 1.0 bar/s - 50 bar/s in the case of water as pressurising medium, and a typical sample volume) can be performed. Alternatively, dynamic processes can be studied in pressure-jump relaxation experiments with jump amplitudes up to 2.5 kbar/10ms in both directions (pressurising and depressurising jumps).

In most applications diamond windows of 0.75 mm thickness (each) are used. The transmission of one pair (entrance and exit window) is 0.1 at 8 keV, i.e. lower than 0.3, the value for the originally used 1.5 mm thick Be-windows. However the loss in intensity is more than compensated for by the considerably lower background scattering of diamond thus leading to higher q-resolution in the experiments.

The sample thickness can be 0.6-4.0 mm, with a volume of approximately 0.5-3 mm^3 completely irradiated by pin-hole collimated (< 1.0 mm diameter) X-rays.

The pressure cell system is flexible and can be built according to the needs of the particular experiment. Normally, a liquid (water, ethanol or octanol) is used as pressurising medium. But in principle, also gaseous media can be employed as well. N_2 has been successfully tested, and measurements in supercritical CO_2 became frequent.
Beside bulk measurements on samples in transmission set-up, also grazing incidence experiments using silicon wafer with highly aligned samples on its surface inserted in the high-pressure cell have been carried out successfully.

10. Oxford Cryostream Cooler

The Cryostream cooler creates a cold environment only a few millimeters from the nozzle position. The temperature and the flow of the nitrogen gas stream is controlled and regulated by a Programmable Temperature Controller based on an 'in stream' heater and a thermo-sensor before it passes out over the sample.

The system has been especially developed for X-ray crystallography to perform diffraction experiments on e.g. shock frozen bio-crystals. However, the programmable temperature controller allows further implication for SAXS-experiments, e.g., rapid temperature drops in solvents. The design of the Cryostream Cooler facilitates:

- Nitrogen stream temperatures from -190 to 100 °C
- Stability of 0.1 °C,
- Refill without any disturbance of the temperature at the sample
- Temperature ramps can easily be carried out remotely controlled with scan rates up 6 °C/min
- Individual temperature protocols can be cycled
- T-jumps in both directions can be performed by rapid transfer of the sample in a pre-cooled or -heated capillary using an fast syringe driver reaching a minimum temperature of -80 °C. Here, typical scan rates are about 15 °C/sec with a total process time in the order of 10 sec.

Further information can be found at the webpage: http://www.oxfordcryosystems.co.uk/

11. In-line Differential Scanning Calorimeter (DSC)

The in-line micro-calorimeter built by the group of Michel Ollivon (CNRS, Paris, France) allows to take simultaneously time-resolved synchrotron X-ray Diffraction as a function of the Temperature (XRDT) and high sensitivity DSC from the same same sample.
The microcalorimetry and XRDT scans can be performed at any heating rate comprised between 0.1 and 10 °C/min with a 0.01 °C temperature resolution in the range -30/+130 °C. However, maximum cooling rates are T dependent and 10°C/min rates cannot be sustained below 30°C since cooling efficiency is a temperature dependent process. Microcalorimetry scans can be recorded independently, and also simultaniously, of X-ray patterns. The microcalorimeter head can also be used as a temperature controlled sample-holder for X-ray measurements while not recording a microcalorimetry signal. Isothermal microcalorimetry is also possible when a time dependent thermal event such as meta-stable state relaxation or self-evolving reaction, is expected. The sample capillaries have a diameter of 1.5 mm and are filled over a length of 10 mm.

12. Tension Cell

Together with the external user group Schulze-Bauer/Holzapfel the research team constructed a general-purpose tension cell. This particular cell was designed for *in-situ* tensile testing with the particular feature that the sample could be completely immersed in a solvent (e.g. physiological solution), which is of particular interest for the blood vessel or collagen fiber testing. The sample container can be attached to a thermal bath to control the temperature in the range from 5 to 95 ºC. A screw with an appropriate opening for the passage of the X-ray beam can adjust the optical thickness of the sample container continuously and optimize the set-up for different sample geometries.

The fully remote controlled system allows to control not only the fiber extension from 0 to 50 mm, but also it records simultaneously the force signal in the range from 0 to 25 N and as an option the optically determined Video extensometer signal to measure the transversal contraction of the sample.

13. Larger experimental hutch

After the prolungation of the experimental hutch by about 3m we have now the possibility to e.g. permanently install a diffractometer (roll on/roll off), or a micro focus set-up, which delivers focal spot sizes down to 10 µm and thus will allow for micro spot scanning SWAXS experiments with a new X-Y scanning stage.

On the other hand we can increase the sample to detector distance and therefore improve our minimum SAXS resolution or maximise the flux density at the sample position for certain experiments. Nevertheless this prolongation of the experimental hutch will ensure the sustainable development of the beamline also in the future by giving us the opportunity to realize new optical concepts, e.g. new mirrors, Fresnel or refractive lenses.

5. AVAILABLE DETECTORS

1. 2D Image Plate

The Mar300 Image Plate detector with a circular active area of 300mm in diameter is the largest-area detector available to users of the beamline, with a spatial resolution (pixel size) of 150μm. This detector has two modes of operation (180mm or 300mm), depending on the desired active area, which result in image sizes of 1200x1200 and 2000x2000, respectively. They are stored in the mar image format (16 bit for compactness, with higher precision extensions for values out of range), and can be processed and converted using the Fit2D program [1]. Typical applications are those that need a large Q-range with high dynamic range (typical values of 10^5), i.e. solution scattering from proteins and nanoparticles, temperature-step scans, slow processes like nanoparticle formation, mesophase formation, etc. The exposure time for the Image Plate is given in seconds, with typical values between 1 and 60. Readout time depends on the chosen active area (for 180mm mode, about 130 seconds; for 300mm mode, about 210 seconds), and therefore it is not suitable for samples where high time resolution is needed. Exposure information, number of images in the series and other information is automatically written to a summary file after each image.
So far the detector cannot be triggered by an external trigger input. Controlling an additional (external) device or experiment can only be done by hardware wiring of the TTL shutter signal.

2. 2D Pilatus 100K Detector System

The Pilatus 100K detector system (http://www.dectris.com/sites/pilatus100k.html) operates in "single photon counting" mode and is based on the CMOS hybrid pixel technology: the X-rays are directly transformed into electric charge, and processed in the CMOS readout chips. This new design has no dark current or readout noise, a high dynamic range of 1000000 (20 bits), a read-out time of less than 3 ms, a framing rate of over 200 images/s and an excellent point spread function of < 1 pixel.

3. 2D CCD-Camera System

The CCD (Phtotonic Science, GemStar/XIDIS model) is a high resolution and sensitivity camera, providing a high dynamic range (16 bit) and advanced features such as on-camera binning and external triggering. The camera is fully software-controlled using the Image Pro Plus software, and connects to the controlling computer via a Hi-Speed USB interface.

Camera specifications:

Sensitive area	82 x 74 mm (110 mm diagonal)
Image size	2048 x 2048
Pixel size	43 μm
Dynamic range	16 bit (20 bit in exposure fusion mode)
Binning	x1, x2, x4, x8 (independent X and Y, on-chip and in software)
Interface	external triggering, external gating (3.3V TTL)
Intensifier gain	12 bit (0-4095 levels, approx 200:1 max gain)
Exposure time	<1ms to 30 min

Frame rate	at x1 binning, ~800 ms readout time per frame at x8 binning (on-chip), ~145 ms readout time per frame
Image format	16bit TIFF native (Image Pro Plus allows exporting to other formats as well)

4. 1D Vantec Detector

Two identical one-dimensional high-count rate capable Vantec-1 Detectors from BrukerAXS Inc. are available. They have each an active area of 50 x 16 mm, and can be used together mounted in-line to increase the active area. They have a spatial resolution of about 50 µm, which is smaller than the resolution obtained by the presently used Gabriel Type Gas detectors. Moreover its new gas amplification principle based on the Microgap technology [1] allows much higher count rates compared to the old system. Now the main limitation is the data acquisition system with its maximum integral count rate of about 1 MHz. In the present data acquisition system HCI (Hecus X-ray Systems, Graz, Austria) the detector has the following performance:

- Minimal time resolution: 11 µs
- Maximum No. of frames: 512 (depending on the no. of channels)
- Maximum integral count rate: 1 MHz

5. 1D Gabriel-type Detector System

Two 1D Gabriel-type detectors are available, which feature both 1024 pixels. The smaller detector has an entrance window size of 8 x 100 mm, and an active length of 86.1 mm with a resolution of 0.135 mm/channel. The larger detector has an entrance window size of 10 x 150 mm, and an active length of 134 mm with a resolution of 0.159 mm/channel. They can be used simultaneously, and are run with the data acquisition system HCI (Hecus X-ray Systems, Graz, Austria). This detector system has the following performance:

- Minimal time resolution: 11 microsec
- Maximum No. of frames: 512
- Maximum integral count rate: 40 kHz

6. OFFLINE SAXS SUPPORT LABORATORY

The laboratory consists of two rooms: the chemistry lab, which has been renewed during 2013, serves mainly for sample preparation and analysis for both, in house research and external SAXS user groups. In the X-ray laboratory is available a SWAXS camera for simultaneous small and wide-angle scattering (Hecus X-ray Systems, Graz, Austria: www.hecus.at), which allows on-site testing of samples before moving on to the SR beamline.

The chemistry lab is also equipped with:

- micro centrifuge (max. 13200 rpm; model 5415D from Eppendorf, Hamburg, Germany)
- Chemical fume hood, equipped with a carbon filter for general organic solvents (model GS8000 from Strola, Italy)
- vacuum drying oven (min. pressure 1 mbar; max. T: 200 °C, precision +/- 0.4 °C; Binder WTB, Tuttlingen. Germany)
- balance (min.-max.: 0.001 - 220 g; model 770 from Kern & Sohn, Balingen, Germany)
- Magnetic stirrer with heating plate and thermometer, temp max 260 °C
- vortex for microtubes (model REAX from Heidolph, Schwabach, Germany)
- two water baths :
  - Unistat CC, freely programmable in the range from -30 to 100°C (Huber, Offenburg, Germany);
  - Lauda M3, available for heating only (Lauda-Könighofen, Germany)
- ultrasonic bath with water heater (VWR International, Milano, Italy)
- Ultrasonic processor equipped with a 3 mm probe (Sonics VCX130, SY-LAB Geräte GmbH, Germany)
- HPLC pump, Pharmacia LKB; working range, 0,01-9,99 ml/min, 0,1-40MPa
- HPLC pump, Gilson 307; working range, 0,01- 5 ml/min, 0,1-60MPa
- three-syringe pump, low pressure; flow rate range, 1µl/hr – 2120 ml/hr (TSE Systems GmbH, Germany)
- four-syringe pump, high pressure: P max ~ 60 bar (Harvard Apparatus, Holliston, Massachusetts, USA)
- three high pressure infusion modules: P max ~ 690 bar (Teledyne Isco, Lincoln, NE, USA)
- fridge (+ 4°C) and freezer (- 20 °C)

Standard glassware, syringes and needles of different sizes, µ-pipettes (p10 - p100 - p200 - p1000), as well as some standard chemical reagents (e.g., chloroform, ethanol, methanol) and deionized water (milli-RO and ultrapure milli-Q water) is available.

Figure 4. View of the Chemistry laboratory (left) and X-Ray laboratory (right).

User Contributions

Material Science

ULTRA-THIN ORGANIC-INORGANIC HYBRID FILMS BASED ON CONDUCTING MAGNETS

N. Akhtar[1], A.O. Polyakov[1], A. Aqeel[1], H. Amenitsch[2], P. Rudolf[1] and T. T. M. Palstra[1]

1.) Zernike Institute for Advanced Materials, University of Groningen, Nijenborgh 4, 9747AG Groningen, The Netherlands
2.) Institute of Inorganic Chemistry, Graz University of Technology, Stremayrgasse 9/IV, 8010 Graz, Austria

We investigated the crystalline properties of the organic-inorganic hybrid films deposited by the Langmuir-Blodgett (LB) technique. As sketched in Figure 1 these films consist of layers of organic molecules separated by inorganic sheets. At the SAXS beamline, we determined the length of repeat unit in the out-of-plane geometry and investigated the homogeneity of the films by recording diffraction data in various points on the film. Moreover, to extract information on the stacking of the individual layers within the film, rocking curves were recorded. The hybrid films were studied both in dry and humid conditions to determine the stability of the structure.

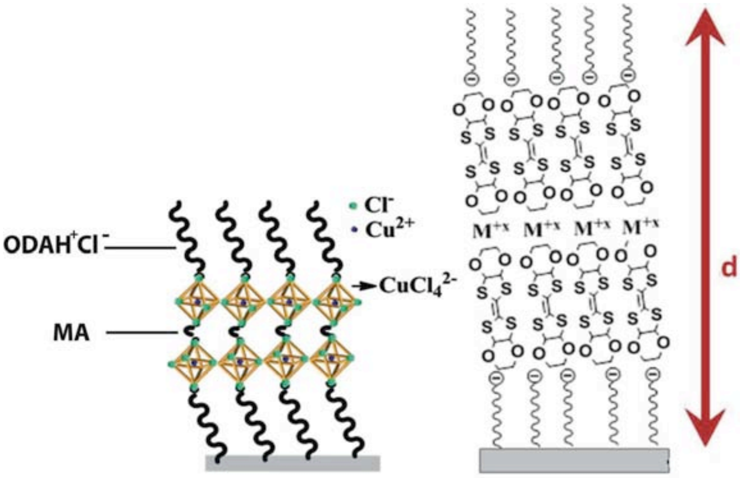

Figure 1. Left: Sketch of repeat unit in CuCl4-based hybrid LB film with octadecyl ammonium chloride (ODAH+Cl-) and methyl amine (MA) as organic ligands.
Right: Sketch of repeat unit in arachidic acid (C20)+BEDO-TTF+M+x hybrid LB film with M+x = Gd+3, Cu+2.

$CuCl_4$-based hybrid LB films:

Figure 2 displays the out-of-plane diffraction data taken at 7 different spots on a 16-layer-thick and an 8-layer-thick film, both with an area of 1×2 cm^2. All the spots showed a similar diffraction pattern pointing to homogenous films. The length of smallest periodic unit perpendicular to the film surface (d) was calculated from the position of the diffraction peaks using the Bragg formula. The value for d found for both 8-layer-thick and the 16-layer-thick CuCl4-based hybrid LB film was 54.5±0.4 Å, which demonstrates that the crystal structure is independent of the number of layers. Calculations, based on the X-ray diffraction studies of the bulk $CuCl_4(CH_3CH_2NH_3)_2$ hybrid have determined a Cu-Cl out-of-plane distance of 2.3038 Å, while the N-N out-of-plane distance in the $CuCl_4(MA)_2$ single crystal hybrid has been found to be 2 Å. Taking into account these values and the length of ODAH+ molecule, the d value for our model should be about 62 Å. The smaller value of the experimental d calculated from the diffraction peak positions can be explained as due to tilting of the long ODA ligands.

Figure 3 displays the rocking curve (θ-scan) measured at the (001) peak position in the out-of-plane orientation. A Gaussian fit of the rocking curve indicates that the individual layers are stacked almost parallel to each other with an average tilting angle of 0.039±0.001o as visualized in the sketch in figure 3. The in-plane XRD pattern of the 16-layer-thick $CuCl_4$-based hybrid LB film presented figure 4 showed one diffraction peak which confirms that the film is crystalline also in the plane. A large FWHM of the peak indicates presence of more than one diffraction lines.

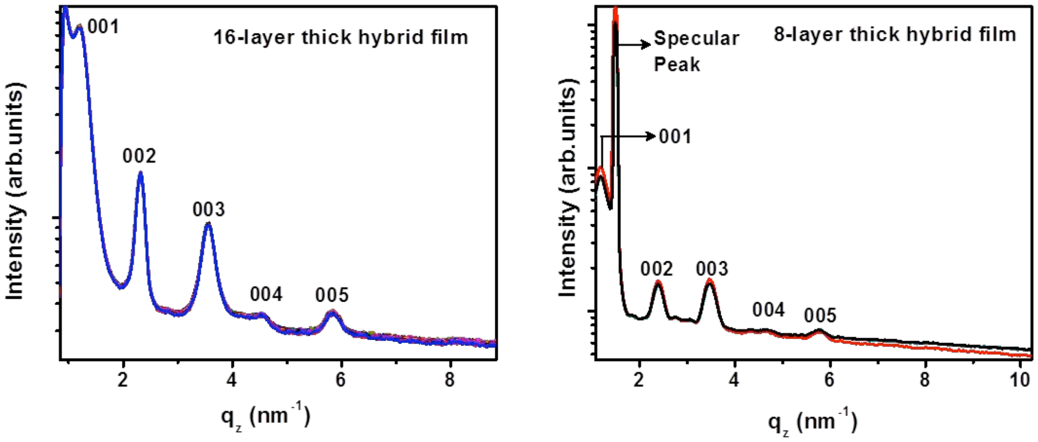

Figure 2. Out-of-plane diffraction profile of 16-layer thick (left) and 8-layer thick (right) $CuCl_4$-based hybrid LB film taken at various spots.

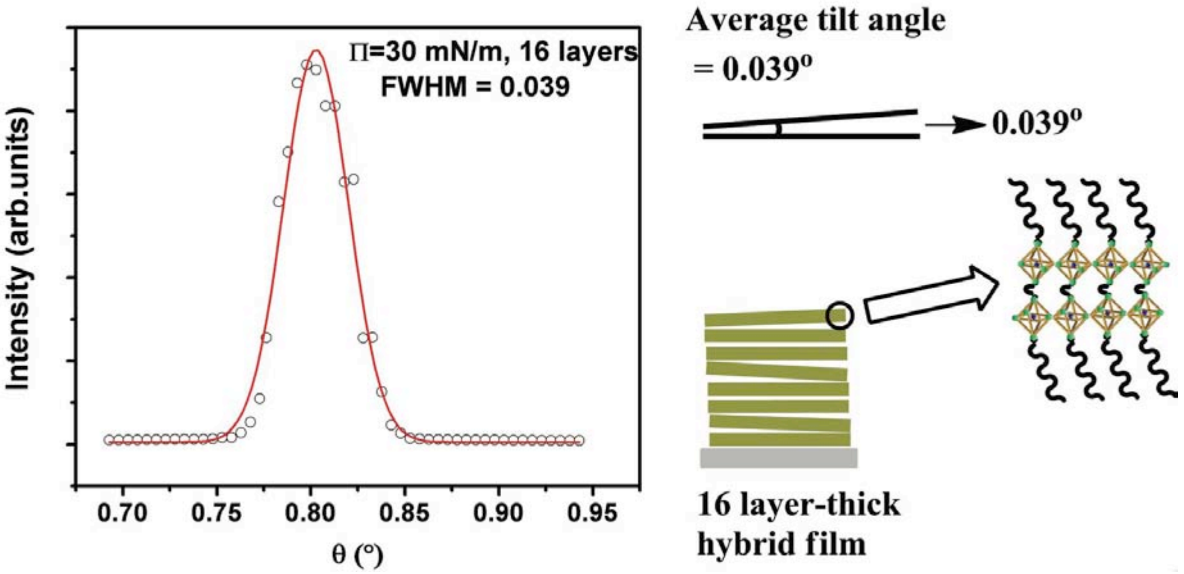

Figure 3. Left panel: Rocking curve measured at the (001) diffraction peak position of a 16-layer-thick CuCl4-based hybrid LB film deposited at a surface pressure of 30 mN/m. The red solid line represents the Gaussian fit to the data. Right panel: Sketch of the layer stacking in the film growth direction.

Hybrid LB films based on conducting magnets:

The out-of-plane X-ray diffraction curves recorded at 7 different spots of 22-layer-thick C_{20} + BEDO-TTF + Gd LB film deposited onto an area of 1×2 cm2 is shown in figure 5. All the spots showed a similar diffraction pattern indicating a homogenous film. Seven diffraction peaks were observed and indexed as 001, 002, 003, 004, 005, 006 and 007. Using the Bragg's diffraction condition, the dimension of the periodic unit in the growth direction was found to be d = 55±1 Å which is smaller than the theoretically calculated value of 75 Å. This indicates that the organic molecules are tilted away from the direction normal towards the film plane. This is different from the geometry of a C_{20} + BEDO-TTF + Cu LB film, where the d value as calculated from diffraction data obtained from laboratory diffractometer was 75±1 Å.

Further information on the stacking of individual layers in these multilayer hybrid LB films was obtained from rocking curves (θ-scans) measured at the 001 peak position in the out-of-plane direction. Appearance of a single peak demonstrated that the individual layers are tidily stacked in both these hybrid films. The average tilt angle between the layers, as calculated from the FWHM of the rocking curves in figure 6, was 0.094±0.001° for the C_{20} + BEDO-TTF + Cu LB film and 0.038±0.0008° for the C_{20} + BEDO-TTF + Gd LB film. The smaller value for the Gd containing film indicates even better packing of the individual layers compared to the film with Cu complexes.

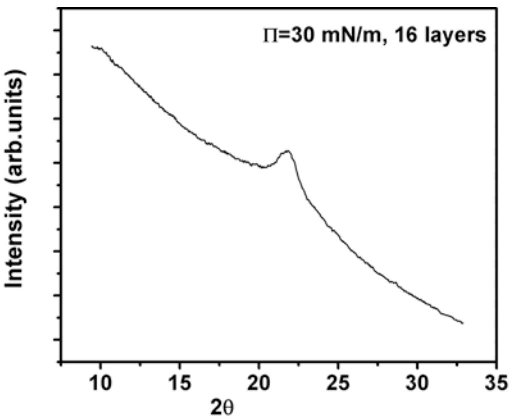

Figure 4. In-plane diffraction pattern of a 16-layer thick $CuCl_4$-based hybrid LB film deposited at a surface pressure (Π) of 30 mN/m.

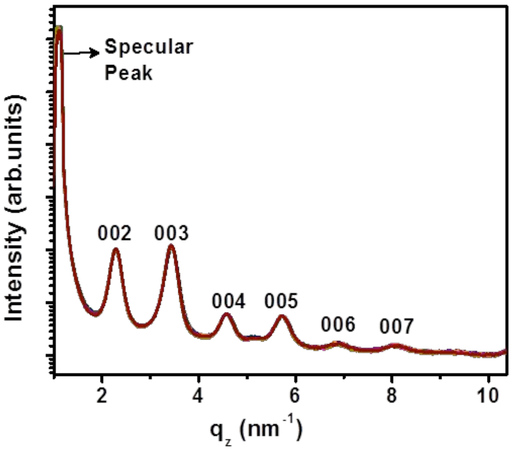

Figure 5. Out-of-plane diffraction profile of 22-layer thick C_{20}+BEDO-TTF+Gd hybrid LB film taken at various spots.

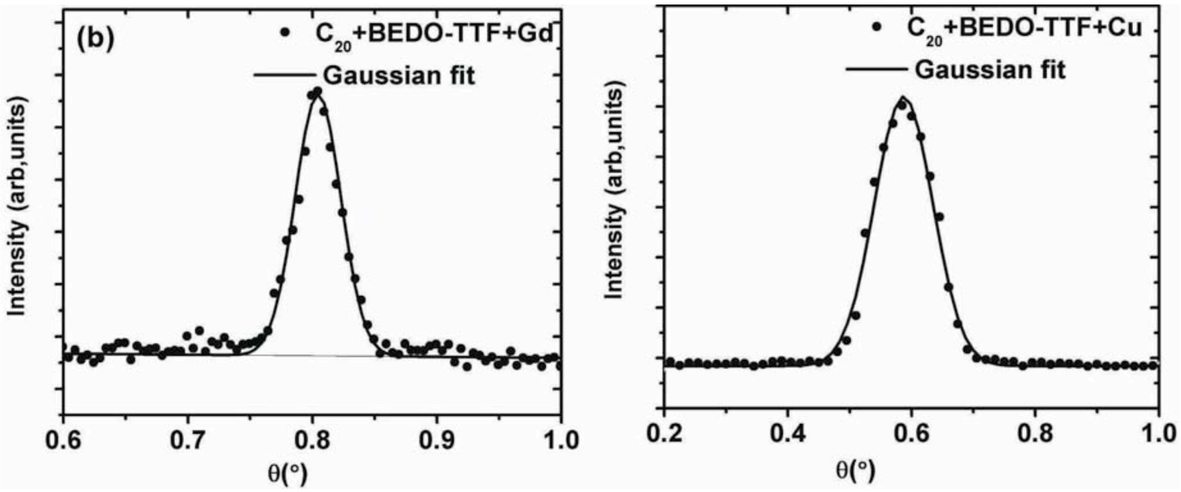

Figure 6. Rocking curves at the (001) peak position from 22-layer thick LB films of C_{20} + BEDO-TTF + Gd and C_{20} + BEDO-TTF + Cu.

Conclusions:

Hybrid LB films were studied to determine the homogeneity of the crystalline phase and orientation relation between individual layers within the film structure. All films showed a homogenous crystalline structure with very good stacking of the individual sheets. Moreover, the diffraction data were the same when measured in humid (70-90%) and dry conditions (not shown here) testifying to the stability of the films. In conclusion, the high X-ray flux together with the optimum diffraction geometry allowed us to extract information on the crystalline structure of hybrid LB films that were not possible to obtain by a typical laboratory thin film X-ray diffractometer.

DETERMINATION OF ION TRACK RADII IN AMORPHOUS MATRICES BY GISAXS

M. Buljan[1], I. Bogdanović-Radović[1], M. Karlušić[1], M. Jakšić[1], S. Bernstorff[2] and N. Radić [1]

1.) Ruđer Bošković Institute, Bijenička cesta 54, 10000 Zagreb, Croatia
2.) Elettra - Sincrotrone, SS 14, km 163.5, 34149 Basovizza, Italy

Ion beam irradiation of materials is powerful tool for the manipulation of material properties and formation of various nano-objects and three-dimensionally ordered nano-structures [1,2]. The interaction of ion beams with material is based on two main effects: electronic stopping (*Se*) and nuclear stopping (*Sn*). The former one is especially important since it causes local heating of the material in a narrow region around the ion trajectory [2]. This part of the material close to the ion trajectory, which is affected by the ion passage, is called ion track. The experimental determination of ion tracks radii in amorphous materials is very important since it enables the prediction and modeling of the structural properties of the irradiated materials.

The determination of the radii of ion tracks in amorphous materials is a hard task, especially for ion types that do not cause melting of the material, because of the lack of a straightforward method for their observation. High-resolution transmission electron microscopy is very useful in determining ion track radii in crystalline systems, because the interaction of the ion-beam with such material usually causes its amorphization. However, the same method is not always efficient in amorphous systems because the ion track and the surrounding material are of the same type. Another method usually applied is small angle x-ray scattering (SAXS). It gives structural data in the reciprocal space with excellent statistics. However, the problem often encountered with applications of this technique is the very small difference in the electron density between the track and surrounding material. This occurs because both track and surroundings usually have the same composition and only a slightly different density. The SAXS intensity is proportional to the electron density difference, so if it is very low, the method cannot be applied. Some other, indirect methods may be complicated because of the very short duration of the temperature pulse (in the ps range).

In Ref. [3], we have shown that it is possible to use an amorphous material (matrix) containing a small amount of foreign atoms that easily diffuse and form clusters during temperature increases caused by passage of the ion for the determination of ion track radii. Formed clusters have a different electron density than that of the matrix and produce a strong scattering of x-rays, so they are easily observed using grazing incidence small angle x ray scattering (GISAXS). The separations between the clusters are related to the ion track radii (*R*), so from the separations of the clusters (denoted by *L*) formed by the passage of ion types having different *Se* (and small *Sn*) through the same material it is possible to determine the ion track radii. The relation connecting the cluster separations (L=2R according to the Monte-Carlo simulation given in Ref.[3]) and main parameter of the ion track radius (a) is given by:

$$a^2=(R_2^2-R_1^2)/\ln(Se_2-Se_1) \qquad (1)$$

for the simple case when two ion types are used. More details about the model and the relation of the ion track width and temperature are given in Ref. [3].

To test the efficiency of the proposed method we have prepared amorphous SiO_2 films containing 7% of Ni atoms. The films were irradiated with two ion types having different *Se* and a small value of *Sn*. Thin films consisting of 20 alternating Ni+SiO_2 and SiO_2 layers were produced by magnetron sputtering deposition on Si(111) substrate. The deposition was performed at room temperature using a KJLC-CMS 18 magnetron sputtering deposition system. The irradiation with Oxygen ions was performed at the 6 MV Tandem Van de Graff accelerator at the Ruđer Bošković Institute with two different energies: 3 MeV and 2 MeV, causing electronic stopping Se_1 = 1.84 keV/nm and Se_2 = 1.58 keV/nm respectively. The structural properties of the films were determined by the GISAXS technique, performed at the synchrotron Elettra (Trieste), at the SAXS beamline, with a photon energy of 8 keV and with a two-dimensional photon detector.

Due to different values of the electronic stopping, the effects of the irradiation with two Oxygen ion types on $(Ni+SiO_2)/SiO_2$ films are different: the ion track radii differ and consequently the separations between the formed Ni clusters. GISAXS is an ideal tool to see these differences. GISAXS intensity distributions of the irradiated films are shown in Figure 1 (a),(b). From the positions of the lateral maxima in the GISAXS intensity distributions (denoted by arrows) it is obvious that the separations between the clusters are different. To obtain the real values of the cluster separations we have analyzed the measured GISAXS maps using a paracrystal model, specially adopted for the irradiated materials, described in detail in Ref. [4]. We found the mean separation between clusters L_1=3.3±0.2 and L_2 =4.3±0.2 nm for 2 MeV O and 3 MeV O, respectively. Assuming $L=2R_{\text{ion}}$, we get the radii of the tracks R_1 =1.7±0.1 nm, and R_2 = 2.1±0.1 nm. Using the obtained values and Eq.(1), we calculate the parameter a =3.5±0.5 nm.

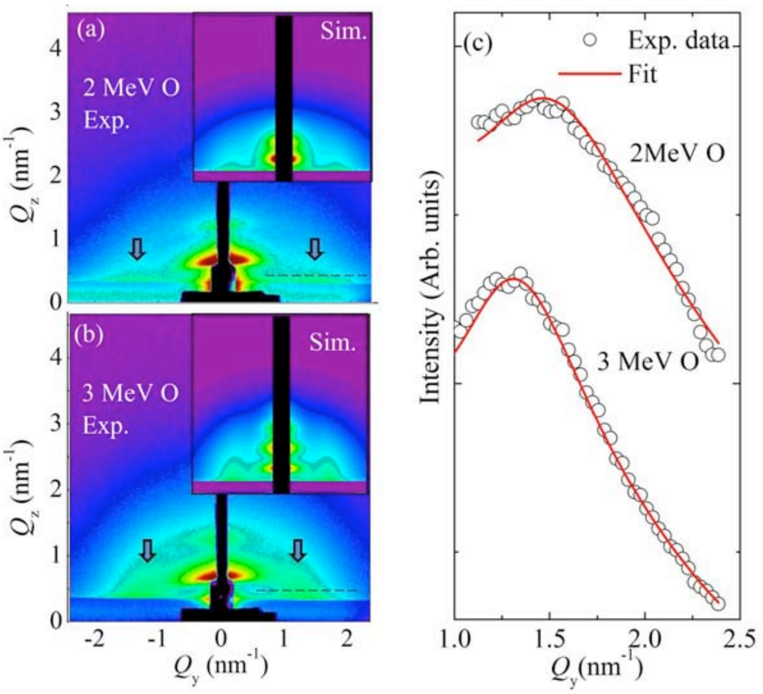

Figure 1. (a),(b) GISAXS maps of films irradiated by 2 MeV and 3MeV Oxygen ions (indicated in the figure). The insets show the simulated GISAXS maps obtained by fitting of the measured spectra.
(c) Intensity profiles (circles) taken along the lines indicated in the panels (a) and (b) together with the corresponding fit (solid lines)

The proposed method is very applicable and useful in predicting temperatures inside the ion tracks over a broad range, and for the design of the QD-based materials by ion-beam irradiation.

References:

[1] M. Buljan, I. Bogdanović-Radović, M. Karlušić, K. Salamon, G. Dražić, U.V. Desnica, N. Radić, S. Bernstorff, M. Jakšić and V. Holý, Phys. Rev. B **84**, 15531 (2011)
[2] I. Bogdanović-Radović, M. Buljan, M. Karlušić, N. Skukan, I. Božičević, M. Jakšić, G. Dražić and S. Bernstorff, Phys. Rev. B, **86** 165316 (2012)
[3] M. Buljan, M. Karlušić, I. Bogdanović-Radović, M. Jakšić, K. Salamon, S. Bernstorff, N. Radić, Appl. Phys. Lett. **101**, 103112 (2012)
[4] M. Buljan, N. Radić, S. Bernstorff, G. Dražić, I. Bogdanović-Radović, V. Holý, Acta Cryst. A **68**, 124 (2012)

SMALL-ANGLE X-RAY SCATTERING IN SOFT NANOCOMPOSITES, MAGNETOELECTRICS AND ELASTOMERS

G. Cordoyiannis[1], M. Lavrič[1], D. Jesenek[1], U. Puc[2], M. Jagodič[3,4], S. Gyergyek[5], H. Amenitsch[6], and A. Zidanšek[1,2,3]

1.) Condensed Matter Physics Department, Jožef Stefan Institute, Jamova 39, 1000 Ljubljana, Slovenia
2.) Jožef Stefan International Postgraduate School, Jamova 39, 1000 Ljubljana, Slovenia
3.) Faculty of Natural Sciences and Mathematics, University of Maribor, Koroška 160, Maribor, Slovenia
4.) Institute of Mathematics, Physics and Mechanics, Jadranska 19, 1000 Ljubljana, Slovenia
5.) Materials Synthesis Department, Jožef Stefan Institute, Jamova 39, 1000 Ljubljana, Slovenia
6.) Institute of Inorganic Chemistry, Graz University of Technology, Stremayrgasse 9/IV, 8010 Graz, Austria

The structural behavior of various soft nanocomposites (liquid crystals and nanoparticles) and liquid crystal elastomers has been measured. We have measured the thickness of smectic layers of liquid-crystalline phases, as well as the trends in the intensity and full-width at half maximum of quasi-Bragg peaks as a function of temperature. Moreover, we have probed the average size and size distribution of nanoparticles dispersed in liquid crystal hosts. In this way the phase transition behavior and the nanoparticle-induced liquid-crystalline phases have been probed. We mainly had three types of samples, as described in the following paragraphs.

a) Measurements of liquid crystals in order to obtain the temperature profiles of the order parameter (tilt angle for the SmA-SmC* transition) and compare it with the respective profiles of magnetic susceptibility in the search of soft magnetoelectrics.

b) Measurements of liquid crystal elastomers, which are binary soft systems, composed either of crosslinked polymer network and mesogenic molecules attached to the polymer chain or liquid crystal polymers, crosslinked with mesogenic or nonmesogenic units. We measured the temperature profiles of the order parameter in the vicinity of the Nematic-to-SmA transition.

c) Measurements of liquid crystals and isotropic (spherical) or anisotropic (platelet) nanoparticles. Samples: CE8 + Graphene nanosheets , where we explored the possibility of graphene assembly within the smectic phases [1]. CE + CdSSe nanoparticles in order to confirm the presence of TGB$_A$ phases from trends in the intensity (*I*) and full-width at half-maximum (*FWHM*) of the quasi-Bragg smectic peaks. This is a continuation of our previous work on nanoparticle-induced TGB$_A$ phases (data obtained at ELETTRA during 2010) [2]. The TGB order is confirmed by specific trends in *I*, *FWHM* as shown in Figure 1.

In addition, one manuscript was submitted and published in 2012 based on our 2010 measurements in liquid crystals confined in controlled-pore glass matrices [3].

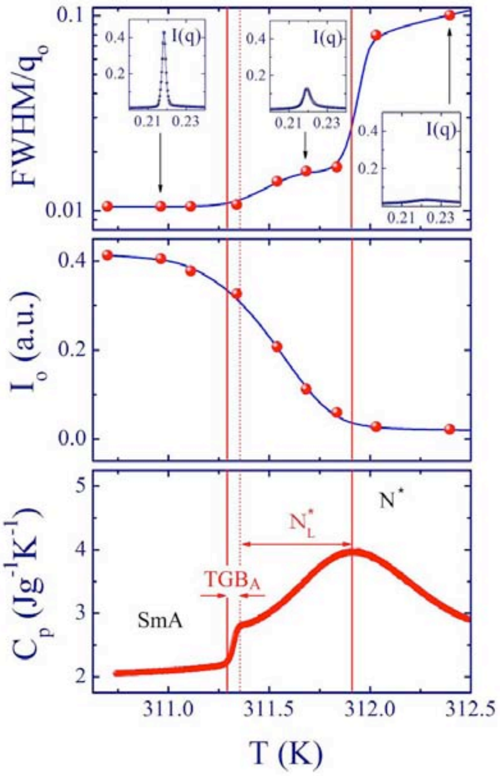

Figure 1. The trends of *FWHM* and *I*, as a function of temperature, confirm the presence of TGB_A phase indicated by high-resolution calorimetric measurements.

References:

[1] M. Lavrič, V. Tzitzios, S. Kralj, G. Cordoyiannis, I. Lelidis, G. Nounesis, V. Georgakilas, H. Amenitsch, A. Zidanšek and Z. Kutnjak; The effect of graphene on liquid-crystalline blue phases; Appl. Phys. Lett., under review (2013)

[2] G. Cordoyiannis, V.S.R. Jampani, S. Kralj, S. Dhara, V. Tzitzios, G. Basina, Z. Kutnjak, G. Nounesis, C.S.P. Tripathi, P. Losada-Perez, D. Jesenek, C. Glorieux, I. Muševič, A. Zidanšek, H. Amenitsch and J. Thoen; Different kinds of topological defects stabilized by adaptive targeting nanoparticles; Soft Matt. **9**, 3956-3964 (2013)

[3] S. Kralj, G. Cordoyiannis, D. Jesenek, A. Zidanšek, G. Lahajnar, N. Novak, H. Amenitsch and Z. Kutnjak; Dimensional crossover and scaling behavior of a smectic liquid crystal confined in controlled-pore glass matrices, Soft Matt. **8**, 2460-2470 (2012)

SILVER NANO PARTICLES FOR FUTURE PHOTOVOLTAIC APPLICATIONS

P. Dubček[1], B. Pivac[1], N. Radić[1] and S. Bernstorff[2]

1.) Ruđer Bošković Institute, Bijenička 54, 10000 Zagreb, Croatia
2.) Elettra - Sincrotrone Trieste, SS 14, km 163.5, Basovizza (TS), Italy

It is known that Ag nanoparticles embedded in the photoactive layer of a bulk heterojunction enhance the efficiency of photovoltaic devices. Doping with plasmonic nanoparticles leads to a power conversion efficiency improvement that can reach 20%. A good control of the size and space distribution is crucial for future device applications.

Here we report the investigation of post-annealed magnetron sputtered silver thin film on monocrystalline silicon. The deposition was carried out at room temperature, and the samples were annealed up to 650 ºC for one hour. GISAXS was employed in the size and size distribution investigation. Since the samples consist of nano islands on a flat substrate, the data were taken at the critical grazing angle of incidence.

As an example, GISAXS pattern from samples of 10 nm (left) and 20 nm (right) nominal thickness of Ag is shown in Figure 1. The samples were annealed at 650 ºC. The experimental data are shown in the left half of each image, while the right part is the result from data fitting to a size distribution of hemispheres. The relevant fitting parameters are shown in table 1. Obviously, the particle size is not a simple function of the nominal film thickness: some silver is lost during the annealing process, and this is more significant for thinner initial thickness. The average particle sizes are similar to the film thickness for thinner initial layers, while they tend to overgrow the film thickness for the thicker ones.

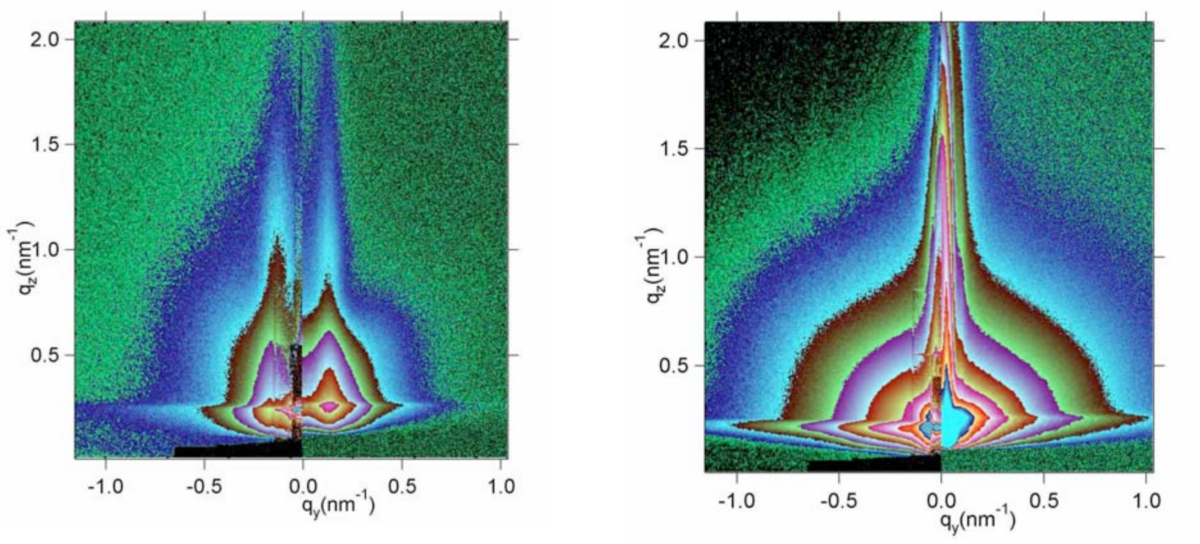

Figure 1. GISAXS intensities for 10 nm (left) and 20 nm (right) nominal thickness of Ag deposited on monocrystalline Si substrate. The left side of each of the images is the color-coded measured intensity, while the right side shows the calculated intensity.

A thinner initial film leads to a better uniformity regarding the particle height, but the in-plain size distribution width amounts to half the average particle size. When normalized to the average particle size, the horizontal size distribution is narrower for thicker film. This holds true also for the interparticle distance.

Our two examples fall into two different potential designs, and both can potentially enhance the light absorption efficiency in a photovoltaic cell. For the thicker initial layer (particle radius R ~ 50 nm, see Table 1.), light scattering from large metal nanoparticles (diameter >50 nm) falls into high angles inside the photoactive layer, causing increased optical path lengths in the device, while for the smaller inital thickness (particle radius ~ 10 nm) the plasmon resonance induced by the small diameter (5–20 nm) metal particles causes a local field enhancement.

Table 1. Results of the fitting to a hemisphere model: R is the radius, H the height and D the interparticle distance. These parameters are mean values from a normal size distribution, and dR, dH and dD are respectivly the halfwidths of these distributions.

Sample	R (nm)	dR (nm)	H (nm)	dH (nm)	D (nm)	dD (nm)
10	8	4	10	1	35	4
20	50	10	50	12	250	25

Generally, we found that optimal sizes and narrow size distributions were obtained for higher annealing temperatures and thinner initial thickness of the silver layer. However, high annealing temperatures are prohibitive when Ag nanoparticles are realized within a silicon heterojunction. On the other hand, when annealed at temperatures up to 150 ºC, the silver layer transforms into a wide size distribution of nanoparticles, with much smaller interparticle distances. Some compromise will be necessary for functional device production.

THE INFLUENCE OF THERMAL ANNEALING ON NANO-STRUCTURES IN THIN FILM SOLAR CELLS MATERIALS

D. Gracin [1], K. Juraić[1], P. Dubček[1], A. Gajović[1], S. Bernstorff[2] and M. Čeh[3]

1.) Rudjer Boskovic Institute, Bijeička 54, 10000 Zagreb, Croatia
2) Elettra-Sincrotrone Trieste, SS 14, km 163.5, 34149 Trieste, Italy
3) Jožef Stefan Institute, Jamova 39, 1000 Ljubljana, Slovenia

Hydrogenated amorphous-nano-crystalline Si, a-nc-Si:H, is a promising material for high efficiency solar cells. In order to test the stability of this kind of material and examine the possibilities of post-deposition treatment the as deposited samples were exposed to isochronal thermal annealing. Samples were prepared by PECVD using a highly diluted mixture of silane by hydrogen on glass substrate [1, 2] and exposed to post-deposition thermal treatment in hydrogen atmosphere for one hour at three different temperatures: 200 °C, 300 °C and 400°C. The structure of as deposited and annealed films was examined by high-resolution electron microscopy (HRTEM), Grazing Incidence Small Angle X-ray Scattering (GISAXS), Grazing Incidence Wide Angle x-ray Scattering (GIWAXS) and Raman spectroscopy.

A typical HRTEM micrograph of as deposited films is plotted in Fig.1. The borders of the crystals are marked by a line for better visibility. The crystals are separated from each other which allows using the Guinier approximation in the GISAXS patterns analysis. The average crystal sizes were between 5 and 8 nm with a broad log-normal type distribution, assuming random nucleation and growth of crystals [3].

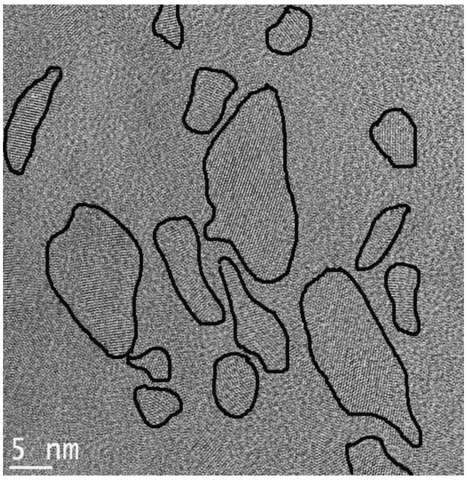

Figure 1. HRTEM micrograph of a typical sample. The borders of the nano-crystals are marked by a line

The GISAXS experiment was done at the SAXS beam line using 8 keV radiation and a camera length of approximately 2m. Because of the non homogenous sample structure the angle of incidence was varied in small steps starting from the critical angle for total external reflection α_c up to $\alpha_c+0.25°$, which enabled to study the changes induced by the heat treatment in various depths of the examined samples e.g. for various initial structures. The GISAXS pattern showed that the films contained particles with average sizes ($2*R_{gav}$) similar to those estimated by HRTEM (D_{HRTEM}), as seen from Fig 2.

The analysis of the width of the GIWAXS diffraction lines confirmed that crystals are as small as expected from HRTEM. The Rietveld analysis showed that the broadening of characteristic lines in GIWAXS was due to the nano-size of the crystals and additionally due to the strain present in the samples [4]. After thermal treatment, the width of characteristic peaks in GIWAXS spectra changes, while the gyro radii in GISAXS remain the same. This indicated that the crystals sizes remain the same while the strain changed. This result is consistent with Raman spectra where the TO phonon peak shifts towards lower frequencies

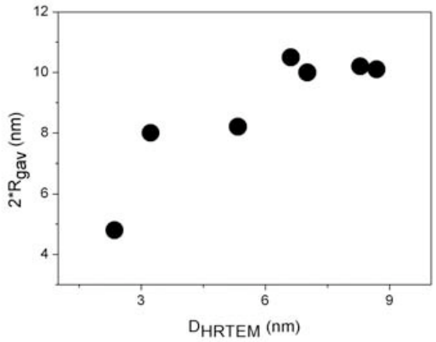

Figure 2. Particle sizes estimated from GISAXS using the Guinier approximation, 2*R_{gav}, versus average crystal sizes estimated from HRTEM micrographs, D_{HRTEM}

Figure 2. Particle sizes estimated from GISAXS using the Guinier approximation, 2*R_{gav}, versus average crystal sizes estimated from HRTEM micrographs, D_{HRTEM}

with heath treatment, indicating a change of strain. The GISAXS patterns in the Porod range showed that the initial slope of the log (I) versus log (q) curve changed from values above 4 towards lower values which indicates that the interfaces between particles and surrounding matrix became more defined. This is also seen from the x-ray reflectivity of the samples (Fig 3). With heath treatment the amplitudes became larger, indicating better defined interfaces.

After thermal treatment, the critical angle for total external reflection increased gradually indicating an increase of the mass density, as seen from Fig. 3.

The observed changes of the structural properties will be correlated with changes in the optical properties and discussed as a consequence of hydrogen effusion and redistribution in the film since the hydrogen concentration gradually decreases during annealing from some 12-15 at% for as deposited samples towards 4-5% in samples annealed at 400^0C.

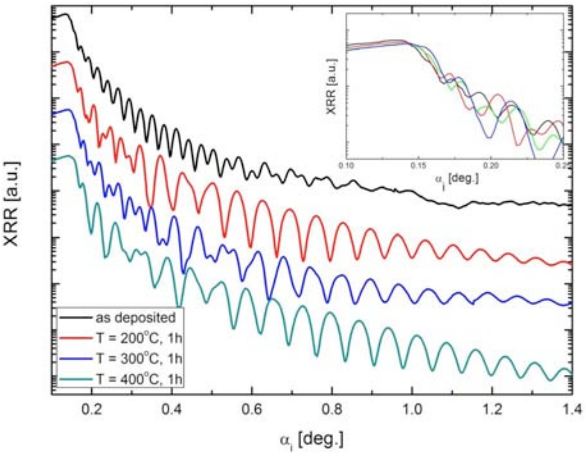

Figure 3. The x-ray reflectivity of as deposited sample (black line) and samples after heath treatment at various temperatures (coloured lines). The insert shows the extended part of the graphs for smaller incidence angles

References:

[1] D. Gracin, S.Bernstorff, P.Dubček, A.Gajović, K.Juraić, Study of amorphous nanocrystalline thin silicon films by grazing- incidence small-angle X-ray scattering, Journal of Applied Crystallography **40** (2007) S373–S376

[2] D. Gracin, S.Bernstorff, P.Dubček, A.Gajović, K.Juraić, The influence of substrate morphology on growth of thin films by GISAXS, Thin Solid Films **515** (2007) 5615-5619

[3] K. Juraić, D.Gracin**,** B.Šantić, D.Meljanac, N.Zorić, A.Gajović, P.Dubček, S.Bernstorff, M.Čeh, GISAXS and GIWAXS analysis of amorphous-nanocrystalline silicon thin films, Nuclear Inst. and Methods in Physics Research, B. **268** (2010) 259-262

[4] K.Juraić, D.Gracin, I.Djerdj, A.Lausi, M.Čeh, D.Balzar, Structural analysis of Amorphous-Nanocrystalline Silicon Thin Films by Grazing Incidence X-ray Diffraction, Nuclear Inst. and Methods in Physics Research, B. **284** (2012) 78**-**82

MONITORING THE ONSET OF COLLOIDAL CRYSTALISATION BY *IN-SITU* SAXS

R.T. Lechner[1], C. Prehal[1], H. Amenitsch[2], M. Yarema[3,4], W. Heiss[3] and O. Paris[1]

1.) Institute of Physics, Montanuniversitaet Leoben, A-8700 Leoben, Austria
2.) Institute of Inorganic Chemistry, Technical University Graz, A-8010 Graz, Austria
3.) Institute of Semiconductor and Solid State Physics, Johannes Kepler Universitaet Linz, A-4040 Linz, Austria
4.) EMPA-Swiss Federal Laboratories for Materials Science and Technology, CH-8600 Dübendorf, Switzerland

Colloidal crystals using crystalline nanoparticles (NCs) as building blocks offer the opportunity for designing artificial solids with tailored properties [1].

In this work we monitor the onset of the crystallization process by in-situ SAXS measurements using a slow destabilization approach by diffusion of a non-solvent into the colloidal dispersion [2]. We followed two experimental schemes to study the ordering: First we create a single NC-solvent (= toluene) non-solvent (= ethanol) interface and measure the SAXS signal as function of time and hence, as function of the ethanol concentration within the NC-toluene solution. Thus we can correlate the appearance of the structure factor peak and its change in position to the amount of ethanol.

In the second setup, after fast mixing defined amounts of NC-solution with ethanol, we follow the variation of the scattering pattern as function of time at *constant* ethanol fraction.

We continued the research with Bi-nanocrystals and developed a two-syringe mixing system for fast mixing of defined amounts of NC-solution with the non-solvent ethanol. This system allows also to create a better defined solvent/non-solvent interface as previously investigated (see Annual Report 2011). Furthermore, we extend the measurement series using also semiconducting PbS nanocrystals for our colloidal crystallisation experiments. The PbS-NC diameter of 3.6 nm with a size distribution of around 8% was derived from SAXS measurements on pure PbS-NC solutions in toluene (e.g. topmost scan in Fig.1a).

After injecting first 600 µl ethanol, followed by 200 µl PbS-NC solution we established an interface with defined volumes of solvent and non-solvent and measured just below this interface within the NC solution (see inset Fig.1a). By recording continuously SAXS spectra every minute the evolution of a correlation peak with increasing time is visible. This peak is more clearly visible in the experimental structure factor, which is derived by dividing all measured spectra by the first spectrum representing the form factor of the single particle (see Fig.1b). From the position of the peak we can conclude on an average particle-particle distance of around 5.4 nm that is significantly larger than the PbS-NC diameter. This is an indication for a densely packed, but not very well ordered system, where the organic ligands around the NCs still acts as spacers.

For a more quantitative analysis, we measured simultaneously the transmission through the solvent/non-solvent solution (blue line in Fig. 1c) and can hence derive the toluene and ethanol fraction (green and red line) as a function of time. In Fig. 1d we combine the derived ethanol fraction with the integrated correlation peak intensity derived from the peak-area. From this, we can directly relate the first appearance of the correlation peak to a non-solvent concentration of around 35%. The peak intensity and the ethanol fraction increases with time, but the ethanol concentration reaches its maximum value of around 40% after 60 minutes, while the correlation peak intensity still increases. A quite constant maximum peak value is reached, however, only after 2 hours reaction time. This proves that the colloidal crystallisation process is initialised by a critical amount of non-solvent fraction, but continues even at a constant non-solvent concentration within the NC-solution.

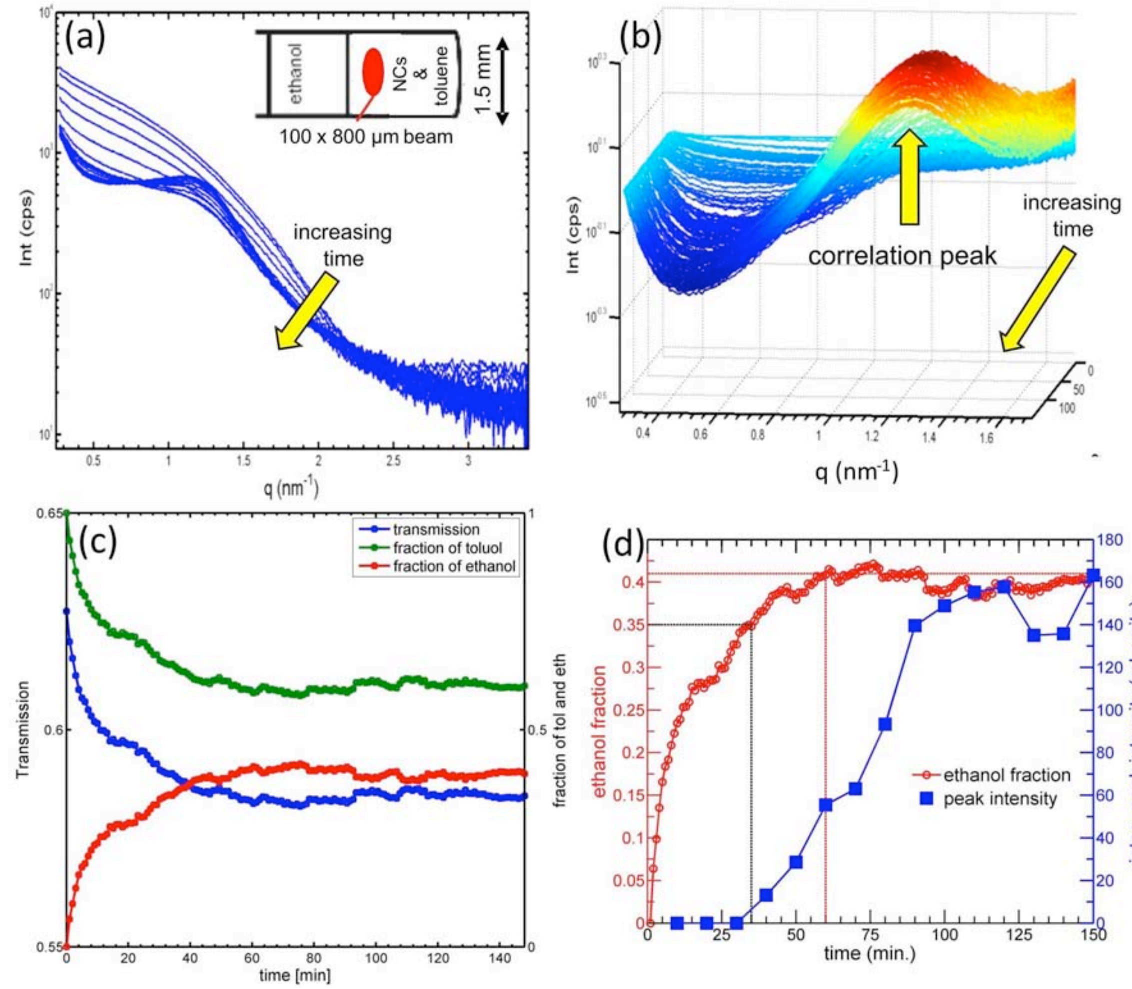

Figure 1. (a) SAXS spectra as a function of time with the x-ray spot position close to the solvent (=toluene) / non-solvent (=ethanol) interface within the PbS-nanocrystal solution (see inset). (b) Experimental structure factor as a function of time. (c) The measured transmission (blue) versus time together with the derived toluene (green) and ethanol (red) fraction at the position of the x-ray beam. (d) The ethanol fraction (left) together with the integrated correlation peak intensity (right) versus time. The black dashed line marks the appearance of the correlation peak at 35% ethanol fraction. The red dashed line marks the time, when the maximum ethanol value of around 40% is reached.

Especially, the further evolution of the ordering process can be studied with the second experimental setup, where the SAXS patterns as a function of time were measured after fast mixing defined amounts of NC-solvent and non-solvent. Further experiments were performed for PbS-NC as well as Bi-NC solutions with various concentrations and different solvent/non-solvent ratios. All these data will be related over the transmission data to the exact ethanol and particle concentrations. Thus we can study independently three important parameters that influence the colloidal crystal formation, i.e., the non-solvent concentration within the nanocrystal solution, the growth time as well as the amount of NCs in the initial solution.

References:

[1] Talapin, D.V., MRS Bull. 37, 63-71 (2012)
[2] Yarema, M., Kovalenko, M.V., Hesser G., Talapin, D.V., Heiss W., JACS 132, 15158–15159 (201014310)

REAL TIME INVESTIGATION OF CRYSTALLIZATION AND AGGREGATION DYNAMICS IN AMBIPOLAR SEMICONDUCTIVE POLIMER DURING THERMAL ANNEALING

F. Liscio[1], L. Ferlauto[1], S. Milita[1], D. Gentili[2], M. Cavallini[2], P. Sonar[3] and A. Dodabalapur[3,4]

1.) Istituto per la Microelettronica e i Microsistemi, IMM-CNR, Via Gobetti 101, I-40129, Bologna
2.) Istituto per lo Studio del Materiali Nanostrutturati, ISMN-CNR, Via Gobetti 101, I-40129, Bologna
3.) Institute of Materials Research and Engineering (IMRE), Agency for Science, Technology and Research (A*STAR), 3 Research Link, Singapore 117602
4.) Microelectronics Research Centre, The University of Texas at Austin, Austin, Texas 78758, United States

The structure and morphology of a new ambipolar polymer semiconductor have been investigated *in-situ* and in real time during thermal treatment. A diketopyrrolopyrrole-based polymer (PDPP-TBT, Figure 1) was chosen due to its high and balanced hole and electron mobilities measured in organic thin film transistor (OTFT) devices [1-2]. In particular, thermal treatments of PDPP-TBT films lead to the highest performance among all ambipolar OTFTs reported.

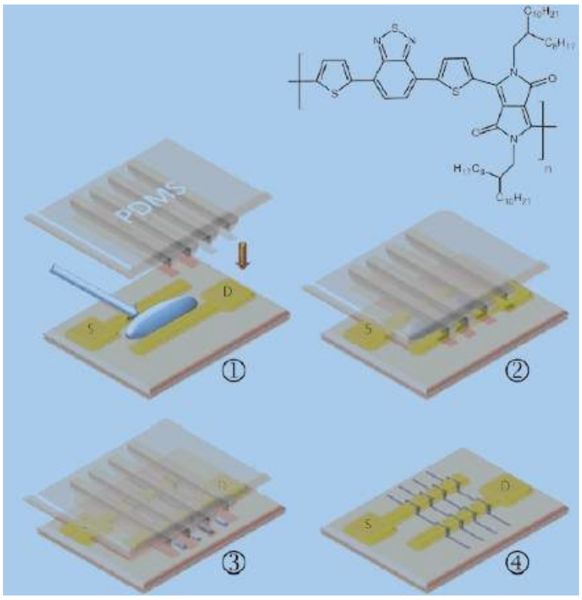

Figure 1. Scheme of lithographically controlled wetting (LCW). In LCW, a polymeric stamp with parallel protrusions is placed in contact with a PDPP-TBT solution film spread on 150 nm high interdigitated gold electrodes of a FET/inverter test structure. As the solution volume gradually shrinks, the capillary forces drive the formation of menisci pinned only under the stamp protrusions. When the solvent has completely evaporated, nanostripes of solute form in between interdigitated electrodes. The inset shows the chemical structure of PDPP-TBT.

Three series of samples were prepared by different solution processes: drop and spin castings, and lithographically controlled wetting (LCW), which is a method for creating highly reproducible nanopatterns with precisely controlled dimensions (Figure 1) [3]. LCW has already proven to be a powerful tool for improving the crystallinity, the electrical properties [4], and in some cases driving the crystal orientation [5].

The structural characterization of the pristine sample was performed by keeping it in air and by collecting GIWAXS images on an image plate detector able to explore a large q-space range. *In-situ* and real time GIWAXS measurements were performed mounting the sample inside a chamber suitable for annealing until around 200°C under N_2 atmosphere and using a Pilatus detector characterized by a small q-range window and a fast acquisition time, which allowed the kinetic of crystallization to be characterised in real time. After the thermal treatment and the cooling to room temperature, each sample was investigated using the same set-up of the pristine characterization.

In-situ and real time GISAXS measurements under thermal annealing in N_2 atmosphere were carried out using the CCD camera.

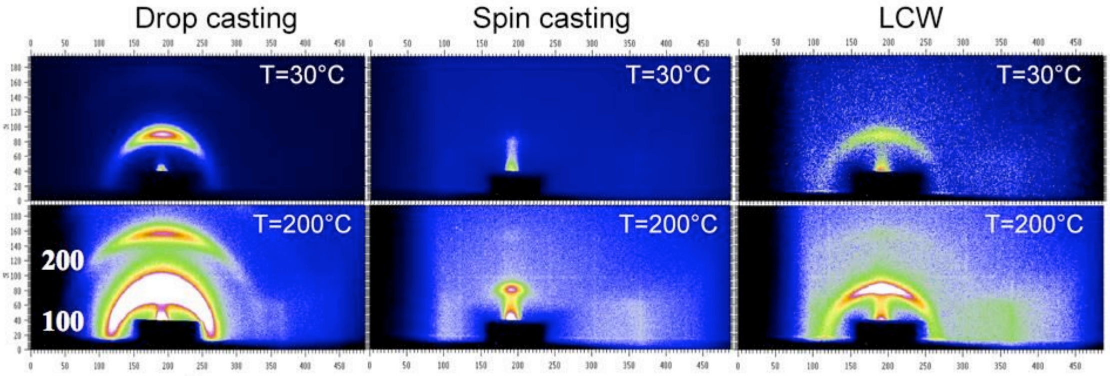

Figure 2. 2D-GIWAXS detector images collected for PDPP-TBT films prepared by drop and spin casting and LCW, before and after 15min of thermal treatment at 200°C. The axis labels correspond to the pixel values of the PILATUS detector.

Figure 2 shows the 2D-GIWAXS detector images of the films prepared by drop casting, spin casting and LCW before and after 15 min. of thermal treatment at 200°C. The observed different patterns are clear evidence that the crystal structure of the films strongly depends on the preparation method. Although no crystalline order is observed in the spin cast film, the appearance of the (100) reflection after annealing indicates that the polymer self-organises in crystalline grains with highly ordered *layer-by-layer* lamellar packing motif, with an edge-on orientation. The high crystalline degree is marked by the sharpness of the corresponding Bragg peak. Conversely, both pristine films prepared by drop casting and LCW are characterized by a crystalline order, as shown by the presence of the (100) reflection. The arc shape of the Bragg peak indicates a high mosaicity, i.e. a large misorientation of crystalline grains. After the thermal annealing process, an increase of the amount of crystalline grains occurs, as indicated by the more intense peak and the appearance of (200) reflection, although a high mosaicity still persists. The difference in the peak intensity between the drop casted and LCW films can be ascribed to the different film thickness, which is typically of dozens of μm for drop casting samples and dozens of nm for LCW samples. The differences in crystalline order before and after thermal annealing explains the electrical response of the OFETs devises fabricated under the same preparation conditions. Mobility measured on LCW OFET both before and after thermal annealing is higher than that of the spin-coated OFET. The nanoconfinement induced by LCW improves crystallinity and fiber orientation of the active material, which results in high balanced hole and electron field-effect mobility, both of them around 1 $cm^2 V^{-1}s^{-1}$, which are among the highest values measured for thin film transistors made of ambipolar organic semiconductors [6].

During the thermal annealing several GIWAXS and GISAXS images were collected. The evolution of the structural parameters and the lateral size of PDPP-TBT fibres will be extracted from the analysis of vertical cuts of the GIWAXS images and horizontal cuts of the GISAXS images, respectively. As an example, Figure 3a reports the vertical cuts of the GIWAXS images recorded at different temperatures for the spin cast film, showing an increase of the Bragg reflection intensity. The evolution of the domain size and the (100) peak position *vs* the annealing time, compared with the annealing temperature (Figure 3b), underlines that the crystallinity reaches the highest order already at 100°C.

The proper analysis of the combined GIWAXS and GISAXS data is being carried out together with the analysis of the electrical properties of OFET devices measured during thermal treatment. The results obtained from the in-situ and real time experiments are the only way to probe the direct connection between crystal order, lateral size and mobility parameters, which is still not properly acquired nowadays.

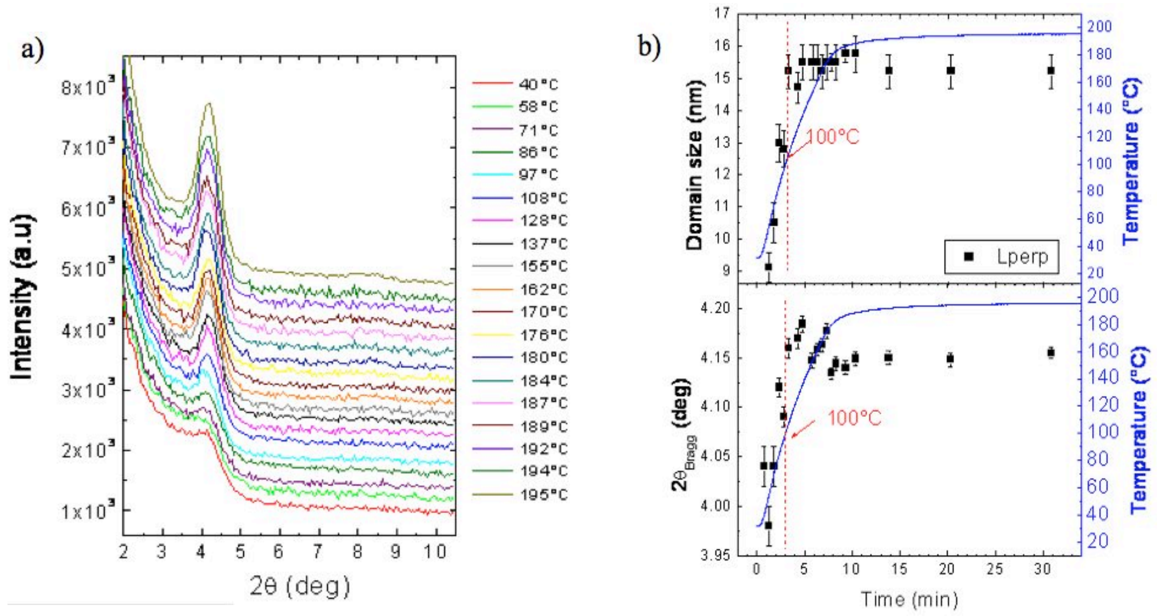

Figure 3. a) Vertical cuts of the 2D GIWAXS images registered at different temperatures for spin casting PDPP-TBT films. **b)** Domain size and (100) peak position trend *vs* annealing time, compared with the annealing temperature ramp (blue line).

References:

[1] P. Sonar, S. P. Singh; Y. Li, M. S. Soh and A. Dodabalapure, Adv. Mater. 22, 5409–5413 (2010)
[2] T.J. Ha, P. Sonar, B. Cobb, A. Dodabalapur, Organic Electronics 13, 136–141 (2012)
[3] M. Cavallini, D. Gentili, P. Greco, F. Valle F. Biscarini,, Nat. Protoc., 7, 1668−1676 (2012)
[4] M. Cavallini, P. D'Angelo, VV Criado, D Gentili, A Shehu, F Leonardi, S Milita, F Liscio, F Biscarini, Adv. Mater., 23, 5091−5097 (2011)
[5] D. Gentili, F. Di Maria, F. Liscio, L. Ferlauto, F. Leonardi, L. Maini, M. Gazzano, S. Milita, G. Barbarella, M. Cavallini, J. Mater. Chem., 22, 20852−20856 (2012)
[6] D. Gentili, P. Sonar, F. Liscio, T. Cramer, L. Ferlauto, F. Leonardi, S. Milita, A. Dodabalapur and M. Cavallini, Nano Lett., 13, 3643−3647 (2013)

GISAXS STUDY OF HYBRID FILMS OF METAL NANO-PARTICLES EMBEDDED IN ORGANIC SEMICONDUCTOR MATRICES

J. Novák[1], R. Banerjee[1], Y. Busby[2], D. Soraruf[1], H. Amenitsch[3], G. Casula[4], P. Cosseddu[4], S. Nau[5], S. Sax[5], E. J. W. List-Kratochvil[5], A. Bonfiglio[4], J.-J. Pireaux[2] and F. Schreiber[1]

1.) Institute of Applied Physics, Eberhard Karls Universität Tübingen, Auf der Morgenstelle 10, 72076 Tübingen, Germany
2.) Department of Physics, Université de Namur, Rue de Bruxelles 61, 5000 Namur, Belgium
3.) Institute of Inorganic Chemistry, Graz University of Technology, Stremayrgasse 9/IV, 8010 Graz, Austria
4.) Department of Electrical and Electronic Engineering, University of Cagliary, Piazza D'Armi, 09123 Cagliari, Italy
5.) NanoTecCenter Weiz Forschungsgesellschaft mbH, Franz-Pichler-Straße 32, 8160 Weiz, Austria

Hybrid films consisting of metal clusters embedded in an organic semiconductor matrix (OSM) are attractive for applications in non-volatile memory devices (NV-MD) [1, 2]. Here, a voltage or light stimuli [3] leads to charging of metal nanoparticles (NPs) from the surrounding OSM and a concomitant change of the film resistance. However, details of the charge transfer and charge retention are not yet theoretically described. Additional challenge is to optimize the physical properties of the hybrid structures, i.e., to obtain reproducible switching effect, maximize the ratio between switch-on/switch-off currents, and to maximize state-retention-time and the overall lifetime of the devices. Knowledge of the structural properties of the devices (or at least model samples) is needed to address the basic principles of the devices for optimization and fabrication.

We have performed grazing incidence small angle X-ray scattering (GISAXS) experiments on a series of samples of hybrid organic/inorganic thin films aimed for non-volatile memory devices. The intention is to cross-correlate the structural properties of the films with preparation protocols. The samples were prepared using various deposition methods and preparation conditions. Mainly, three of the series of samples were studied: 1) films with arrays of Al NPs evaporated at different deposition rates atop N1400 (purchased from Polyera Corp.) thin films of various thicknesses, 2) films with Al NPs evaporated on plasma treated tris(8 hydroxyquinolinato)-aluminium (Alq3), and 3) films with Al evaporated atop of plasma treated polymer Poly(3-hexylthiophene) (P3HT). The samples of the last two series were prepared at various metal deposition rates and the OSM was treated in argon or nitrogen atmosphere. Additionally, samples with gold NPs evaporated atop or embedded within the Alq3 OSM wafer were studied.

The GISAXS measurements were realized using Pilatus 100K CMOS hybrid pixel detector, allowing for high intensity dynamic range. In order to suppress radiation damage of the organic samples during the X-ray measurements [4], samples were kept in a protective nitrogen-atmosphere in a home build sample cell (University Tübingen) equipped with kapton windows for entry and exit of X-rays (see Fig. 1). The GISAXS measurements were performed at two incidence angles (α_i) for the samples with metal clusters on top surface of the OSM and 5 incidence angles (in the vicinity of the critical angle) for the samples with metal clusters buried within the OSM in order to achieve depth resolution via varying the X-ray penetration depth. Additionally, the GISAXS study was complemented by AFM and transmission electron microscopy measurements.

For all samples with Al evaporated atop N1400 (sample series 1) GISAXS provides a clear indication of Al cluster formation. The presence of the Al clusters is indicated by a broad diffuse scattering shoulder along $Q_{||}$, which is missing for samples without Al (see Fig. 2). The presence of the Al clusters is also visible in complementary AFM measurements. From AFM, we can quantify average size and nearest neighbor distance of the clusters to be 50 nm and 90 nm, respectively. The lateral size of the clusters is, however, beyond the resolution limit of the present GISAXS setup.

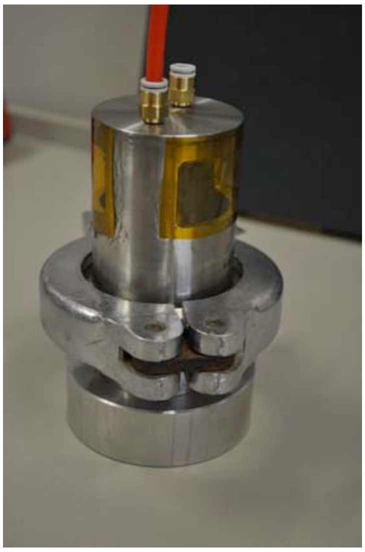

Figure 1. Sample cell used to suppress radiation damage of the samples during the X-ray measurements. The cell is equipped with entry and exit kapton windows and the gas inlets and outlets allow to keep the sample under nitrogen atmosphere.

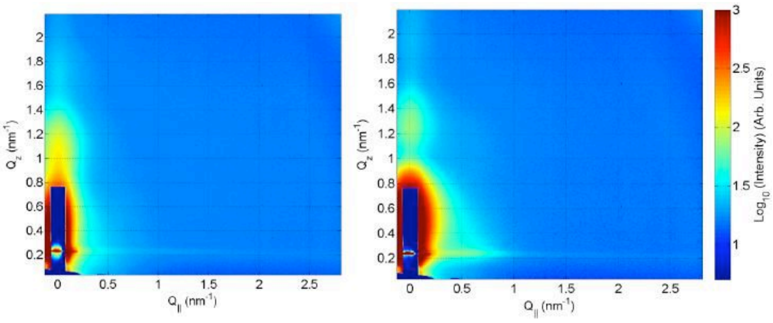

Figure 2. GISAXS images of a sample with N1400 thin film (left) and 15 nm of Al evaporated atop N1400 film (right). The broad diffuse scattering in the right image clearly indicates formation of Al clusters.

Similarly, for samples with 15 nm Al evaporated atop plasma treated Alq3 layers (sample series 2) GISAXS measurements indicate presence of the Al clusters. For samples treated with both plasma gases Ar and N2, broadened side shoulders are present in GISAXS images. However, the precise determination of the clusters' size is not feasible using the current measurements. Nevertheless, the observation is interesting, since for layers deposited at the same conditions atop of Alq3 without a previous plasma treatment, Al layer forms a continuous layer.

In contrast to the results for the previous two sample series, for the third series with Al deposited atop plasma treated P3HT polymer layers, no evidence of cluster formation is observed by GISAXS. This is, indeed, an important information, since cluster formation is believed to be a necessary prerequisite for functional hybrid organic/inorganic memory-device.

Interestingly, for samples with 3 nm of gold evaporated atop Alq3 OSM, we observe a regular array of clusters. This is evidenced by well pronounced side maxima in GISAXS images (Fig. 3). The average nearest-neighbor distance of the clusters is 10 nm and the average height of the clusters is approximately 4 nm, as determined from the GISAXS images. Additional Alq3 deposited atop Au clusters reproduces very well the surface profile of the clusters. The resonant diffuse maxima along the Q_z direction in the GISAXS image taken at incidence angle above the critical angle of the organic layer (see Fig. 3) provide clear evidence of such conformal growth. To sum up, 3 nm of Au deposited atop Alq3 form clusters and their surface structure is reproduced by overlaying Alq3 layer, whenever deposited.

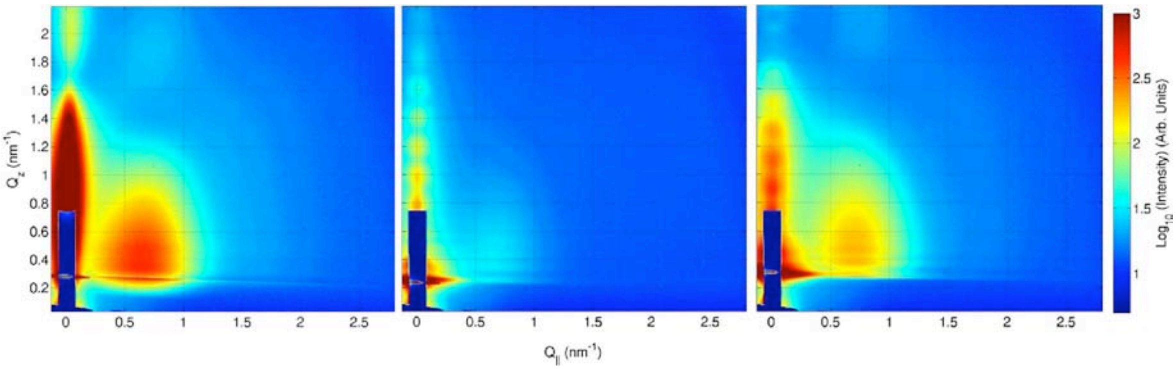

Figure 3. GISAXS images taken for sample with Au clusters evaporated on tris(8 hydroxyquinolinato)-aluminium (Alq3) organic semiconductor matrix at X-ray beam incidence angle of α_i=0.17° (left) and for sample with Au clusters embedded in Alq3 matrix: incidence angles of α_i=0.17° and α_i=0.22°, (middle and right, respectively).

In summary, we have studied series of samples with metal (Au or Al) deposited on top of organic semiconductor thin films (N1400, Alq3 or P3HT), which are relevant for hybrid non-volatile memory elements. For deposition of Al on top of N1400 and plasma treated Alq3, GISAXS experiments evidence formation of metal clusters, which is not the case for deposition on semiconducting polymer P3HT. Additionally, enhanced regularity in cluster spacing was observed for deposition of gold atop Alq3. The results of the X-ray measurements were compared to AFM data and the results play an important role in the sample growth process optimization. Additionally, the structural properties obtained from GISAXS experiments will be correlated to the devices properties, thus helping to understand switching effect in the hybrid memory devices.

References:

[1] J. Ouyang, C.-W. Chu, C. R. Szmanda, L. Ma and Y. Yang, *Nat. Mater.,* **3,** 918, (2004)
[2] V. Reddy, S. Karak and A. Dhar, *Appl. Phys. Lett.,* **94**, 173304, (2009)
[3] N. Koch, A. Dürr, J. Ghijsen, R. Johnson, J.J. Pireaux, J. Schwartz, F. Schreiber, H. Dosch and A. Kahn, *Thin Solid Films,* **441,** 145, (2003)
[4] A. Neuhold, J. Novák, H.-G. Flesch, A. Moser, T. Djuric, L. Grodd, S. Grigorian, U. Pietsch, and R. Resel, *Nucl. Instrum. Meth.* B 284, 64 – 68 (2012)
101 (2007) 114310

SAXS FROM FREE METAL CLUSTERS IN A MOLECULAR BEAM

P. Piseri[1], M. Devetta[1], H. Amenitsch[2]

1.) Dipartimento di Fisica & CIMaINa, Università degli Studi di Milano, via Celoria 16 - 20133, Milano, Italy
2.) Institute of Inorganic Chemistry, Graz University of Technology, Stremayerg. 9/IV, 8010 Graz, Austria

The study of isolated nanoparticles produced in the gas phase is a key issue for understanding how the properties of matter evolve from atomic and molecular level to bulk materials. Besides fundamental interest, a bottom-up approach to the development of novel materials exploiting the extraordinary physical and chemical properties of nanostructures, relies on the possibility of establishing clear relationship between the assembled materials and nanoscale building blocks. Controlled nanoparticle synthesis combined with manipulation and deposition stages thus plays a major role in the advancement of nanostrustructred materials production. Supersonic Cluster Beam Deposition [1] is a technique for thin films synthesis based on this approach. Access to information on free nanoparticle morphology, to their aggregate structure and possibly a fractal dimension, i.e. particle characterization beyond size is thus of major importance. Recently we developed a method, based on the low-pressure aerodynamic mobility of neutral particles, for the quantitative determination of a morphology descriptor of free clusters with complex nanostructure [2]. The possibility to compare the results obtained with this method with those given by a well established method such as SAXS, has stimulated our SAXS experiment.

Owing to the high cluster beam intensity and stability achievable with a Pulsed Microplasma Cluster Source (PMCS) [3], combined with aerodynamic focusing of particle trajectories in the subsonic part of the aerosol flow [4], a sample density in the range of 10^{14} atoms/cm^3 is typically obtained which is considered enough to allow performing time resolved SAXS and thus obtain structural information on the nanometric particles in the gas-phase taking "snapshots" at fixed stages of their growth and extraction from the source on a millisecond timescale [5].

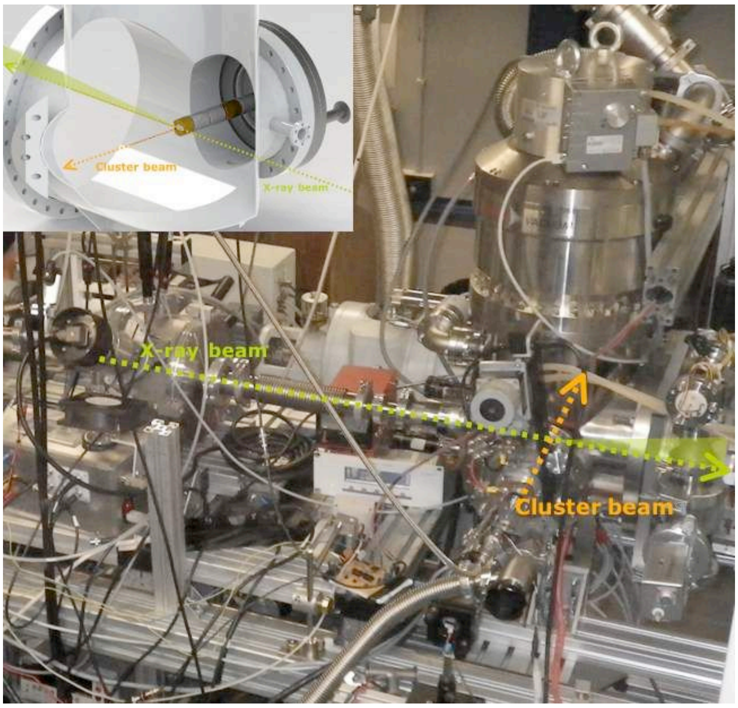

Figure 1. The experimental setup showing the high-vacuum cluster beam apparatus directly attached to the beamline. The inset is a rendering of the inside of the expansion chamber, showing a sketch of the experimental scheme.

In order to reduce background signal to a minimum, we attached the molecular beam apparatus directly to the SAXS beamline and thus kept the whole X-ray beam path under high vacuum until the 200 mm polyimide exit window just in front of the Dectris PILATUS 100K detector. A ~11 kHz background count rate has been obtained, corresponding to about 55 counts per frame at the timing scheme adopted for the experiment (5 ms exposure images, taking 8 frames - 9 ms spacing - per every single cluster beam pulse. 10 Hz rep. rate). The observed signal level is ~1.7 scattered photons per frame at maximum of pulsed beam intensity for Pb clusters in Ar carrier gas. Alignment of the system has been performed by measuring the deposited material on a thin Mylar disk inserted at 45° angle so to intersect both cluster and X-ray beams. The disk was rotating synchronously with the cluster beam pulses repetition, so to provide reference spectra for the deposited material corresponding to the gas phase experiments.

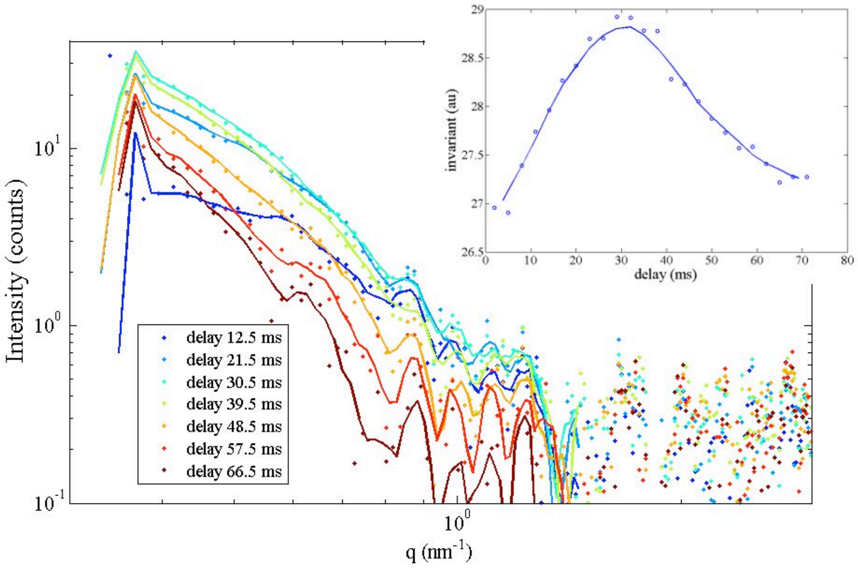

Figure 2. Time resolved SAXS as obtained after summation of 24k individual images for each delay. Background is obtained from scattering data corresponding to the first two delays. The inset shows time evolution of the scattering invariant.

From a Guinier analysis of the acquired SAXS data, the evolution with residence time of the radius of gyration can be obtained, showing a monotonic increase from ~2.5 nm on the head of the cluster beam pulse, to ~5.2 nm on the tail after ~50 ms. A detailed analysis of the state of aggregation (fractal dimension of the aggregates) as a function of residence time suffers from a lack of statistics due to limited accumulation time that was a consequence of the very long preparation time and low efficiency in data acquisition (limited by data transfer rate from the detector to mass storage in the HD drive). Despite these limits, the experiment proved the feasibility of cluster morphology determination via SAXS on a wiggler X-ray source.

References:

[1] P. Milani, P. Piseri, E. Barborini, A. Podestà and C. Lenardi;Cluster beam synthesis of nanostructured thin films ; J Vac Sci Tech A **19**, 2025 (2001)

[2] T. Mazza, M. Devetta, P. Milani, G. Bongiorno, M. Coreno, and P. Piseri; Accessing the fractal dimension of free clusters in supersonic beams; New J. Phys. **13**, 023009 (2011)

[3] E. Barborini, P. Piseri, and P. Milani; A pulsed microplasma source of high intensity supersonic carbon cluster beams; J Phys D **32**, L105 (1999)

[4] P. Piseri, H. Vahedi Tafreshi, and P. Milani; Manipulation of nanoparticles in supersonic beams for the production of nanostructured materials; Curr Op Solid State Mat Sci **8**,195(2004)

[5] G. Beaucage, HK. Kammler, R. Mueller, R. Strobel, N. Agashe, SE. Pratsinis, and T. Narayanan; Probing the dynamics of nanoparticle growth in a flame using synchrotron radiation; Nature Mater **3**, 370 (2004)

THE IMPACT OF THE AMORPHOUS PHASE ON THE DEFORMATION INDUCED FORMATION OF DISLOCATIONS IN IPP

F. Spieckermann[1], G. Polt[1], H. Wilhelm[1,2], E. Schafler[1], C.Fischer [2], M.J.Zehetbauer[1] and S. Bernstorff[3]

1.) Research Group Physics of Nanostructured Materials, Faculty of Physics, University of Vienna, 1090 Wien, Austria
2.) Laboratory of Polymer Engineering LKT-TGM, 1200, Wien, Austria
3.) Elettra - Sincrotrone, I-34149 Basovizza / Trieste, Italy

Earlier experiments [1,2,3,4] studying the dislocation dynamics in semi-crystalline polymers focused on the response of the crystalline phase with respect to plastic deformation. The response of the amorphous phase is expected to play an important role for the formation of dislocations during plastic deformation, as the stresses of this phase are transmitted via tie-molecules to the crystalline phase. Therefore the influence of this phase is investigated in the present experiment.

In-situ WAXS measurements during plastic deformation were successfully performed on alpha-phase isotactic polypropylene. By choosing samples with different molecular weights the degree of entanglement is varied. The glass transition temperature (Tg) of Polypropylene is at 0°C; hence the rigidity of the amorphous phase can be easily controlled by the deformation temperature. An Oxford Cryostream Cooler was used to cool the samples below Tg. A constant sample temperature of -5°C was reached. For reference the same experiment was performed at room temperature.

Figure 1 shows diffraction patterns of alpha-iPP deformed to different degrees of deformation, measured below Tg. Interestingly the deformation induced broadening of the line profiles is moderate. In Figure 2 the moderate increase of the dislocation density in such a sample is shown for deformation at room temperature and for deformation below the glass transition. A possible explanation of the less significant increase in the dislocation density of the sample deformed below Tg could be the reduced ability of the lamellae to rotate in the amorphous matrix. This would inhibit crystallographic slip as too few slip systems are available in slip condition. Such a behaviour should result in shear band formation easily observable by SEM investigations. Further experiments will be necessary to clarify this question.

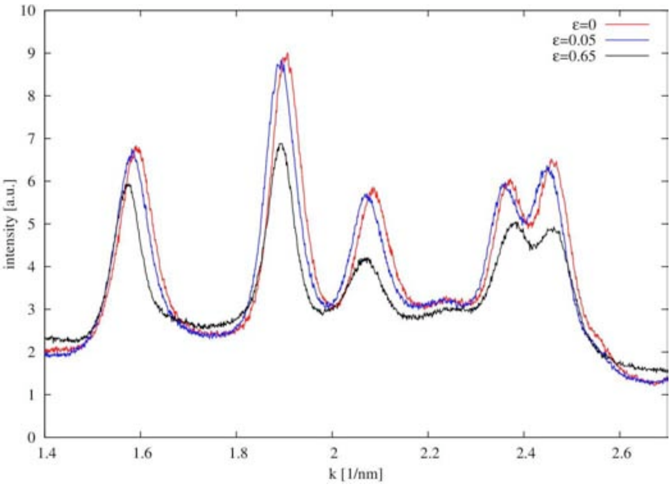

Figure 1. Diffraction patterns of alpha-iPP deformed to different degrees of deformation measured below the glass transition temperature.

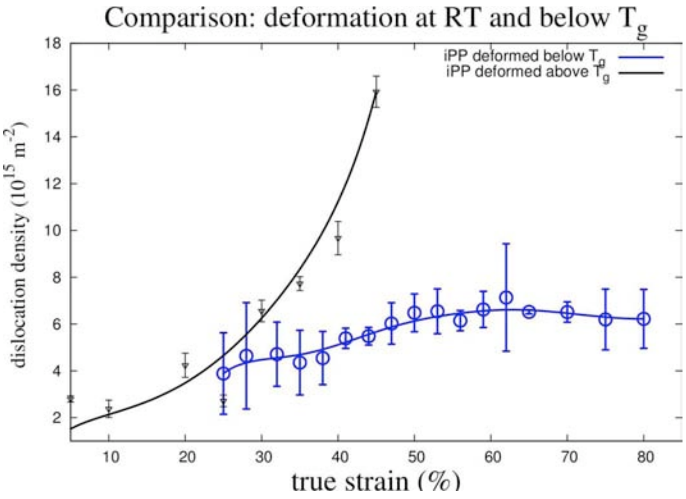

Figure 2. Comparison of the evolutions of the dislocation density in alpha polypropylene at room temperature and below the glass transition temperature.

Acknowledgements:

Thanks are given to the Austrian Science Fund (FWF) for support in the frame of project 22913-N20.

References:

[1] F. Spieckermann, G. Polt, H. Wilhelm, M. Kerber, E. Schafler, and M.J. Zehetbauer; The role of dislocations for the plastic deformation of semicrystalline polymers as investigated by multireflection X-ray line profile analysis; J. Appl. Polym. Sci., 125, 4150-4154 (2012)

[2] H. Wilhelm, A. Paris, E. Schafler, S. Bernstorff, J. Bonarski, T. Ungar, and M.J. Zehetbauer; Evidence of dislocations in melt-crystallised and plastically deformed polypropylene; Mater. Sci. Eng., A, 387-389, 1018-1022, (2004)

[3] F. Spieckermann, H. Wilhelm, E. Schafler, M. Kerber, S. Bernstorff, S. and M.J. Zehetbauer; Plasticity and X-ray Line Profile Analysis of the semicrystalline polymer poly(3-hydroxybutyrate); Journal of Physics: Conference Series, 240, 012146, (2010)

[4] G. Polt, F. Spieckermann, H. Wilhelm, M. B. Kerber, E. Schafler, S. Bernstorff, M. Zehetbauer, The Role of Dislocations in γ-iPP under Plastic Deformation investigated by X-ray Line Profile Analysis, Mech. Mater., http://dx.doi.org/10.1016/j.mechmat.2013.05.010, in press

[5] T. Ungár, and A. Borbély; The effect of dislocation contrast on x-ray line broadening: A new approach to line profile analysis; Appl. Phys. Lett., AIP, 69, 3173-3175, (1996)

KINETIC EFFECTS ON THE PROPERTIES OF PARTICLES FORMED BY NANOPRECIPITATION

M. Steinhart[1,2], A. Jager[1], E. Jager[1], P. Štěpánek[1] and H. Amenitsch[3]

1.) Institute of Macromolecular Chemistry, Heyrovský sqr. 2, 162 06 Prague, Czech Republic
2.) Institute of Applied Physics and Mathematics, FCHT, Univ. of Pardubice, Studentská 84, 532 10 Pardubice
3.) Institute of Inorganic Chemistry, Graz University of Technology, Stremayrgasse 9/IV, 8010 Graz, Austria

Introduction

With the growth in the last decades in the research focused on nanoparticles for several technological applications many efforts were done trying to understand the process of nanoparticle formation to achieve better control and stability. Currently we are working on a new class of aggregates nanoparticles (NPs) intended for use in biomedical and optical applications based on polythiophene cationic polyelectrolyte with ionic-liquid like side groups: poly{3-[6-(1-methylimidazolium-3-yl)hexyl]thiophene-2,5-diyl bromide} (PMHT-Br) prepared by nanoprecipitation in aqueous media containing silver nanoparticles with sizes around 1.5 nm (Ag-NPs) [1]. Nanoprecipitation consists in mixing DMSO solution containing the PMHT-Br polymer with an excess of water containing Ag-NPs under specific physic-chemical conditions during which polymer and Ag-NPs aggregates' and NPs are formed. Dynamic light scattering shows instantaneously a multimodal size distribution of the PMHT-Br-Ag-NPs aggregates with populations about 5, 30, and 100 nm. In order to understand the kinetics of PMHT-Br-Ag-NPs aggregates under formation the kinetics of the early stages of the NPs aggregation formation was probed using stopped-flow SAXS. This also involves studying the conditions that influence the nanoprecipitation process: polymer concentration, water/DMSO ratio and temperature.

Experimental

A small-angle scattering experiment was performed using the SAXS beam line equipped with the Bio-Logic SFM-400 stopped-flow apparatus and the Pilatus100K detector. With the wavelength 1.5 A the detector position was set to cover a q-range 0.05-5 nm^{-1} necessary to investigate the expected range of NPs sizes. Samples were prepared by using two syringes of the thermostated mixing instrument. The first syringe was filled with the solution of PMHT-Br in DMSO and the second one with Ag-NPs in water. The samples were mixed in several ratios of these two components at two temperatures 25°C and 40°C. The counting time in the first 499 frames was 19 ms, in the next 500 frames 994 ms and then 10 s. Data transfer time after each frame was 6 ms.

Results and Discussion

At first we have tried to find a way how to reveal meaningful changes in time possibly from the raw data. The idea was that this method could be used even during the measuring sessions which could then be rescheduled according to the immediate results. For this purpose the calculation of correlation length using the ratio of two integral parameters is sometimes done. In our case, however, we found more sensitive the Guinier analysis of the raw data with the empty cuvette subtracted. The advantage of this approach is its generality, mainly independence on the objects involved. Illustration of such analysis is depicted in Figure 1 where the time development of Rg for three runs which differ in concentration of PMHT-Br polymer versus Ag-NPs is being compared. The process for high concentration clearly differs from the other two. The fastest growing are nanoparticles with medium concentration of polymer and the growth for low concentration is slower. Since the endings of the relevant lin-log plots are roughly linear it is possible to consider the growth as logarithmic and its parameters can be fitted as it is done on the right side of Figure 1. Here the data are deliberately unsmoothed to show that reliability of the information from the first quickly taken frames is low. More information could be revealed best by fitting an appropriate structure model in which the solvent scattering is also taken care of.

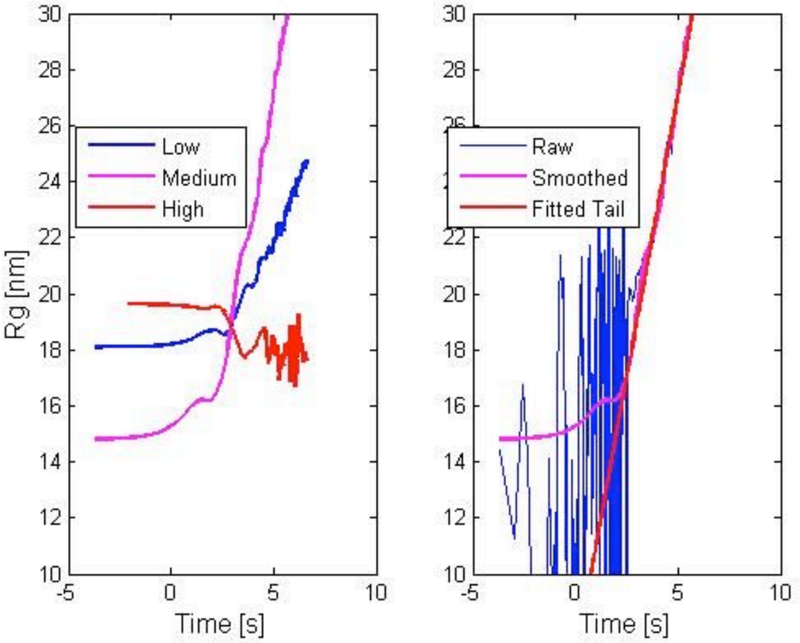

Figure 1. Rg as a function of time from Guinier analysis. Left: Smoothed data for three concentrations. Right: Fit of logarithmic growth for the medium concentration on the unsmoothed data. Note that the scale of the horizontal time axis is logarithmic.

An example of such a process is illustrated in Figure 2 where static measurements of the components before mixing and two representative frames from the kinetic of mixing of Ag-NPs water solution (2.3 x 10^{-7} M) with PMHT-Br polymer in DMSO (2.5 x 10^{-6} M) in a ratio 1/10 *v/v* (DMSO/water) at 25°C are shown. The frames compare scattering and its fit with a model close to the beginning of the mixing (frame 100 ~ 2.5s) and close to the end of the experiment (frame 1010 ~ 622 s). The pure Ag-NPs in water can be fitted well using widely distributed spheres with mean radius Ra = 2.6 nm. In all other measurements the contribution of polymer scattering is important. We have found a model applicable for all this data consisting of Schulz-Zimm distributed spheres + mass fractal + background. The polymer part is complicated so it is fitted at least technically i.e. without gaining meaningful structural parameters. Solvent scattering is approximated by a constant background. This might be acceptable for water solutions but is surely more problematic for DMSO + H2O mixtures especially shortly after mixing. Fitting of the first frames is very unstable and the model is not appropriate since it is ill-conditioned (it uses more parameters than is the real information content). But from around 11 s after the mixing the fitting becomes stable and the parameters meaningful. It is possible to see a similar behavior as could be estimated from the Guinier analysis but now supported by a structure model and also giving more parameters. In Figure 3 the development in time of the mean size of spherical nanoparticles and Rg of the mass fractal part are shown.

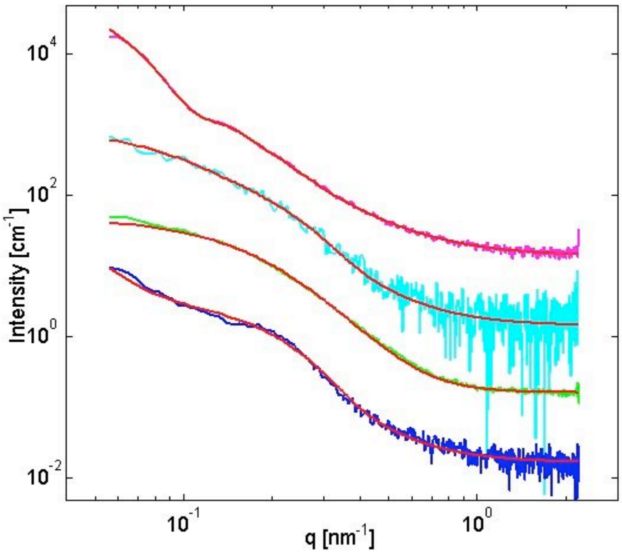

Figure 2. Scattering curves with their fit on the absolute scale. From below: pure polymer in DMSO, Ag nanoparticles in H2O (x10), frame at 2.5 s (x100), frame at 622 s after the mixing (x1000). Curves were successively multiplied by ten to be easily distinguished]

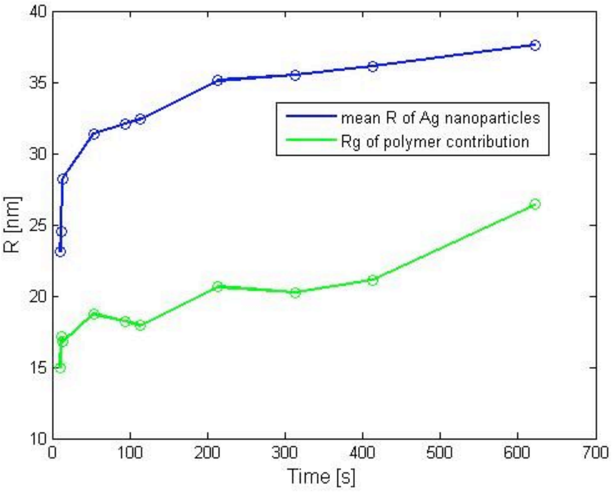

Figure 3. Time development of model parameters of Ag-NPs-PMHT-Br aggregates and polymer contribution after mixing [5].

Although the Rg values of the latest frames from the kinetics measurement are in agreement with the Rh values found in dynamic light scattering, there are still several hundreds of frames right after the mixing (taken at 19/ 25 ms) from which our information is poor due to their low quality. Since they contain the transition region further thorough study using better methods will have to be done. On the other hand even the relatively simple approach described above gives an important result revealing the details of the nanoparticles growth at various experimental conditions.

References:

[1] Kazim S., Pfleger J., Procházka M., Bondarev D., Vohlídal J., *J Coll. Int. Sci* 2011, 354, 611–619

STRUCTURE OF Fe_2O_3/Ti_2 NANOCRYSTALS IN SILICA MATRIX

V. Valeš[1], J. Endres[1], V. Holý[1], M. Buljan[2], V. Janicki[2], and S. Bernstorff[3]

1.) Zernik Charles University in Prague, Ke Karlovu 5, 12116 Prague, Czech Republic
2.) Rudjer Boskovic Institute, Bijenička 54, 10000 Zagreb, Croatia
3.) Elettra - Sincrotrone Trieste, Strada Statale 14, km 163.5, 34149 Basovizza (TS), Italy

Titania (TiO_2)-based systems have been very intensively studied in the last decades because of their photocatalytic activity, which found broad commercial applications [1-3]. Functionalized titania composites, especially Fe_2O_3/TiO_2 systems, attracted a lot of attention recently (see [4-8], among others), since they make it possible to improve the photocatalytic performance of titania. We have studied (Fe_2O_3+SiO_2)/ SiO_2 and (Fe_2O_3+SiO_2) / (TiO_2+SiO_2) /SiO_2 periodic multilayers with the same SiO_2-spacer thicknesses of 10 nm, and variable thicknesses d of the (Fe_2O_3+SiO_2) / (TiO_2+SiO_2) layers. Both types of samples were grown by a sequential deposition, in which 10-period multilayers were deposited by electron beam evaporation onto rotating Si substrates at room temperature. Growth details have been described elsewhere [9]. The samples have been subsequently annealed for one hour at various temperatures in air or forming gas (FG – Ar + 4% H_2). The structure of the multilayers has been studied by x-ray diffraction (XRD) using a standard laboratory diffractometer (CuKα radiation, 1.6 kW X-ray tube) and by grazing-incidence small-angle X-ray scattering (GISAXS) at the SAXS beamline at ELETTRA (Trieste), using the photon energy of 8 keV and a large image plate as a detector.

The XRD data on samples without titania exhibit diffraction maxima neither before, nor after post-growth annealing, i.e., the Fe_2O_3 component did not crystallize during the annealing even at 900 °C. From the data it follows that TiO_2 nanoparticles grow during the annealing, from the positions of their diffraction peaks we identified the tetragonal rutile phase (see Fig. 1). More interestingly, in (Fe_2O_3+SiO_2) / (TiO_2+SiO_2) / SiO_2 multilayers after annealing at 900°C in air we detected also Fe_2O_3 nanoparticles, however their diffraction maxima are rather weak, which indicates that the density of these particles is very small. The positions of the Fe_2O_3 maxima roughly correspond both to hexagonal hematite α-Fe_2O_3 and tetragonal ε-Fe_2O_3 phases.

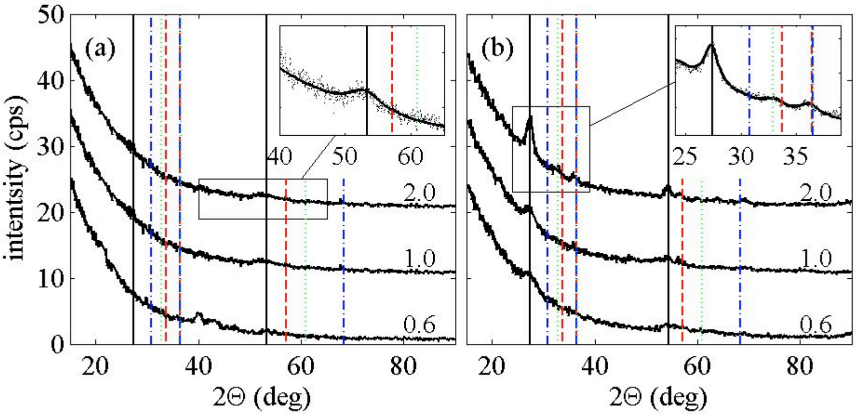

Figure 1. X-ray diffraction curves of mulitlayers annealed at 700 °C (a) and at 900 °C (b). The numbers denote the nominal thicknesses d of the (Fe_2O_3+SiO_2)/(TiO_2+SiO_2) layers. The insets display the details of the diffraction peaks along with their fits to theoretical curves (lines). The vertical lines indicate the theoretical positions of the diffraction peaks for various phases: black full lines – rutile, red dashed lines – hematite (α-Fe_2O_3), blue dash-dotted lines – maghemite (γ-Fe_2O_3), and green dotted lines – ε-Fe_2O_3.

Examples of GISAXS data are plotted in Fig. 2 together with the simulation results. The GISAXS simulation program and the structure model of disordered particle arrays were described in detail elsewhere [10]. We assume that the particles are ellipsoidal and they create a highly disordered three-dimensional array. The experimental data of the (Fe_2O_3+SiO_2)/SiO_2 multilayers show no XRD peaks and no side maxima in GISAXS intensity maps. Therefore, the multilayers not containing titania remain amorphous and do not form any ordered structure of amorphous or crystalline particles during post-growth annealing at temperatures up to 900 °C. On the other hand, the multilayers (Fe_2O_3+SiO_2)/(TiO_2+SiO_2)/ SiO_2 exhibit both XRD peaks and GISAXS side maxima after annealing, thus they contain ordered arrays of *crystalline* particles. In these samples, both rutile TiO_2 and α-Fe_2O_3 or ε-Fe_2O_3 phases are present, however, the Fe-containing phases with much smaller occurrence. Therefore, the presence of the TiO_2 phase facilitates the crystallization of Fe_2O_3 during post-growth annealing.

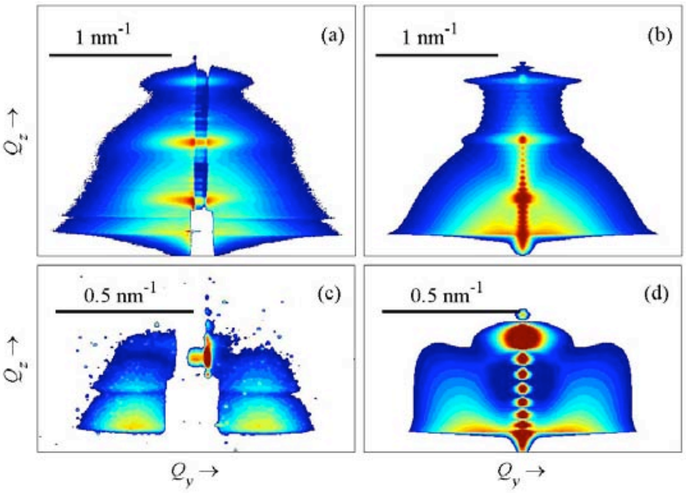

Figure 2. Measured (a,c) and simulated (b,d) GISAXS intensity maps of samples with *d* = 2.0 nm after annealing at 700°C (a,b) and 900°C F (c,d) in air. The data in panels (a) and (c) were recorded by an image plate and a ccd detector respectively, the step of the intensity contours is $10^{0.3}$ and $10^{0.1}$ for panels (a,b) and (c,d).

In conclusion, we have investigated the growth of crystalline nanoparticles during post-growth annealing of (TiO_2, Fe_2O_3, SiO_2) multilayers by x-ray diffraction and grazing-incidence small angle x-ray scattering. We observed the growth of rutile TiO_2 and Fe_2O_3 nanocrystals and determined the dependence of their size and ordering on the annealing conditions. From our data it follows that the crystallization of hematite is facilitated by the presence of TiO_2.

References:

[1] A. Fujishima and K. Honda, Nature **37,** 238 (1972)
[2] A. Fujishima, K. Hashimoto, and T. Wanatabe, *TiO_2 Photocatalysis, Fundamentals and Applications*, (BKC, Inc., Tokyo, 1999)
[3] M.R. Hoffman, S.T. Martin, and W. Choi, Chem. Rev. **95,** 69 (1995)
[4] H. Cui, W. Ren, W. Wang, J. Sol-Gel Sci. Technol. **58**, 476 (2011)
[5] R. C. Suciu, M. C. Rosu, T. D. Silipas, E. Indrea, V. Popescu, and G. L. Popescu, J. Environ. Eng. Landsc. Manag. **10**, 187 (2011)
[6] M. T. Esfandarani, L. J. Minggu, W. R. W. Daud, and M. B. Kassim, J. New Mater. Electrochem. Syst., **13**, 333 (2010)
[7] V. Tyrpekl, J. Poltierová Vejpravová, A.G. Roca, N. Murafa, L. Szatmary, and D. Nižňanský, Appl. Surf. Sci. **257**, 4844 (2011)
[8] V. Valeš, J. Poltierová Vejpravová, V. Holý, V. Tyrpekl, P. Brázda, and S. Doyle, phys. stat. solidi C **7**, 1399 (2010)
[9] V. Valeš, V. Holý, M. Buljan, V. Janicki, S. Bernstorff, Thin Solid Films **520**, 4800 (2012)
[10] M. Buljan, U. V. Desnica, M. Ivanda, N. Radić, P. Dubček, G. Dražić, K. Salamon, S. Bernstorff, and V. Holý, Phys. Rev. B **79**, 035310 (2009)

NANO-MORPHOLOGICAL CHARACTERIZATION OF THE CATALYST DEGRADATION IN HIGH TEMPERATURE PEM FUEL CELLS

F. Valle[1], B. Marmiroli[2], H. Amenitsch[2], R. Taccani[1]

1.) Engineering and Architecture department, University of Trieste, via A. Valerio 10, Trieste 34127, Italy
2.) Institute of Inorganic Chemistry, Graz University of Technology, Stremayrgasse 9/IV, Graz 8042, Austria

High temperature PEM fuel cells have several advantages over lower temperature ones, such as higher tolerance of CO in fuels, enhanced reaction kinetics and absence of a humidification system. The higher operative temperature, however, introduces some drawbacks mainly related to the Membrane Electrode Assembly (MEA) degradation. The catalyst degradation is one of the main issues. The catalyst, in PEM fuel cells, is in the form of nanoparticles, in order to increase the active surface area to weight ratio. The degradation of the catalyst happens during operation, both through the increase in size due to aggregation and through isolation and dissolution of the particles. The common consequence of these phenomena is the reduction of the Electrochemical Active Surface Area (EASA) of the catalyst that leads to a lower performance of the fuel cell. The understanding of the physical process behind the aggregation of the catalyst particles is a primary step towards the improvement of the PEM fuel cell efficiency and durability. The aim of this research is to increase the knowledge related to catalyst degradation and to propose fuel cell operation modes that can decrease fuel cell loss in performance. For this purpose, the samples have been investigated with synchrotron Small-Angle X-ray Scattering (SAXS).

The sample employed for the experiments is the Celtec-P 1000 by BASF [1], a commercial MEA for HT-PEM fuel cells. This MEA is composed by three layers in a sandwich-like structure: the polymeric memebrane (MEA) in the middle, the catalyst layer and the Gas Diffusion Layer (GDL) as shown in figure 1 top right. The polymeric membrane is made by phosphoric acid-doped polybenzimidazole (PA-PBI), the Gas Diffusion Layers (GDLs) by carbon cloth and the catalyst layer by a mix of Pt nanoparticles (the catalyst) and carbon powder (a support). The SAXS experiment has been carried out in transmission with a 1x0.5mm beam, using a 2D detector (Pilatus 100K, Dectris Ltd. Swiss). The collected images have been analyzed with the software FIT2D [2]. The q-range varies from 0.1 to 4 nm^{-1}.

The model employed to describe the catalytic nanoparticles system within the catalyst layer considers a polydispersed system of spherical adhesive particles with a narrow and deep attractive inter-particle potential and a Schulz distribution of sizes, as described by Pontoni et al. [3]. Additionally, the contribution from the carbon in the GDL and particles in the catalyst layer has been modeled with a generalized Porod law [4].

A first experiment had the purpose to obtain the scattering contribution of the different layers of the MEA in order to design an effective procedure for the catalyst investigation. A PEM sample has been obtained from the border and the GDL has been removed by peeling from the rest of the MEA. The scattering intensity curves of these specimens are plotted in Figure 1. The scattering intensity of the PEM (1) is significantly lower than the others. This means that this layer has a limited contribution to the entire MEA scattering. Comparing the curve of the entire MEA (4) with the one of the GDL (2), a different behavior is visible. This confirms that the Pt particles are concentrated into the catalyst layer. Thus, the GDL contribution does not affect the catalyst particles information as well as the PEM layer. For these reasons, the scattering intensity curve of the entire MEA can be employed to analyze the catalyst particles and a specific preparation of the sample can be avoided. In a second experiment three whole MEAs (MEA ref, MEA 1 and MEA 2) have been observed. MEA ref is a virgin sample, MEA 1 operated for few hours in a fuel cell stack and MEA 2 has been subjected to intense start-stop operation in a single cell. A quantitative result has been obtained by the fitting of the experimental scattering curves with a polydispersed system of spherical adhesive particles (Table 1). The results of the fitting confirm the growth of the catalytic particles. The mean size of the virgin MEA ref is 5 nm and it is assumed to be the initial size of all the three samples before operation. MEA 1 operated for few hours, but a little agglomeration of the particles is however present: the mean size is 5.5 nm, with a growth of about 9%. MEA 2 is the most used one and the particles agglomeration is the highest, as expected: the mean size is more than 8 nm that it is an increase of 62.8%. Given the root mean square of the particles radius σ_R and the mean radius R for each sample, it has been possible to obtain the Schulz distribution of R, as shown on the inset of Figure *2*. MEA ref and MEA 1 have a low and similar σ_R, about the half of that of MEA 2. This leads to a very sharp distribution and thus a low polydispersity of the Pt particles. The distribution of MEA 2 is significantly flatter, with a high polydispersity. The values of the volume fraction remark the previous considerations. Most of the particles are isolated in the virgin MEA ref, while in MEA 2 the aggregation is significantly higher. In MEA ref, indeed, the inter-particle potential is negative and thus the aggregation is absent. The results confirmed thus that MEA 2 is the most degraded sample and that catalyst particles agglomeration is strongly dependent on operation mode.

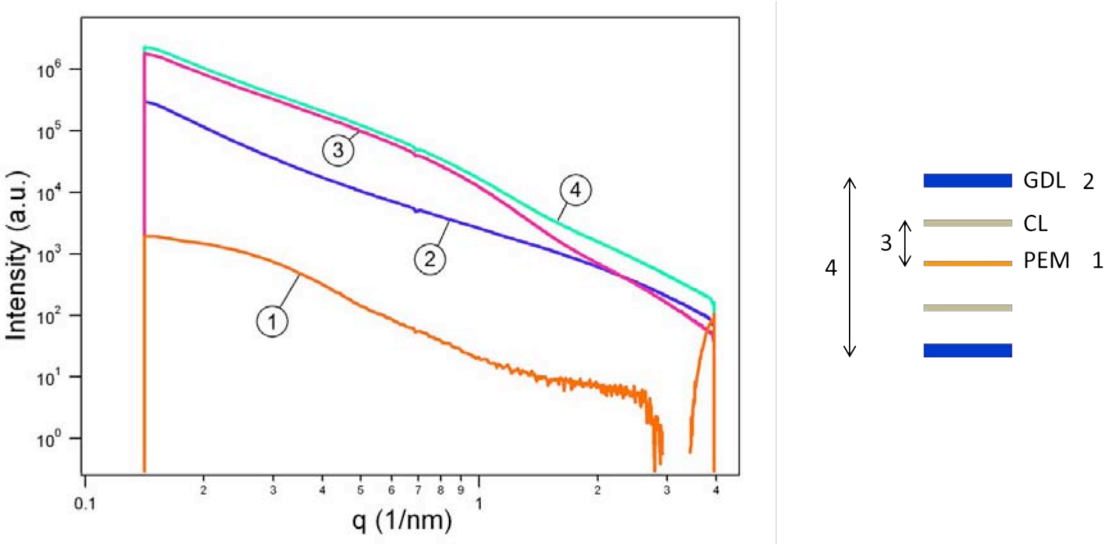

Figure 1. Scheme of the composition of the MEA (top right). Scattering curves of a MEA: PEM (1), GDL (2), PEM sandwiched with the catalyst layers (3), entire MEA (4). PEM (1) contribution is significantly lower than the others, the GDL (2) behavior is different from that of curve (3) and (4) due to the absence of catalyst particles.

Table 1. Results of the fitting. R is the mean radius of the particles, σ_R is the root mean square deviation of the radius, V_f is the volume fraction of the particles surrounding every single particle, λ is the width and ε the depth of the square-well of the inter-particle potential

Sample	**R [nm]**	**σ_R [nm]**	**V_f [-]**	**λ [-]**	**ε [-]**
MEA-ref	2.48	0.48	0.03	2.8	-0.1
MEA-1	2.72	0.42	0.07	3.1	0.1
MEA-2	4.07	0.94	0.10	1.4	0.2

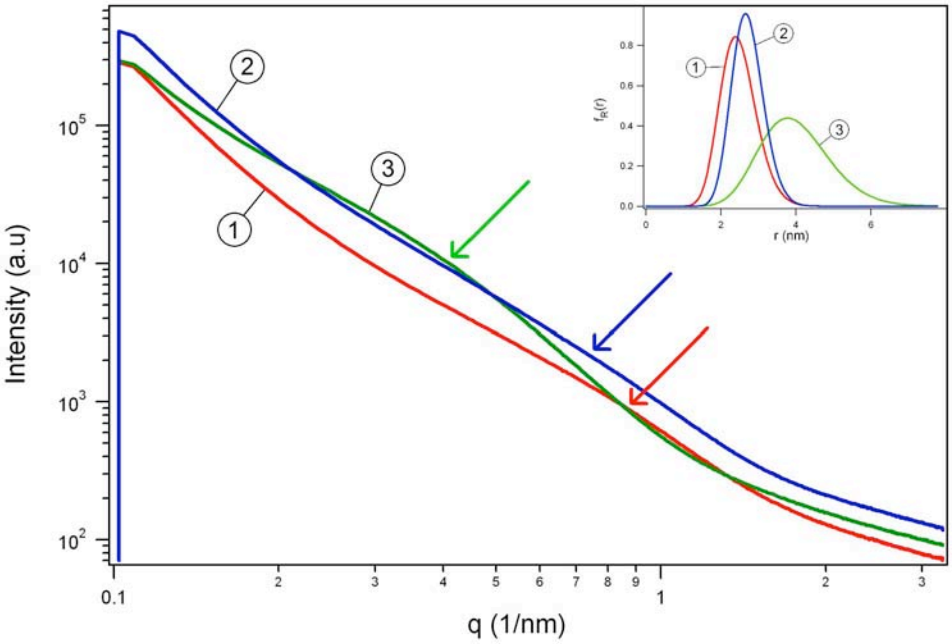

Figure 2. SAXS scattering curves of MEA-ref (1), MEA-1 (2) and MEA-2 (3). The arrows indicate the shoulder on the curves that indicates the presence of the catalyst particles. The curves on the inset are the Schulz size distribution for each sample showing the higher polydispersity of MEA-2 (3) than that of MEA-ref (1) and MEA-1 (2)

References:

[1] BASF Fuel Cell, Celtec-P 1000 Membrane Electrode Assembly, Technical Information Brochure, 1997
[2] A. P. Hammersley, ERSP International Report, ESRF98HA01T, FIT2D V9, 129 Reference Manual V3.1, 1998
[3] D. Pontoni, S. Finet, T. Narayanan and A. R. Rennie, Interactions and kinetic arrest in an adhesive hard sphere colloidal system, The Journal of Chemical Physics, vol. 119 (12), pp. 6157, 2003
[4] F. Valle, SAXS characterization of a HT-PEMFC Membrane Electrolyte Assembly, M.Sc. thesis, University of Trieste, 2012

STRUCTURAL AND ELECTRICAL CHARACTERIZATION OF NANOSTRUCTURES BASED ON SiGe NANOCRYSTALS EMBEDDED IN Al_2O_3 MATRIX

E. M. F. Vieira[1], J. Martín-Sánchez[2], M. Buljan[3], M. A. Roldan[4], M. Varela[5], S. J. Pennycook[5], S. I. Molina[6], S. Bernstorff[7], A. G. Rolo[1], A. Chahboun[1,8] and M. J. M. Gomes[1]

1.) Centro de Física, Universidade do Minho, 4710-057 Braga, Portugal
2.) Laser Processing Group, Instituto de Óptica, CSIC, C/ Serrano 121, 28006 Madrid, Spain
3.) Ruđjer Bošković Institute, Bijenička cesta 54, 10000 Zagreb, Croatia
4.) Universidad Complutense de Madrid, Madrid 28040, Spain
5.) Materials Science and Technology Division, Oak Ridge National Laboratory, Oak Ridge, Tennessee 37831, USA
6.) Departamento de Ciencia de los Materiales e Ing. Metalúrgica y Q. I., Universidad de Cádiz, Cádiz, Spain
7.) Elettra - Sincrotrone Trieste, 34149 Basovizza (TS), Italy
8.) FST Tanger, Physics Department, BP 416, Tanger, Morocco

The fabrication of nanostructures with dimensions below 100 nm and organized within large macroscopic areas is a prerequisite for many applications in the field of nanotechnology. In recent years, growing attention has been paid to semiconductor nanocrystals (NCs)/dielectric multi-layered (ML) systems because of their interesting size-tunable properties, which makes them suitable for applications in electronics, optoelectronics and solar cells [1-2]. For an optimal performance, it is highly desirable to develop a fabrication method that allows one to obtain stable layers with low interfacial roughness, low inter-diffusion between layers and a high spatial density of NCs; homogeneous sizes in a very thin and well defined two-dimensional layer, where the distance between adjacent NC layers can be maintained constant over large areas are also required. In fact, we have recently reported a stable multi-layer structure with the formation of well-organized SiGe NCs confined between 5nm thick SiO_2 layers [3]. Here, we show an overall multilayer stability with well-organized SiGe NCs in 4 nm thick layers after performing a conventional annealing at 800 ºC for 10 min and a rapid annealing (RTA) at 900 ºC for 30 s. Also, we show that carrier transport in a typical $Si_{1-x}Ge_x$+Al_2O_3/Al_2O_3 MOS nanostructure is dominated by the Fowler-Nordheim tunneling mechanism.

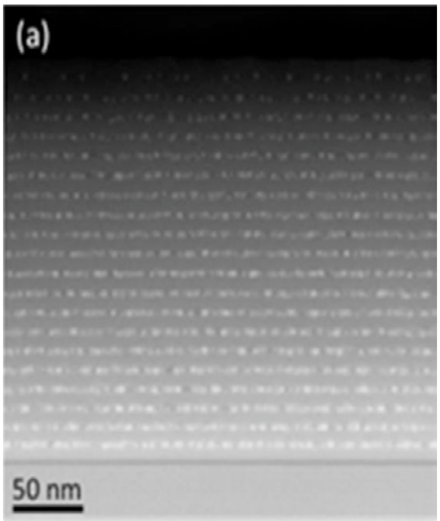

Figure 1. Low magnification cross-sectional HAADF-STEM images of the whole ML structure for an annealed sample produced at 60 W RF power [4].

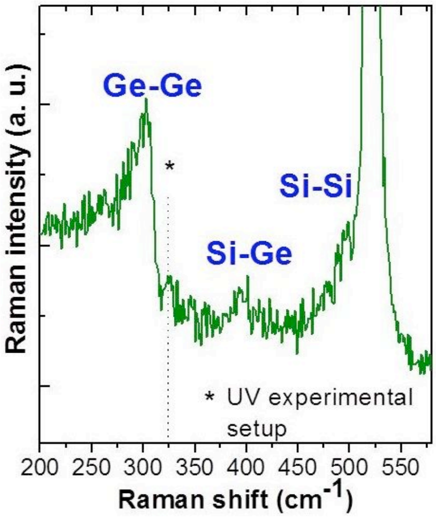

Figure 2. Raman spectra of an annealed sample produced at 60W RF power [4]. The peak at 325 cm^{-1} (*) comes from the UV experimental setup.

Cross-sectional HAADF-STEM images of the whole SiGe+Al_2O_3/Al_2O_3 ML structure produced at 60 W RF sputtering-power show after annealing (Figure 1) a well-organized ML structure with well-defined interfaces, with the formation of spherical nanoparticles (3 to 5 nm of diameter). The formation of SiGe nanocrystals is confirmed by Raman spectroscopy (Figure 2). In the GISAXS map of the as-grown film (Figure 3a), the Bragg sheets are resolved and they correspond to a multilayer structure with good periodicity ($\alpha > \alpha_{cr}$). On the other hand, the GISAXS map obtained for the annealed film indicates nicely ordered surface morphology features ($\alpha \sim \alpha_{cr}$) (Figure 3 b).

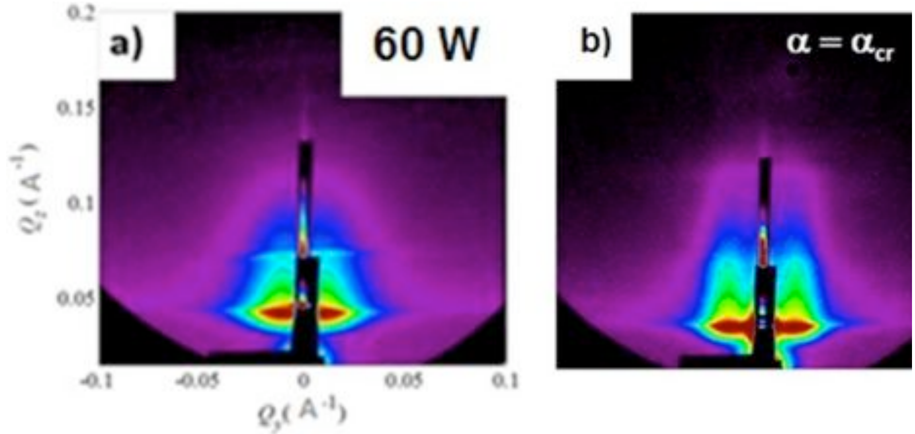

Figure 3. GISAXS intensity distributions of the as-grown (a) and annealed (c) sample produced at 60W RF power [4].

References:

[1] S. Gardelis, P. Manousiadis, and A. Nassiopoulou; Lateral electrical transport, optical properties and photocurrent measurements in two-dimensional arrays of silicon nanocrystals embedded in SiO_2; Nanoscale Res. Lett. 6, 227(1-6) (2011).

[2] S. K. Kim, C. H. Cho, B. H. Kim, S. J. Park, and J. W. Lee; Electrical and optical characteristics of silicon nanocrystal solar cells; Appl. Phys. Lett. **95**, 143120(1-3) (2009).

[3] E.M.F. Vieira, J. Martín-Sánchez, A.G. Rolo, A. Parisini, M. Buljan, I. Capan, E. Alves, N.P. Barradas, O. Conde , S. Bernstorff, A. Chahboun, S. Levichev, and M.J.M. Gomes; Structural and electrical studies of ultrathin layers with Si0.7Ge0.3 nanocrystals confined in a SiGe/SiO2 superlattice; J. Appl. Phys. **111**, 104323(1-9) (2012).

[4] E.M.F. Vieira, J. Martín-Sánchez, M.A. Roldan, M. Varela, M. Buljan, S. Bernstorff, N.P. Barradas, N. Franco, M.R. Correia, A.G. Rolo, S.J. Pennycook, S.I. Molina, E. Alves, A. Chahboun and M.J.M. Gomes; Influence of RF-sputtering power on formation of vertically stacked $Si_{1-x}Ge_x$ nanocrystals between ultra-thin amorphous Al_2O_3 layers: structural and photoluminescence properties; Journal of Physics D: Applied Physics, Vol. 46 - 38, pp. 385301-1-385301-10 (2013)

Life Sciences

STRUCTURAL INSIGHTS INTO THE HUMAN GINS COMPLEX

M. De March[1], M. Carroni[2], I. Krastanova[1], H. Amenitsch[3], A. Patwardhan[2] and S. Onesti[1]

1.) Structural Biology Laboratory, Elettra - Sincrotrone Trieste S.C.p.A. 34149 Trieste, Italy
2.) Imperial College London, SW7 2AZ, London, UK
3.) Institute of Inorganic Chemistry, Graz University of Technology, A-8010 Graz, Austria

Background

Chromosomal DNA replication in *Eucharya* is a process that requires a large number of protein factors whose activity is tightly regulated to ensure that each genomic region is replicated only once per cell cycle. In this process the DNA is unwound by specific replicative machinery, known as the CMG complex [1], which is assembled to form two replication forks moving in opposite directions. The well-known members of the CMG machinery are the MCM 2-7 helicases [2]. Whereas a low resolution structure by SAXS has been recently published on Cdc45 [3], structural information on the GINS complex has been available for a few years, but there is a serious discrepancy between the results from protein crystallography (PX, [4]) and electron microscopy (EM, [5]): the crystal structure showed the 4 subunits (Psf1, Psf2, Psf3, Sld5) making up the GINS complex forming a compact tetramer, while the EM data has been interpreted as a partially open ring. The authors suggest that in solution the four subunits open up to form a C-shape, but gets compacted in the crystal [5]. To resolve the discrepancy we carried out new structural studies using new EM data complemented by SAXS studies performed at the AustroSAXS beamline at Elettra.

Results and discussion

The new EM study carried out on the negatively stained human GINS complex revealed the presence of a twofold axis, leading to a 3D reconstruction that resembles the one published [5] in terms of overall size, but is distinctively different. The dimeric reconstruction can be fitted by a dimer of tetramers, present in the crystal structure (PDB code: 2EHO, [4]). Two small protrusions can be assigned to the B domain of Psf1, which is not visible in the crystal structure presumably due to flexibility. Indeed, by size-exclusion chromatography coupled with multi-angle laser light scattering (SEC-MALL) we were able to detect the presence of two oligomeric state of the GINS complex: the tetramer (95kDa) and a double-tetramer (191kDa) with a relative concentrations of 10:1, respectively. Samples from the single tetramer peak did not show visible, distinct particles when visualised by EM (presumably due to the small size), while single globular particles of roughly 100Å were visible from samples corresponding to the dimeric peak.

To confirm this novel interpretation, SAXS data were collected for both the wild-type human GINS complex and a deletion mutant lacking the Psf1 B-domain. The X-ray scattering curves were collected at $\lambda=1.54$ Å with a sample to detector distance of about 1.7 m. After calibration, background subtraction, average, normalization and merge processes, the structural parameters where calculated from the experimental curve (Table 1). The ATSAS softwares [6] were further used to get a second estimation of the structural parameters, to derive the P*(r)* function and to get the best ab-initio model for both the wt-GINS and ΔB-hGINS. The SAXS model of wt-hGINS appears as a compact parallelepiped with a lateral extension. The main core is in good agreement with the crystallographic structure, and the lateral extension can be assigned to the B-domain as it is in proximity of the last Psf1 residues visible in the crystal structure (Figure 1a). The simulated curve [6] of the wt-hGINS atomic coordinates together with the Psf1 B-domain fits the experimental data better than the crystal structure alone [4]. The SAXS model for ΔB-hGINS showed a more compact structure and lacked the extension. SAXS data therefore confirm that the GINS complex is a compact tetramer in solution as well as in the crystals (Figure 1b) and do not provide evidence for the proposed conformational change [5]. Instead, the discrepancy between the crystallographic and EM data is due to the fact that only the small amount of dimeric complex present in solution has a signal-to-noise ration sufficient to show distinct particles, and therefore the EM reconstruction corresponds to a dimeric structure. Moreover, both SAXS and EM data provide some indication of the location of the Psf1 B domain, a flexible region that is important for the function of the complex within the replication machinery.

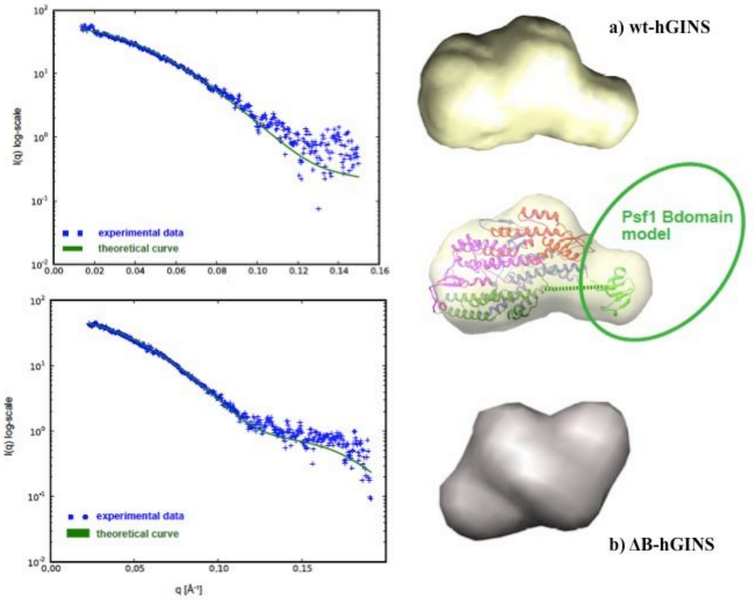

Figure 1. SAXS data from hGINS. **a)** The wt-hGINS experimental profile (blue crosses) with the theoretical one (green line) simulated from the model (yellow). The X-ray structure [4] is fitted into the core of the envelope and the side protrusion is assigned to the B-domain of the Psf-1 subunit. **b)** The ΔB-hGINS experimental profile (blue crosses) with the theoretical (green line) simulated from the model (gray).

Table 1. The SAXS structural parameters calculated for wt-hGINS and ΔB-hGINS.

Sample	q_{range} (nm)	I (0) 1/cm	R_g (Å)	D_{max} (Å)	$V_{envelope}$ ($Å^3$)	MW (KDa)
wt-hGINS	0.0137 – 0.2187	0.067	33.69 ± 0.41	110	193700	124 ± 23.1
ΔB-hGINS	0.0232 – 0.2035	0.026	30.02 ± 0.63	100	105200	84 ± 12.6

References:

[1] S. Onesti and S.A. MacNeill; Structure and evolutionary origins of the CMG complex; Chromosoma **122**, 47-53 (2013)

[2] A. Costa and S. Onesti; Structural biology of MCM helicases; Crit. Rev. Biochem. Mol. Biol. **44**, 326-342 (2009)

[3] I. Krastanova, V. Sannino, H. Amenitsch, O. Gileadi, F.M. Pisani and S. Onesti; Structural and functional insights into the DNA replication factor Cdc45 reveal an evolutionary relationship to the DHH family of phosphoesterases; J. Biol. Chem. **287**, 4121–4128 (2012)

[4] J.M. Choi, H.S. Lim, J.J. Kim, O.K. Song and Y. Cho; Crystal structure of the human GINS complex; Genes Dev. **21**, 1316-1321 (2007)

[5] J. Boskovic, J. Coloma, T. Aparicio, M. Zhou, C.V. Robinson, J. Mendez, G. Montoya; Molecular architecture of the human GINS complex; EMBO Rep **8**: 678-684 (2007)

[6] M.V. Petoukhov, D. Franke, A.V. Shkumatov, G. Tria, A.G. Kikhney, M. Gajda, C. Gorba, H.D.T. Mertens, P.V. Konarev and D.I. Svergun; New developments in the ATSAS program package for small-angle scattering data analysis; J. Appl. Cryst. **45**, 342–350 (2012)

EFFECTS OF CARBON BASED NANOPARTICLES ON MODEL LIPID MEMBRANES

B. Drasler[1], D. Drobne[1], V. Kononenko[1], S. Boljte[1], M. Simon[1], B. Sartori[2], M. Rappolt[2,3]

1.) Biotechnical Faculty, University of Ljubljana, Slovenia
2.) Institute of Inorganic Chemistry, Graz University of Technology, Austria
3.) School of Food Science and Nutrition, University of Leeds, United Kingdom

Nanomaterials are an exciting new class of material used for several value added applications. It is commonly believed that first interactions of nanoparticles (NPs) with cells occur with their membranes; therefore it is of great interest to observe their possible interactions with model lipid membranes. Especially, carbon-based nanomaterials are currently considered to be one of the key elements in nanotechnology. Their potential applications range from biomedicine through nanoelectronics to mechanical engineering. Graphene is an allotrope of carbon, whose structure is one-atom-thick planar sheet. Recently it was reported that sheets of grapheme oxide have antibacterial function and thus could be useful in applications such as hygiene products or packaging that will help keep food fresh for longer periods of time [1]. Applications of C-60 fullerenes have been attracting increasing attention in different fields of research since their discovery in 1985 [2]. Different studies have suggested that C-60 my provoke formation of holes and pores in membranes, and induce changes in the structural and elastic properties of the lipid bilayer, and in its phase transformations. For example, Leroueil et al. [3] provided experimental evidence that C-60 can cause structural changes of lipid membranes that could lead to enhanced permeability by formation of an actual hole in the membrane or by more subtle changes in the composition of the membrane leading to enhanced diffusion. Furthermore, carbon black (CB) particles appear to present substantial health and environmental risks and are produced in huge quantities. Nano-sized CB has been shown to improve the performance of lithium-ion batteries among some other chemical and industrial applications. While carbon nanomaterials have excellent chemical and physical properties, carbon materials of such small size might have high toxicity and adversely affect human health [4].

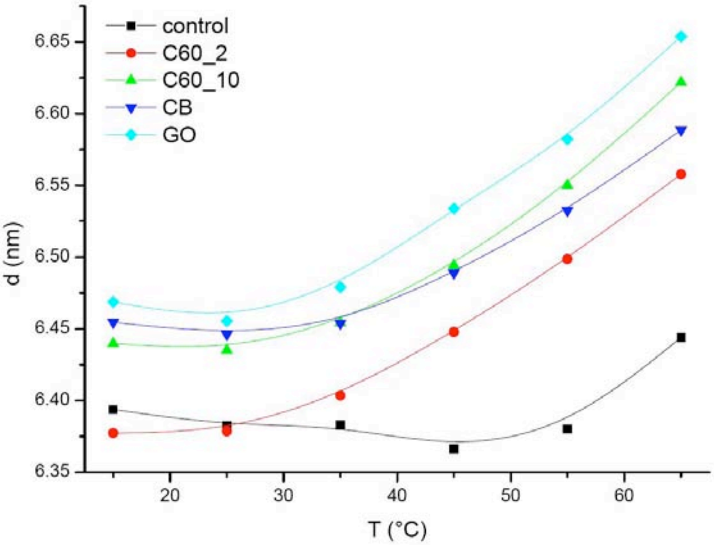

Figure 1. *D*-spacing of multilamellar POPC vesicles alone (control), and with different additional amounts of (i) C60 (C60_2; C60_10), (ii) carbon black (CB) and (iii) graphene (GO).

Our hypothesis is that carbon nanoparticles (NPs) such as fullerenes C-60 provoke structural changes of phospholipid bilayers and we have recently demonstrated that fullerenes have a potential to disturb significantly the integrity of POPC liposomes [4]. Our previous SAXS measurements demonstrated that C-60 probably disrupts the liposomes to some extent, at least locally [5]. The loss of long range order can in principle be caused by two different mechanisms: (i) bigger incorporated C-60 agglomerates (around 100 nm) might sterically perturb the membrane stacking of the MLVs and/or (ii) alternatively, it is possible that single C-60 molecules begin to adsorb into the hydrophobic core of the bilayers giving rise to stronger Helfrich undulations of the bilayers (i.e. increasing the repulsive membrane forces). Fig. 1 demonstrates our first results on the influence of different NPs on the *d*-spacing of POPC observed in the temperature range from 15 to 65 °C. As compared to the control NPs to enhance the swelling significantly, however, the underlying mechanism are still to be analyzed by applying global fitting techniques as published previously [6].

References:

[1] T. Xia, N. Li, A.E. Nel, Potential Health Impact of Nanoparticles, Annual review of public health, 2009; 30:137-150

[2] L.J. dos Santos, G.P. Rocha, R.B. Alves, R.P. de Freitas, Fullerene C-60: Chemistry and Applications. Quim Nova 2010; 33(3):680-93

[3] P.R. Leroueil, S.Y. Hong, A. Mecke, J.R. Baker, B.G. Orr, M.M.B. Holl, Nanoparticle interaction with biological membranes: Does nanotechnology present a janus face? Acc Chem Res 2007;40(5):335-42

[4] Kato H., Nakamura A., Horie M., Endoh S., Fujita K., Iwahashi H., Kinugasa S. Preparation and character ization of stabledispersionsof carbon black and nanodiamond in culture medium for in vitro toxicity assessment. Carbon 2011; 49: 3989 – 3997

[5] J. Zupanc, D. Drobne, B. Drasler, J. Valant, A. Iglic, V. Kralj-Iglic, D. Makovec, M. Rappolt, B. Sartori, K. Kogej, Experimental evidence for the interaction of C-60 fullerene with lipid vesicle membranes. Carbon 2012; 50:1170-1178

[6] G. Pabst, M. Rappolt, H. Amenitsch and P. Laggner, Structural information from multilamellar liposomes at full hydration: full q-range fitting with high-quality X-ray data, Phys. Rev. E 62, 4000-4009 (2000)

ADVANCING HIGH RESOLUTION STRUCTURAL ANALYSIS OF LIPID MEMBRANES USING A GENERIC ALGORITHM

P. Heftberger[1], B. Kollmitzer[1], M. Rappolt[2,3], H. Amenitsch[2], and G. Pabst[1]

1.) Institute of Molecular Sciences, Biophysics Division, University of Graz, Austria
2.) Institute of Inorganic Chemistry, Graz University of Technology, Austria
3.) School of Food Science and Nutrition, University of Leeds, United Kingdom

Membrane structure, in particular the membrane thickness and the lateral area per lipid are key parameters for membrane physics that can be determined from lipid bilayers in the physiologically most relevant L_α phase using SAXS. However, disorder, inherent to this phase calls for dedicated techniques to analyze their scattering data. For example, we have reported a full q-range technique (GAP) for multilamellar vesicles (MLVs) that accounts for both, Bragg peaks and diffuse scattering [1]. In addition to structural parameters, this technique allows to retrieve the fluctuation parameter, which is a measure for bending elasticity and bilayer interactions.

Recently, the structural information content has been enhanced using a more detailed description of the electron density profile [2] and a simultaneous analysis of x-ray and neutron data on unilamellar vesicles (ULVs). The backbone of the technique, termed the SDP model, are volume distributions of quasi-molecular fragments, where parsing of lipids is aided by molecular dynamics simulations (for recent reviews on the technique see [3,4]). We recently employed this description of the electron density profile (Fig. 1) in our original full q-range analysis on MLVs. The advantage of this new technique is that MLVs are more generally formed by membrane lipids than unilamellar vesicles (ULVs). ULVs can be made from MLV forming lipids, e.g. by extrusion. However, because of the high number of fitting parameters and the focus on SAXS data only, standard least square fitting routines are unable to find the global minimum in optimizing model against experimental data. Hence, we resorted to a genetic algorithm and additionally employed physically reasonable constraints to limit the parameter space [5]. Application of genetic algorithms comes at a higher computational cost,

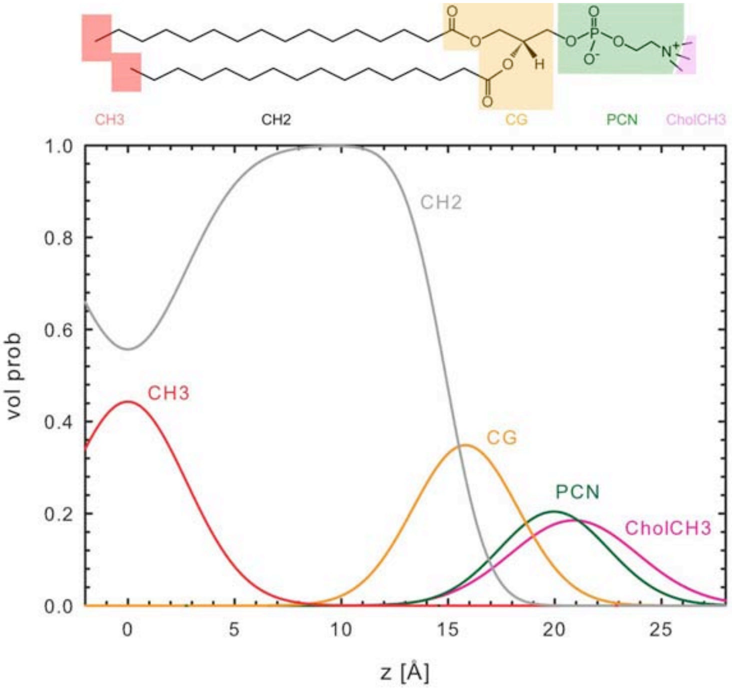

Figure 1. Parsing scheme and volume distributions of quasi-molecular fragments of DPPC.

but can be brought down to reasonable computational times using parallel processing. In order to test the technique we recorded SAXS data on a series of lipids, dioleoyl phosphatidylcholine (DOPC), palmitoyl oleoyl phosphatidylcholine (POPC), stearoyl oleoyl phosphatidylcholine (SOPC), and dipalmitoyl phosphatidylcholine (DPPC), as well as selected binary mixtures with cholesterol. Overall, our results are in excellent agreement with previous reports using the SDP model, i.e. a simultaneous analysis of neutron and x-ray data [5]. As an example, Fig. 2 shows the results for SOPC and compares the new analysis with GAP.

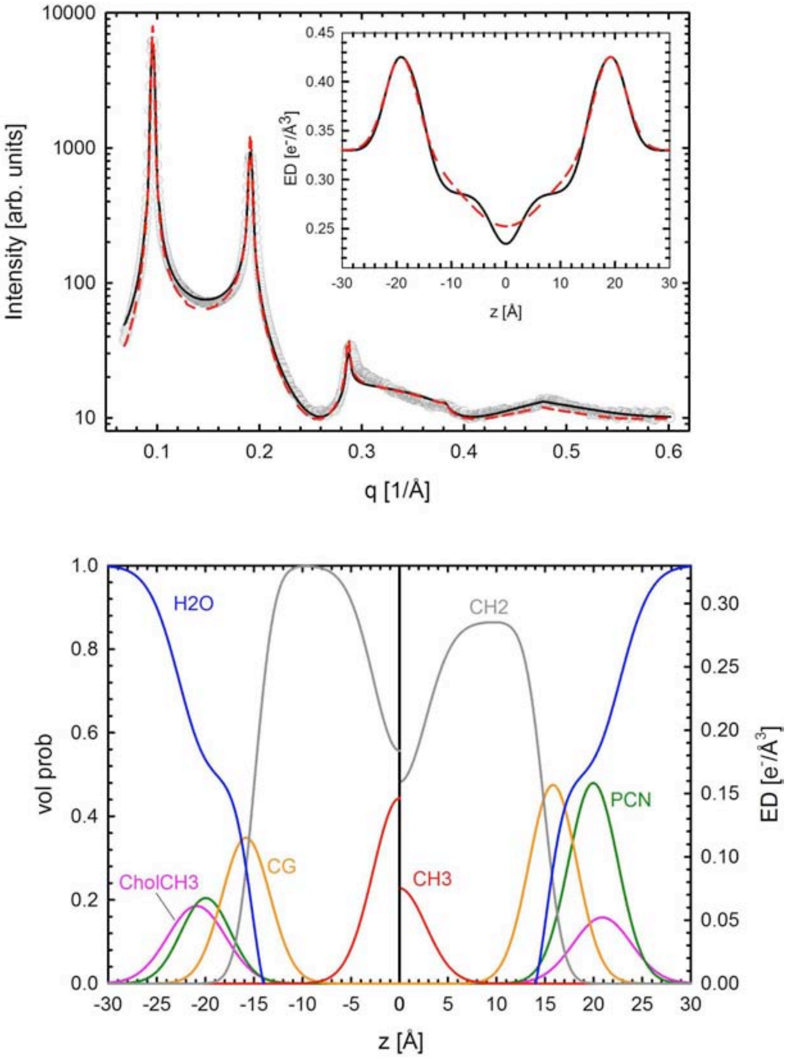

Figure 2. High-resolution full q-range analysis of SOPC MLVs. The upper panel compares the fits of the new technique (black line) with the previous analysis (dashed line). The improved structural resolution is clearly seen in the electron density profile (insert). The lower panel shows the resulting volume distributions (left hand side) and electron densities of the quasi-molecular fragments.

References:

[1] G. Pabst, M. Rappolt, H. Amenitsch, and P. Laggner, Phys. Rev. E 62: 4000–4009 (2000)

MONOLAYER SPONTANEOUS CURVATURE OF RAFT-FORMING MEMBRANE LIPIDS

B. Kollmitzer[1], P. Heftberger[1], M. Rappolt[2,3], and G. Pabst [1]

1.) Institute of Molecular Sciences, Biophysics Division, University of Graz, Austria
2.) Institute of Inorganic Chemistry, Graz University of Technology, Austria
3.) School of Food Science and Nutrition, University of Leeds, United Kingdom

We determined the monolayer spontaneous curvatures J_0 for a series of membrane lipids in the temperature range of 15°C – 55°C using SAXS on inverted hexagonal phases (H_{II}). For dioleoyl phosphatidylethanolamine (DOPE) and palmitoyl oleoyl phosphatidylethanolamine (POPE), which spontaneously form H_{II} in a given temperature range, 12 wt% tricosene was added to relieve curvature strain from interstices [1]. All other lipids, cholesterol, dioleoyl phosphatidylcholine (DOPC), palmitoyl oleoyl phosphatidylcholine (POPC), stearoyl oleoyl phosphatidylcholine (SOPC), dipalmitoyl phosphatidylcholine (DPPC), distearoyl phosphatidylcholine (DSPC) and egg sphingomyelin (SM), are bilayer-forming lipids. For these lipids J_0 was estimated by adding controlled amounts to DOPE H_{II} templates following previously established protocols (see, e.g. [2]) (Fig. 1).

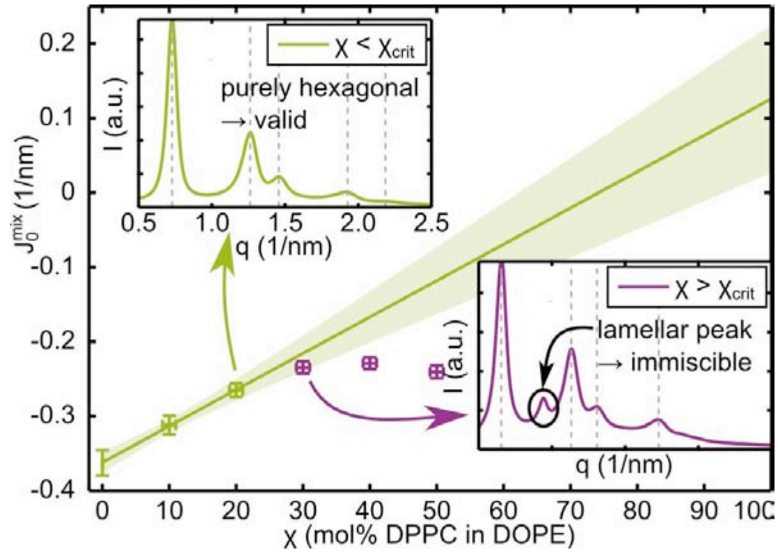

Figure 1. Determination of J_0 of DPPC at 25°C by extrapolation towards $\chi = 100$ mol%. The insets show X-ray patterns for the last valid (top left) and the first immiscible data point (bottom right).

In our analysis we compared two methods, based either on the calculation of the electron density map [3], or simple measurement of the lattice parameter [1]. Within uncertainty of the measurement both results yielded good agreement, also with previously reported values [4]. Absolute values for J_0 of PEs and cholesterol lie around 0.3 nm^{-1} and approximately one order of magnitude closer to zero for PCs and SM. A significant positive value of +0.1 nm^{-1} was found for DPPC. Further, J_0 generally decreased linearly with increasing temperature which can be attributed to the increased mobility of the hydrocarbon chains. The temperature coefficient varied in a range of -1 to -3×10^{-3} (nm °C)$^{-1}$.

Our measurements not only extend the J_0-list of lipid species [4] and add the temperature dependence, but also allowed us to estimate the monolayer spontaneous curvatures of lipid mixtures showing liquid ordered (Lo) / liquid disordered (Ld) phase coexistence [5]. Figure 2 shows the resulting spontaneous curvature phase diagrams for DSPC/DOPC/Chol, DPPC/DOPC/Chol and SM/POPC/Chol. This allowed us to discuss the effects of J_0 on protein insertion and line tension between coexisting domains [5].

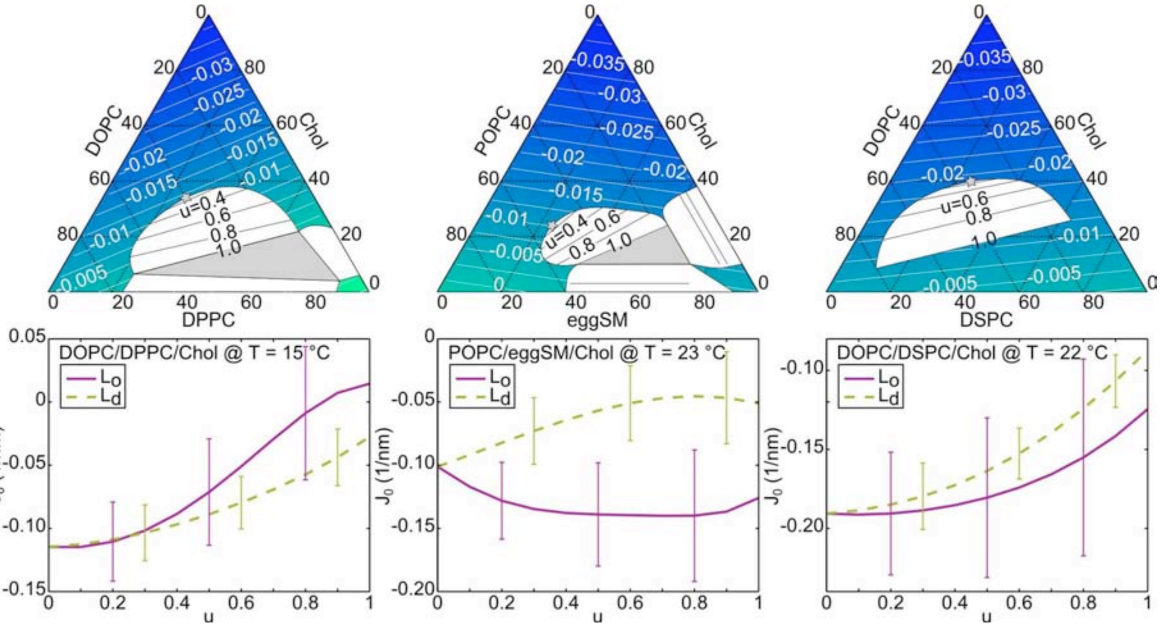

Figure 2. Spontaneous curvature for three ternary mixtures within the phase triangle (top row, units: nm^{-1}) and for coexisting Lo/Ld phases along the boundary of the fluid-fluid phase coexistence regime (bottom row).

References:

[1] S. H. Alley, O. Ces, M. Barahona and R. H. Templer, Chem. Phys. Lipids 154: 64–67 (2008)
[2] R. P. Rand, N. L. Fuller, S. M. Gruner and V. A. Parsegian, Biochemistry 29: 76–87 (1990)
[3] M. Rappolt, A. Hodzic, B. Sartori, M. Ollivon and P. Laggner, Chem. Phys. Lipids 154: 46–55 (2008)
[4] J. Zimmerberg and M. M. Kozlov, Nat. Rev. Mol. Cell Biol. 7: 9–19 (2005)
[5] B. Kollmitzer, P. Heftberger, M. Rappolt, and G. Pabst, data submitted for publication

MEMBRANE-ACTIVITY OF SURFACTANT-LIKE DESIGNER PEPTIDES ON A MODEL MEMBRANE SYSTEM

K. Kornmueller[1], C. Vonach[1], F. Cacho-Nerin[2], H. Amenitsch[2] and R. Prassl[1]

1.) Institute of Biophysics, Medical University of Graz, Schmiedlstraße 6, 8042 Graz, Austria
2.) Institute of Inorganic Chemistry, Graz University of Technology, Stremayrgasse 9, 8010 Graz, Austria

There exists a striking disparity between the actual number of membrane proteins in nature and the number of protein structures thereof solved by means of protein crystallography. Membrane protein crystallography is extremely challenging and the difficulties predominantly arise from the proteins insolubility in aqueous solutions. This problem is typically overcome by the use of detergents. An enormous variety of different detergents is available, but the right one can only be empirically determined.

A new class of detergents has attracted attention recently. Surfactant-like designer peptides mimic natural phospholipids in length and architecture, but are exclusively composed of amino acids. They typically consist of a short hydrophobic tail with consecutive hydrophobic amino acids and a polar head consisting of one or two charged amino acids [1]. They are supposed to be superior to classical detergents due to a rigidity enhancing effect on proteins as a result of intermolecular hydrogen bonding [2].

An important step in the elucidation of their delipidation mechanism is to understand how these peptides interact with membranes. Our way to address this issue was a comparative study between different surfactant-like designer peptides. Their interaction with a model membrane system (dipalmitoyl phosphatidylcholine (DPPC) multilamellar vesicles (MLVs)) has been investigated by Synchrotron SAXS, complemented with differential scanning calorimetry (DSC) and electron spin resonance spectroscopy (ESR). Thin films of DPPC and peptide at different molar ratios were prepared, hydrated with double distilled water, incubated overnight and measured with either method. Synchrotron SAXS measurements were performed at a wavelength of 0.154 nm, a sample-detector distance of 1.1 m and a photon energy of 8 keV. Data was recorded with a Pilatus detector. Samples were measured in a 1.5 mm glass capillary with an exposure time of 60 seconds and at a temperature of 25 °C. Temperature scans were performed from 25 °C to 55 °C to 25 °C.

Figure 1 illustrates the different SAXS patterns of two surfactant-like designer peptides as a function of peptide concentration. Whilst the peptide L3K – even at the highest applied concentration - has almost no effect on DPPC multilamellar vesicles (Figure 1a), the peptide V4WD2 effects dramatic changes in membrane architecture (Figure 1b). With increasing peptide concentration, the SAXS patterns reflect a remodeling process of DPPC multilamellar into oligolamellar vesicles, indicated by the emergence of a broad shoulder between $q \sim 0.5$ and 2 nm^{-1}. Especially noticeable amongst the two highest applied peptide-concentrations is the appearance of a new peak at $q = 1.4\ nm^{-1}$, breaking the typical lamellar repeat distance *d* of MLVs, hinting at the emergence of an interdigitated phase. DSC and ESR support our hypothesis of a disintegrating effect of the peptide V4WD2 on lamellar structures. At lower peptide concentrations (1.1 – 5.5 mM) we observe in DSC thermograms a gradual broadening of the main-transition peak ($\Delta T_{1/2} = 0.16 \rightarrow 0.79$ °C), correlated with a decrease in the main-transition-temperature ($T_m = 41.7 \rightarrow 40.9$ °C). The highest peptide concentration (10.9 mM) results in a total disintegration of the membrane with considerably shifted and broadened transition peaks, an effect that correlates well with the SAXS temperature scan (Figure 1c). Furthermore, ESR data demonstrates a decreasing value for the order parameter ($S = 0.9 \rightarrow 0.7$) with increasing peptide concentrations for the peptide V4WD2.

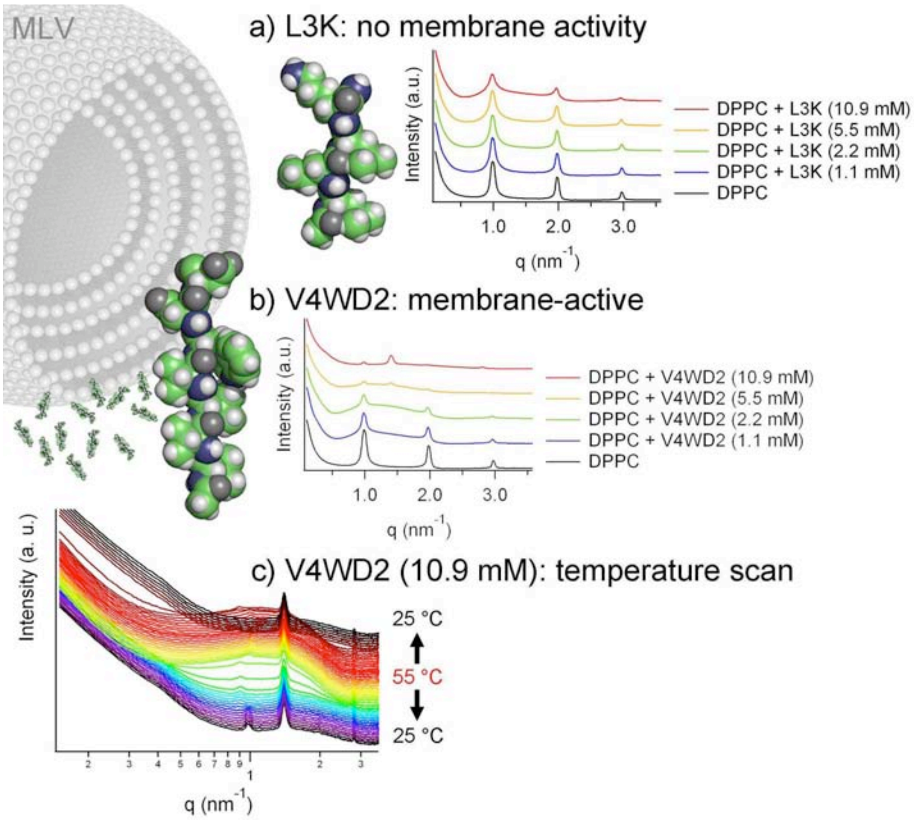

Figure 1. X-ray scattering patterns of DPPC in the presence of the peptide L3K (a) and V4WD2 (b) at different concentrations. c) SAXS temperature scan of DPPC with the peptide V4WD2 at its highest concentration.

Our results clearly suggest that it depends on both, the peptide-sequence and its concentration, whether amphiphilic designer peptides show membrane-activity or not. Thus, not all of them are suitable to be used as detergents and we remain to explore the basic mechanistic features that are accountable for the differences amongst them and try to relate structural features of the peptides to their efficiency as detergents.

References:

[1] X. Zhao, F. Pan, H. Xu, M. Yaseen, H. Shan, C. A. Hauser, S. Zhang and J. R. Lu; Molecular self-assembly and applications of designer peptide amphiphiles; *Chem. Soc. Rev.*, **39**, 3480-3498 (2010)

[2] S. Koutsopoulos, L. Kaiser, H. M. Eriksson and S. Zhang; Designer peptide surfactants stabilize diverse functional membrane proteins; *Chem. Soc. Rev.*, **41**, 1721-1728 (2012)

NANOSTRUCTURED SELF-ASSEMBLIES OF SQUALENE-BASED NUCLEOLIPIDS

E. Lepeltier[1], C. Bourgaux[1] and H. Amenitsch[2]

1.) UMR CNRS 8612, Faculté de Pharmacie, Univ. Paris-Sud, 5 rue Jean-Baptiste Clément, Châtenay Malabry, France
2.) Institute of Anorganic Chemistry, Graz University of Technology, Stremayrgasse 9/IV, 8010 Graz, Austria

The results reported are involved in a long-time study on terpenoid-based prodrugs, within the framework of an "European advanced grant" (ERC TERNANOMED, P. Couvreur)[1],[2],[3]. Drug-loaded lipidic or polymeric nanoparticles are a promising strategy for the treatment of severe diseases since they generally exhibit better activity. However, increasing drug loading over a few wt% remains a challenge and nanoparticles often exhibit a burst effect, in which a significant fraction of the drug is rapidly released upon administration. Building nanocarriers with molecules covalently bound to the drug by a cleavable linkage (prodrug) may allow to overcome these limitations.

A versatile platform delivery of nucleosidic drugs, that are currently used in clinic against cancer or viral infections like AIDS, has been designed in our laboratory. It consists in linking squalene, an acyclic isoprenoid chain precursor in the biosynthesis of sterols, to nucleoside analogues. The resulting amphiphilic molecules self-assemble in water as nanoparticles of 100-300 nm in diameter, whatever the nucleoside or nucleosidic analogue used.

When prodrugs self-organize in nanoparticles their supramolecular structure is expected to be a key parameter for their pharmacological activity. Therefore, in order to better understand the parameters which determine the structure of nanoassemblies, we have covalently coupled squalene to either the nucleobase or the sugar moiety of a library of nucleosides or nucleoside analogues (Fig1). The inner structure of nanoparticles, imaged using cryo-TEM, has been investigated by SAXS.

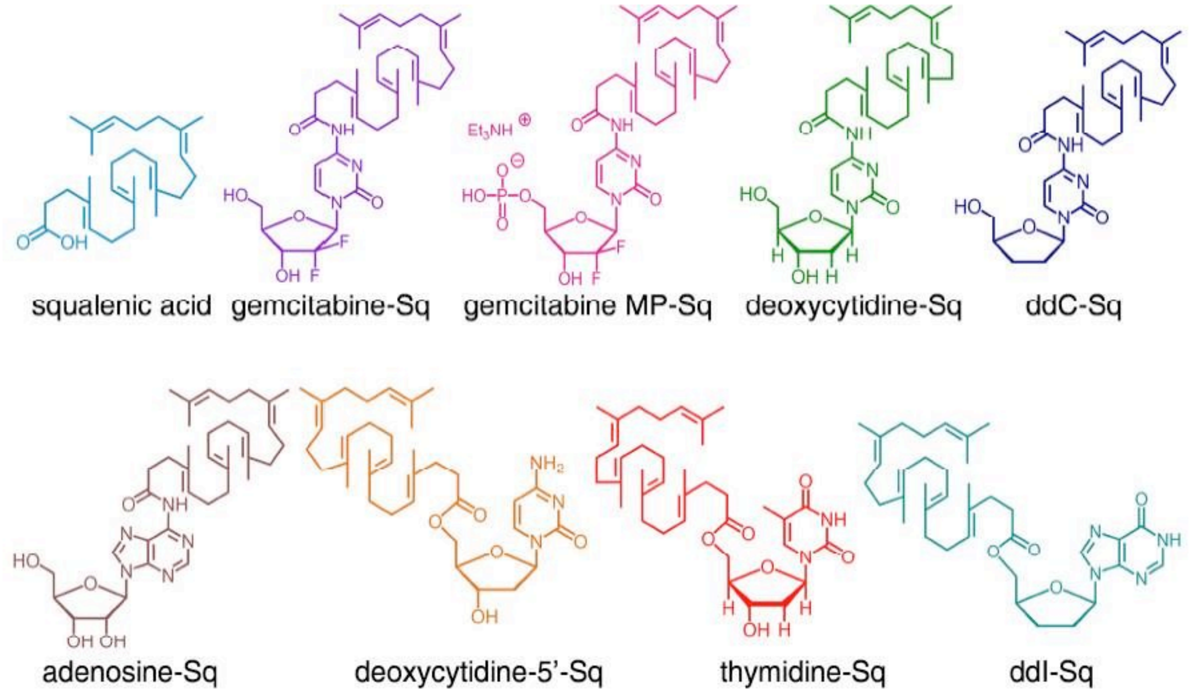

Figure 1. Chemical structures of squalenic acid and squalene –based nucleolipids.

It has been found that squalene-based nucleolipids gave rise to nanoparticles displaying a diversity of structures upon nanoprecipitation in water: hexosomes, cubosomes, spongosomes and multilamellar vesicles have been observed, depending on the nature of the nucleoside and the position of squalene relative to the nucleobase. Noteworthy, tiny chemical differences resulted in major differences in the self-organization of nucleolipids when squalene was grafted on the nucleobase whereas only lamellar phases were formed when squalene was linked to the sugar moiety. An article will be submitted.

References:

[1] P. Couvreur, LH Reddy, S. Mangenot, JH Poupaert, D. Desmaele, S. Lepetre-Mouelhi, B. Pili, C. Bourgaux, H. Amenitsch, M. Ollivon *Small*, 4, 247-253, (2008)

[2] B. Pili, C. Bourgaux, H. Amenitsch, S. Lepêtre-Mouelhi, D. Desmaele, P. Couvreur and M. Ollivon *BBA*, 98, 1, 19-28, (2010)

[3] L. Bildstein, B. Pili, V. Marsaud, S. Wack, F. Meneau, S. Lepêtre-Mouelhi, D. Desmaële, C. Bourgaux, P. Couvreur, C. Dubernet. Eur. J. Pharm. Biopharm., 79, 612-620, (2011)

THE CONTROVERSIAL ROLE OF HSP60

M.G. Ortore[1], S. Vilasi[2], D. Bulone[2], V. Martorana[2] , P. San Biagio[2], F. Cappello[3], F. Spinozzi[1] and P. Mariani[1]

1.) Department of Life and Environmental Sciences, Marche Polytechnic University and CNISM, Ancona, Italy
2.) Institute of Biophysics, National Research Council, Palermo, Italy
3.) Department BIONEC, University of Palermo, Palermo, Italy

Human Hsp60 is a mitochondrial chaperone encoded in a nuclear gene and synthesized in the cytosol with a 26-amino acid long mitochondrial import signal (MIS) at its N-terminus, which drives its translocation into the organelle where the MIS is cleaved. Inside mitochondria, it is expected that Hsp60 forms heptameric rings that assemble into double-ring chaperoning complexes [1, 2]. However it is not known if the cytosolic Hsp60 with its MIS, native Hsp60, also forms hepta- and tetradecamers. This is a key question because Hsp60 also resides and functions in the cytosol, plasma cell membrane, secretory vesicles and extracellular space, including blood. In particular, this answer might help to understand the physiological and pathogenic roles of extramitochondrial Hsp60. Hence, we compared recombinant native Hsp60 with the prokaryotic homolog GroEL, which under normal conditions forms functional double-ring tetradecamers. Also, we investigated the interactions between Hsp60 and caspase-3 in solution, which can represent an important key to clarify the mechanisms inducing apoptosis in the cytosol.

Characteristic sizes of GroEL and HSP60 were investigated by small angle X-ray (SAXS) and static and dynamic light scattering (SLS and DLS) in solution under similar physicochemical conditions. High Performance Liquid Chromatography (HPLC) and blue native polyacrylamide-gel electrophoresis were used to further clarify the equilibrium between the different oligomeric species of the two proteins over a wide range of concentrations, too. Native Hsp60, similarly to GroEL, oligomerized and formed hepta- and tetradecamers, depending on concentration, but the concentrations required for tetradecamerization were higher for Hsp60 than for GroEL, suggesting a noticeable and interesting difference in their association free energy. SAXS data (see Figure 1) proved that Hsp60 and GroEL, in their tetradecameric forms, show some differences, although the extensively studied human and bacterial homologs were until now considered structurally similar [1].

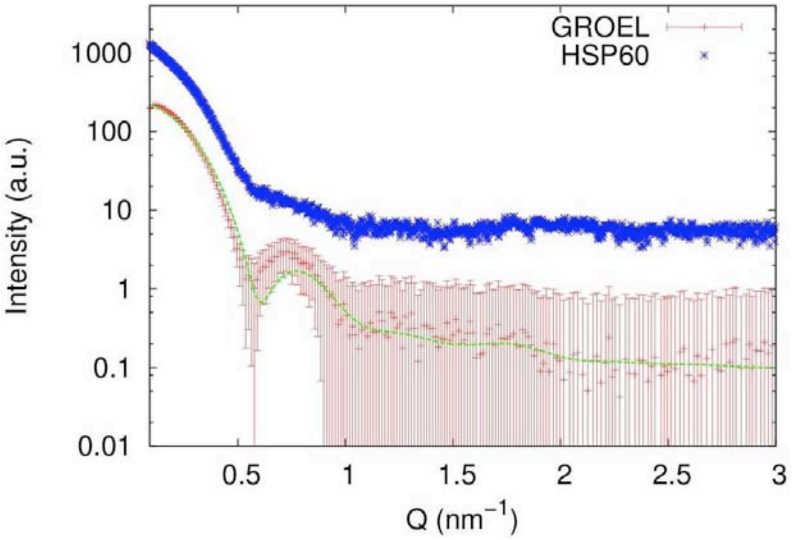

Figure 1. SAXS curves corresponding to Hsp60 and GroEL in solution, both at pH 7.5; curves are shifted for clarity. The theoretical fitting curve corresponding to GroEL was obtained by considering PDB entry 1XCK [3], according to the method described in [4].

While SAXS curve corresponding to GroEL in solution can be satisfactorily fitted by considering the crystallographic structure (Figure 1), SAXS signal corresponding to Hsp60 in solution paves to way to two different hypothesis. On one hand, a different structure of Hsp60 in respect to GroEL can be supposed, hence reconstructed at low resolution from SAXS signal, on the other hand, an equilibrium between different oligomeric species can be supposed even at the concentration investigated by SAXS. DLS and HPLC results suggest that an heptameric aggregate should be present in the solution of Hsp60 at the concentration investigated by SAXS.

Despite some crucial points concerning Hsp60 structure are still to be resolved, the binding between caspase-3 and Hsp60 can be confirmed by data reported in Figure 2. According to Guinier approximation, SAXS curve corresponding to Hsp60 in presence of caspase-3 refers to a complex whose gyration radius is Rg=(63.9 ± 0.9) Å, while without caspase-3, Hsp60 gyration radius results bigger: Rg=(79 ± 1) Å. Hence, caspase-3 probably promotes Hsp60 oligomerization and/or compression. This binding will be clarified after Hsp60 structural reconstruction. It has to be noticed that Hsp60/caspase-3 sample was measured at fixed time steps, too, but no modification of SAXS signal was evidenced in about 80 minutes.

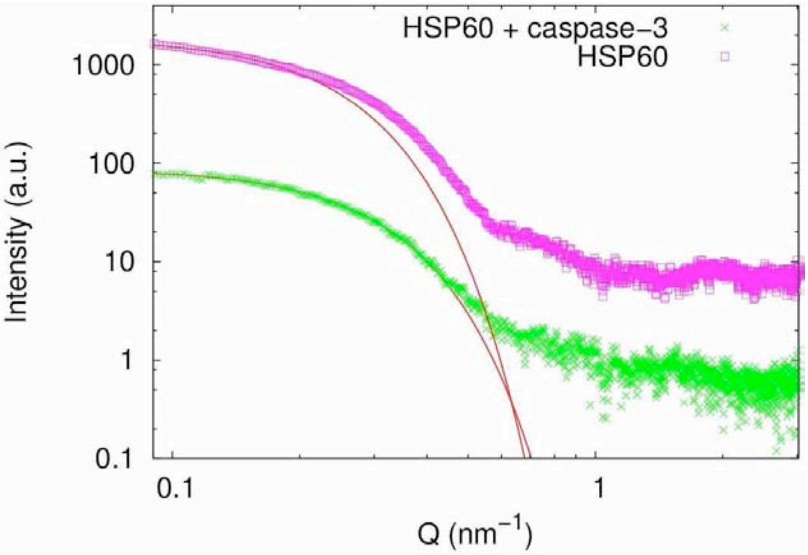

Figure 2. SAXS curves corresponding to Hsp60 in solution, at pH 7.5 and at concentration 1.6 g l^{-1}, with and without caspase-3 at 0.06 g l^{-1}; curves are shifted for clarity. Red continuous lines refer to Guinier fitting approach.

Also, since cytoplasmic and mitochondrial Hsp60 differ from each other in the signal sequence of 26 amino acid residues at the N terminus, we investigated both of them, evidencing that cytoplasmic Hsp60 species (without the 26 amino acids residues tail) aggregates even at low concentration (data not reported here). Further purification protocols are still in progress in order to obtain monodisperse cytoplasmic Hsp60.

References:

[1] N.A. Ranson et al.; Chaperonins; Biochem. J. **333**, 233–242 (1998)
[2] A. M. Merendino et al.; Hsp60 Is Actively Secreted by Human Tumor Cells; Plos One. **5(2)**, e9247 (2010)
[3] C. Bartolucci et al.; Crystal structure of wild-type chaperonin GroEL. J.Mol.Biol. **354**, 940-951 (2005)
[4] Ortore MG et al.; Combining structure and dynamics: non-denaturing high-pressure effect on lysozyme in solution. J. R. Soc. Interface **6**; S619-S634 (2009)

ENZYMATIC REACTION ON DNA MODIFIED GOLD NANOPARTICLES

P. Parisse[1], L.Ianeselli[2], F. Cacho-Nerin[3], H. Amenitsch[3] and L. Casalis[4]

1.) INSTM-ST UNIT, S.S.14 km 163.5 in Area Science Park, Trieste, Italy
2.) SISSA, via Bonomea, 265, Trieste, Italy
3.) Institute of Anorganic Chemistry, Graz University of Technology, Stremayrgasse 9/IV, 8010 Graz, Austria
4.) Elettra - Sincrotrone Trieste S.C.p.A., S.S.14 km 163.5 in Area Science Park, Trieste, Italy

We performed SAXS experiments on solutions containing 10-15 nm Au nanoparticles functionalized with ssDNA, dsDNA and mixed ssDNA/top terminated oligo ethylene glycol 6 (TOEG6) self assembled monolayers. The experiments were carried out as a function of salt concentration and in different buffers as a preliminary study for the helicase reactions.Also the helicase reactions were carried out for bacterial and human RecQ helicases and SAXS data were acquired as a function of reaction time. The analysis of the SAXS data revealed very small differences between ssDNA and dsDNA functionalized nanoparticles and also the resulting action of the enzyme (unwinding dsDNA to ssDNA) was not clearly observed by SAXS measurements probably due to aggregation issues of the nanoparticles in solution.

The experimental goal of this beamtime was to carry out SAXS measurements over DNA modified gold nanoparticles under the action of RecQ family helicases to provide a direct information on kinetics and mechanism of the transient opening of DNA duplexes, a key step in many DNA metabolic processes. In a previous study by AFM measurements we tested the action of RecQ1 and RecQ enzymes onto DNA nanoarrays anchored on gold surfaces [1]. This method allowed us to estimate the unwinding rate but did not allow a real time observation of the enzymatic reaction. We therefore choose to perform a time dependent study of the enzymatic reaction on gold nanoparticles functionalized with dsDNA, according to the scheme proposed (see Figure 1): a) measure the SAXS patterns of gold nanoparticles functionalized with dsDNA; b) then separately add the protein and the ATP (needed for the start of the reaction) using the stopped flow apparatus and c) acquire the SAXS patterns as a function of time in order to monitor the variation in the gold particles structure factor due to the unwinding of the DNA duplexes. In figure 1d we report the evolution as a function of the enzyme RecQ1 incubation time of the SAXS patterns of dsDNA functionalized,10 nm diameter, gold nanoparticles. We can see that the pattern is not changing its shape but its intensity as a function of time. The decrease of the intensity is a sign of beam damaging

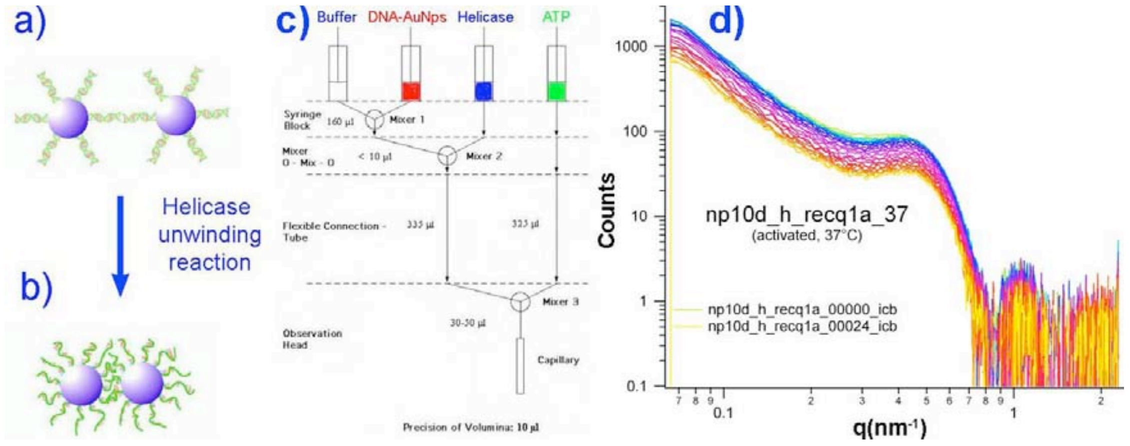

Figure 1. a-b) Schematics of the different aggregation of dsDNA (a) and ssDNA (b) functionalized gold nanoparticles. c) scheme of the stopped-flow setup used for kinetics measurements. In the scheme are highlighted the solutions injected during the experiments. d) example of SAXS patterns of DNA functionalized nanoparticles as a function of the incubation time.

effects that has been further confirmed by the analysis of the correlation function of the patterns with time (not shown here). Since beam damaging effects were affecting our kinetic experiments, we dedicated our attention to the study of the aggregation properties of ss-/ ds-DNA-functionalized gold nanoparticles with different functionalizations and in different salt conditions by means of static/single shot measurements. Functionalized nanoparticles evidenced a strong dependence of their aggregation properties on the buffer used for the analysis. We tried different buffer saline solution (milliQ water, PBS 100mM NaCl, Tris-EDTA 1/10/100/1000mM NaCl and Tris 10mM KCl 5mM MgCl2 pH 7) in order to find the saline buffer in which the patterns of ssDNA and dsDNA functionalized Au particles were more evidently distinguishable. An example of the SAXS patterns obtained for 10 nm diameter nanoparticles is reported in Figure 2. We can clearly observe that only in high salt conditions the difference due to the ss/dsDNA was more evident. SAXS patterns have been fitted with a sticky hard sphere model with a Schultz size distribution. The model considers the Au core of the particle and a potential which takes the interaction between particles due to the external shell into account. With this assumption it is possible to extrapolate some parameters as a function of salt concentration, (i.e. size and dispersion of the particles, interaction distance, etc.). Moreover we can also obtain the interparticle distance from the structure factor extrapolated by the SAXS patterns (Figure 3). Overall the model fits quite well the experimental data and we can conclude that the particles appear monodisperse in size but strongly aggregated. In fact the interparticle distance that can be extrapolated by the fitting is about 1-2 nm, indicating that the "hairy" Au nanoparticles are on average too close each other and the DNA brushes are so interpenetrated that no effects related to the de-hybridization can be observed. Alternatively, the particles are so aggregated even before the functionalization step that only the external surface could be hybridized, i.e. there is no DNA inside the gold nano aggregates.

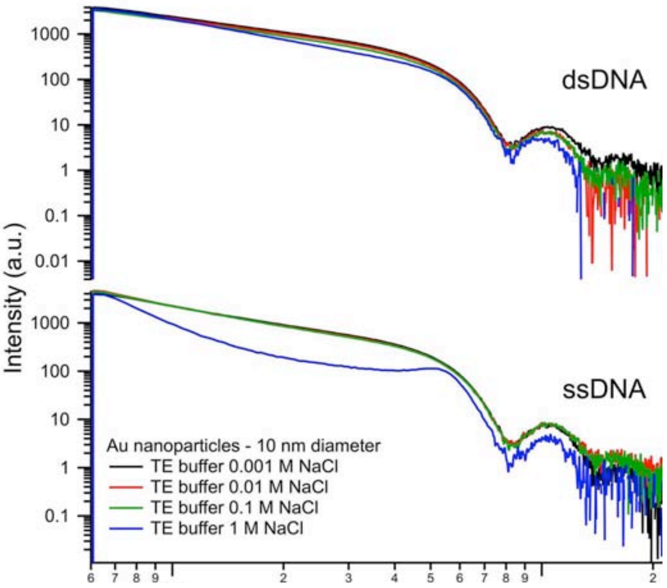

Figure 2. SAXS patterns of dsDNA (upper panel) and ssDNA (lower panel) functionalized gold nanoparticles acquired in TE buffers with different NaCl concentration.

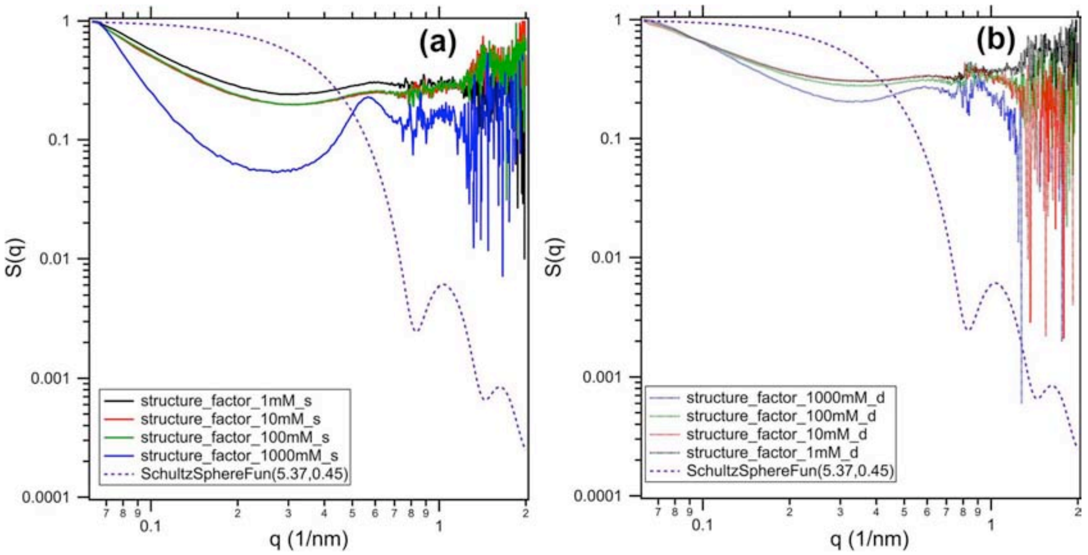

Figure 3. Structure factor for ssDNA (a) and dsDNA (b) functionalized gold nanoparticles acquired in TE buffers with different NaCl concentration. We assumed a Schulz distribution for the particles with radius=5.37nm and with a dispersion of +/- 0.45 nm (dashed lines).

In conclusion hybridization/dehybridization of DNA functionalized nanoparticles was not detected. The aggregation of the gold nano particles prevented the observation of hybridization/dehybridization because of a reduced DNA coverage of the nanoparticles and/or a poor hybridization efficiency. A better control of the original particles and of the functionalization is needed to enhance the ss/dsDNA differences ant therefore to allow the kinetic measurements of Helicase which was the aim of the present proposal. The use of two set of differently functionalized particles with partially complementary ssDNA could help the visualization of the unwinding. In this case we could separately check the two different sets, then putting them together and observe the aggregation due to the hybridization, and finally adding the enzyme we could follow the evolution of the SAXS pattern due to the separation of the aggregate.

References:

[1] P. Parisse, A. Vindigni, G. Scoles, L. Casalis, In Vitro Enzyme Comparative Kinetics: Unwinding of Surface-Bound DNA Nanostructures by RecQ and RecQ1; Journal of Physical Chemistry Letters **3**, 3532-3537 (2012)

IMPACT OF POLYXYLGLYCERIDE-BASED EXCIPIENTS ON API RELEASE FROM LIPID PARTICLES: FOCUS ON API CRYSTALLINITY AND POLYOXYLGLYCERIDE HYDRATION

F. Séquier[1,2], V. Faivre[1], M. Renouard[2], G. Daste[2] and S. Lesieur [1]

1.) Institut Galien – UMR CNRS 8612, 5 rue JB Clément, 92296 Châtenay-Malabry, France
2.) SANOFI, Ambarès, France

More than 35% of commonly used active pharmaceutical molecules are classified as poorly water-soluble according to the Biopharmaceutics Classification System. In addition, Lipinski (1996) pointed out that leads obtained with high-throughput screening tend to have even higher molecular weights causing greater lipophilicity than older leads. In the case where such a lead is transformed into a conventional drug, classical formulation strategies are no longer adequate to achieve acceptable bioavailability. Although a number of alternative technologies are being developed, lipid-based formulations have shown promise in enhancing the bioavailability of lipophilic drugs. In the laboratory; a particular method is used, the prilling, which consists on excipients heating, above their melting temperature, followed by extrusion of molten solution through nozzles. By applying a vibration to the nozzles, the jet breaks into calibrated droplets of product which will crystallize by falling into a temperature controlled atmosphere. The monodisperse final microspheres have size around 300-400 µm [1].

For first couples of excipient and API, some very encouraging results about the drug release mechanism from lipid microsphere have been obtained. Combining SRµCT and X-Ray Diffraction (XRD), it has been shown that the disappearance of drug crystals coincides with the progression of the dissolution liquid [2]. This indicates that API solubilization simultaneously occurs with water diffusion inside the inert lipid matrix and channels revealed by SRµ-CT are very likely located at sites where drug molecules crystallized during prilling. These *in-situ* created channels (at the resolution used, the drug-loaded microparticles are non porous) have been used by the drug to diffuse into the dissolution medium. This diffusion is mainly governed by drug concentration gradients.

With the present project, we want to continue such kind of work on API release mechanism from lipid microspheres. The experiments were focused on the influence of macrogolglycerides onto release kinetics. Macrogolglycerides, or polyoxylglycerides, are mono- and diesters of polyethyleneglycol which are classically used to accelerate/modulate the release rate from lipid microspheres. Thus, during the release process and depending on their distribution into the lipid matrices, these excipients could modify wettability but also size and tortuosity of the pores. Furthermore, as they have a complex behaviour depending on their hydration, compared to non polar excipients which are less lyotropic, some changes into the matrices will occur compared to initial experiments.

Several formulations based on glyceryl behenates (Speziol® GDB) or palmito-stearate monoacylglycerol (Imwitor® 491) and containing various amounts of polyglycerides (Gelucire® 50/13) and/or API of interest have been investigated on the Austrian SAXS and SYRMEP (µCT) Elettra beamlines. In order to understand the drug release mechanisms particular focuses have been done on the "thermotropic dynamics" induced by isothermal experiments at 37°C (without buffer) and "lyotropic dynamics" induced by the microparticles hydration during the dissolution process.

For example, Figure 1 describes the structural events occurring in the SAXS region during the first 20 minutes following the hydration (buffer) of microspheres containing 61% of Speziol® GDB, 26% of Imwitor® 491 and 13% of API. Thanks to the individual analysis of the microsphere components, and taking into account the changes only due to the incubation temperature (37°C), it was possible to follow three distinct events during the microsphere hydration. The change at the lower q (Figure 1) corresponds to the Gelucire® 50/13 hydration, especially to the PEG chains which also lost the helical organization they have in the solid anhydrous state (WAXS data, not shown). The reflection between 0.8 and 4.1 nm^{-1} corresponds to four order of the lamellar organization of the Speziol® GDB which clearly show that this excipient is not sensitive to the aqueous media during release process. However, this excipient is altered by temperature as a progressive transition from sub-α to α subcells has been observed both with anhydrous and hydrated microspheres during isothermal incubation at 37°C for several hours (WAXS data, not shown). At last, the dissolution of the API crystals within the particles leads to the decrease of the intensity/surface area of the reflections at 4.20 and 4.27 nm^{-1}.

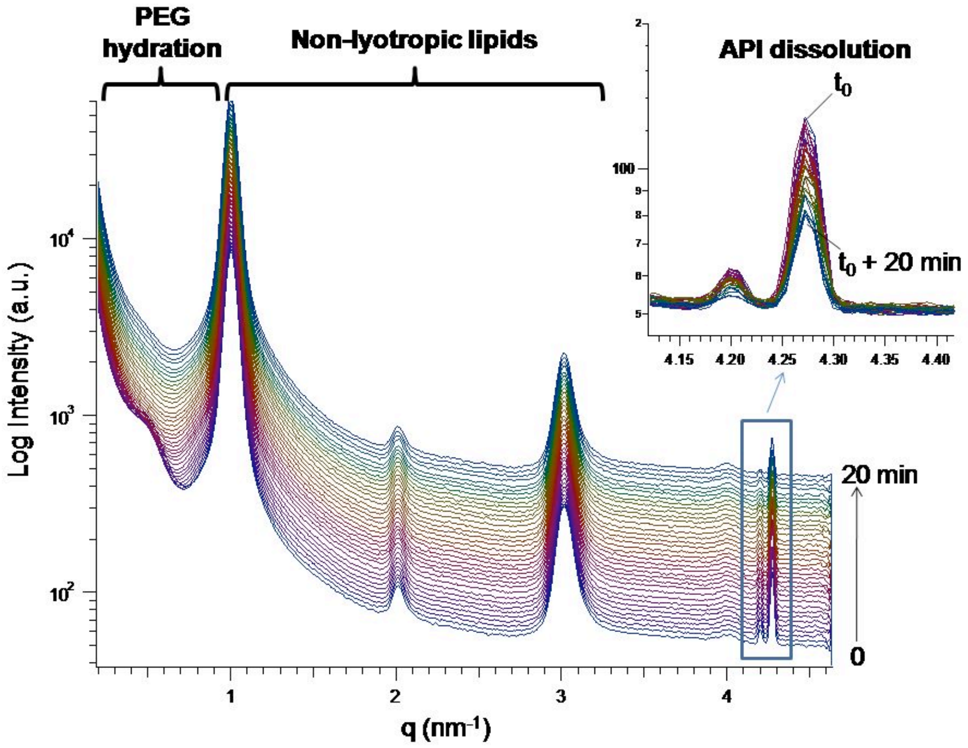

Figure 1. X-ray scattering pattern (SAXS) of microspheres containing 61% of Speziol® GDB, 26% of Imwitor® 491 and 13% of API during their hydration

These experiments were completed with API release studies and µCT experiments also made at Elettra (SYRMEP Lab). Combining all these results, fine description of the events and kinetics leading to the API release could be proposed for totally inert matrices with Speziol® GDB and for more fragile microspheres with Imwitor® 491 which tend to be fragmented during the hydration process. A paper is on progress on these.

References:

[1] P. Pivette, V. Faivre, G. Daste, M. Ollivon, S. Lesieur; Rapid cooling of lipid in a prilling tower: theoretical considerations and consequences on the structure of the microspheres; J. Therm. Anal. Calorim **98**, 47-55 (2009)

[2] P. Pivette, V. Faivre, L. Mancini, C. Gueutin, G. Daste, M. Ollivon, S. Lesieur; Controlled release of a highly hydrophilic API from lipid microspheres obtained by prilling: analysis of drug and water diffusion processes with X-ray based methods; J. Cont. Rel. **158**, 393-402 (2012)

CHARACTERIZATION OF BUPIVACAINE-LOADED FORMULATIONS OF LYOTROPIC LIQUID CRYSTALLINE PHASES AND MICROEMULSIONS

A. Yaghmur[1], M. Rappolt[2,3], J. Østergaard[1], C. Larsen[1] and S. Weng Larsen[1]

1.) Department of Pharmacy, Faculty of Health and Medical Sciences, University of Copenhagen, Universitetsparken 2, DK-2100 Copenhagen, Denmark
2.) Institute of Anorganic Chemistry, Graz University of Technology, Stremayrgasse 9/IV, 8010 Graz, Austria
3.) School of Food Science and Nutrition, University of Leeds, University of Leeds, Leeds, LS2 9JT, UK

This report details the structural characterization and the *in vitro* drug release properties of different local anaesthetic bupivacaine (BUP)-loaded inverted type liquid crystalline phases and microemulsions. The effects of variations in the lipid composition and/or BUP concentration on the self-assembled nanostructures were investigated in the presence of the commercial distilled glycerol monooleate Myverol® 18-99K (GMO) and medium-chain triglycerides (MCT). Synchrotron small-angle X-ray scattering (SAXS) and rotating dialysis cell model were used to characterize the BUP formulations and to investigate the *in vitro* BUP release profiles, respectively. The evaluation of SAXS data for the BUP-loaded GMO/MCT formulations (Figure 1) indicates the structural transition of inverted type bicontinuous cubic phase of the symmetry Pn3m → inverted type hexagonal (H_2) phase → inverted type microemulsion (L_2) with increasing MCT content (0-40 wt%). In the absence of MCT, the solubilization of BUP induces the transition of Pn3m → H_2 at pH 7.4; whereas a transition of Pn3m → (Pn3m + H_2) is detected as the hydration is achieved at pH 6.0.

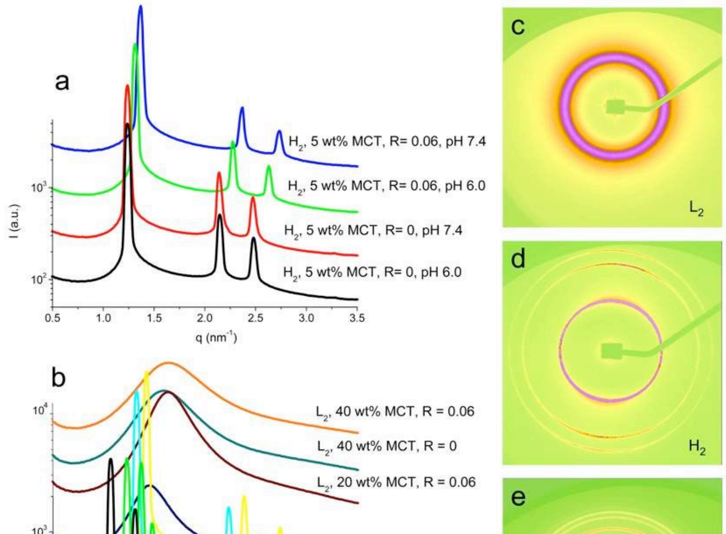

Figure 1. Structural characterization of BUP-free (*R* = 0) and BUP-loaded (*R* = 0.06) fully hydrated systems in the presence of MCT at 37 ºC. (a) pH-dependence of BUP-free and BUP-loaded fully hydrated H_2 phase consisting of GMO/MCT at a weight ratio of 95/5. These investigated samples containing 50 wt% PBS 7.4 or PBS 6.0 (PBS is a phosphate buffer solution) were prepared under equilibrium conditions. (b) The effect of varying lipid composition on the BUP-free and BUP-loaded fully hydrated nanostructures of samples containing 50 wt% PBS 6.0. The MCT content in the GMO/MCT binary mixture was varied in the range of 0-40 wt%. The scattering curves are shifted by an arbitrary constant for better visibility. Panels (c)-(e) show representative examples of SAXS 2D detector patterns for the following samples prepared with PBS 7.4: (c) MCT-loaded L_2 phase contains GMO/MCT mixture at weight ratios of 95/5 (c), (d) MCT-loaded H_2 phase contains GMO/MCT mixture at weight ratios of 80/20, (e) MCT-free Pn3m cubic phase. R is the solubilised drug to lipid weight ratio.

In order to mimic the drug release and transport from *in situ* formed self-assembled systems after subcutaneous administration, the release experiments were performed by injecting *low viscous* stimulus-responsive precursors to a buffer in the dialysis cell leaving the surface area between the self-assembled system and the release medium variable. Our results suggest that the pH-dependent variations in the lipidic partition coefficient, $K_{l/w}$, between the liquid crystalline nanostructures and the surrounding buffer solution are significantly affecting BUP release rates. This pH sensitivity is consistent with our SAXS data: the increased incorporation of BUP into the lipidic matrix induces a full structural transition from Pn3m cubic phase to H_2 phase at pH 7.4; whereas a complete transition is prevented at the investigated drug loads (*R* values) at pH 6.0. In latter case 99.2% of BUP is ionized; whereas the fraction of uncharged form of BUP increases to 16 % at pH 7.4 leading to a relatively higher amount of BUP embedded in the lipid membrane. After exposing the BUP-loaded GMO/MCT preformulations to either PBS 6.0 or PBS 7.4, the *in situ* formation of the self-assembled nanostructures is supposed to take place very fast, within about 15 min as recently reported [1]. This means that the increased level of BUP ionization with decreasing pH from 7.4 to 6.0 enhances the preferential localization of the drug molecules in the hydrophilic nanochannels of the self-assembled systems and in the surrounding excess buffer in the donor compartment, which subsequently leads to a faster drug release to the acceptor compartment.
The release experiments were adequately described by apparent first-order kinetics with correlation coefficients ($R^2 > 0.98$) [2].

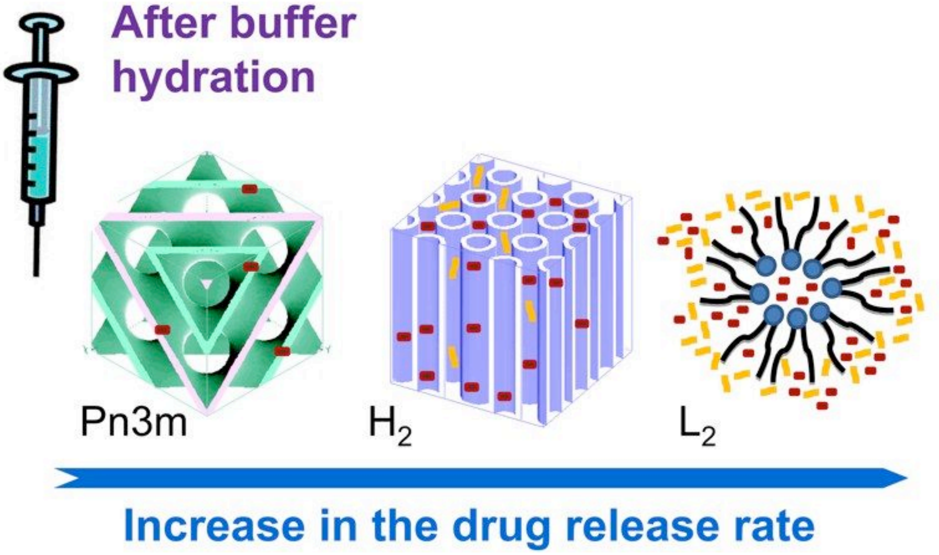

Figure 2. Schematic illustration of the effect of lipid composition on the drug release rates of different BUP-loaded lipidic formulations based on the binary GMO/MCT mixture.

A first step toward understanding of the drug release mechanism of this drug delivery class has been undertaken, tackling the influence of drug ionization as well as the type of the self-assembled nanostructure and its release kinetics under pharmaceutically relevant conditions. In investigating the *in vitro* drug release profiles, keeping the surface area between the investigated inverted type liquid crystalline phase and the release medium constant is common practice. However, in order to mimic the subcutaneous administration in a realistic manner, the release experiments in this study were performed without defining a fixed surface area between the self-assembled system and the release medium. Future studies are needed to fully understand the drug release mechanism at the nanoscale from *in situ* formed self assembled nanostructures by investigating various factors including the drug physicochemical properties (ionization and lipophilicity), the type of the self-assembled nanostructure and its release surface area, and the presence of external stimuli. This calls also for relevant *in vivo* investigations to verify these effects. These lipid-based formulations are attractive candidates for the solubilisation of local anaesthetic agents such as BUP and for extending the duration of their local anesthetic effect.

References:

[1] A. Yaghmur, S. Weng Larsen, M. Schmitt, J. Østergaard, C. Larsen, H. Jensen, A. Urtti and M. Rappolt; *In situ* characterization of lipidic bupivacaine-loaded formulations; Soft Matter **7,** 8291-8295 (2011)
[2] A. Yaghmur, M. Rappolt, J. Østergaard, C. Larsen and S. Weng Larsen; Characterization of bupivacaine-loaded formulations based on lyotropic liquid crystalline phases and microemulsions: effect of lipid composition; Langmuir 28**,** 2881-2881 (2012)

Chemistry

IN-SITU CHARACTERIZATION OF THE DEVELOPING MICROSTRUCTURE IN GEOPOLYMERS UNDER DIFFERENT EXPERIMENTAL PREPARATION CONDITIONS BY SIMULTANEOUS SAXS/WAXS MEASUREMENTS

D. Jozić[1] and S. Bernstorff[2]

1.) University of Split, Faculty of Chemistry and Technology, Telina 10/V, 21000 Split, Croatia
2.) Elettra-Sincrotrone Trieste S.C.p.A., Strada Statale 14 - km 163,5 in AREA Science Park, I-34149 Basovizza, Trieste, Italy

Geopolymerization was performed with different ratios of raw materials (metakaoline and sodium water glass) and concentrated solution of KOH with the intention to satisfy the chemical composition of the mineral mixtures shown in Table 1. The used metakaoline was prepared by calcination of kaolin (Carlo Erba). The calcination of kaolin was performed in a laboratory furnace at 750°C for 8 hours. Insitu time resolved SAXS/WAXS measurements have been performed at the Austrian SAXS beamline at the Sincrotrone Trieste. The sample to detector distance has been 2082 mm and the used photon energy 8 keV (λ=1.5 Å). The SAXS and WAXS data have been collected simultaneously by a MAR300 Image Plate and a Pilatus 100k detector, respectively. All samples were measured in two different conditions: First freshly prepared samples were measured at room temperature up to 8-11 hours of geopolymerization. Second, freshly prepared samples were kept at room temperature in sealed polyethylene cups, for at least 6 hours. Afterwards, they have been measured in a thermostated sample holder at a constant temperature of 70°C, in order to study the very important influence of the thermal activation on the process of geopolymerisation. Different compositions of mineral mixture were used with the aim to understand the parameters that are critical for the final geopolymer properties, the structural design and the porosity of the produced material, as well as to see the influence of the curing temperature on mineral mixture.

Table 1. Chemical composition of mineral mixtures used for the preparation of geopolymers, and their notation

Chemicals	Sample assignation								Recommended value
	D1	**D4**	**D7**	**D8**	**D12**	**D14**	**D17**	**D18**	
c(KOH)	7,77	8,28	8,68	8,79	9,73	10,02	8,92	9,08	**7-11**
pH	13,11	13,08	13,06	13,06	13,01	13,00	13,05	13,04	**>10**
SiO_2/Al_2O_3	3,35	3,54	3,72	3,79	4,03	3,97	3,97	3,97	**3,3-4,5**
$(Na_2O+K_2O)/Al_2O_3$	0,63	0,76	0,89	0,94	1,12	1,18	0,89	0,93	**0,8-1,6**
$(Na_2O+K_2O)/SiO_2$	0,19	0,22	0,24	0,25	0,28	0,30	0,22	0,23	**0,2-0,48**
$H_2O/(K_2O+Na_2O)$	9,56	8,61	7,94	7,76	6,50	6,05	7,81	7,53	**<13,6**

The obtained preliminary evaluation results of the WAXS data are shown in Figure 1 for two sample series denoted as D1 and D14. In the same figure is presented the WAXS pattern of metakaoline (MK750). From the first frame obtained (immediately after the start of the SAXS/WAXS experiments) it becomes clear that the curing period of the mixture (at room temperature) was long enough that the process of geopolymerization had progressed so far that a new amorphous geopolymer phase had developed. This observation was expected, and the main purpose why freshly prepared mixtures have to be kept at room temperature (or lower) is to give time for dissolving the solid amorphous alumosilicate phase from the metakaoline. From the room temperature measurement is it obvious that the process of geopolymerisation started at room temperature, and the diffuse diffraction maximum – characteristic for the amorphous phase (alumosilicate) - started to shift to higher values of

2Theta immediately after mixing the raw materials. Keeping samples at room temperature was tested just because we supposed that the process of dissolving solids (alumosilicate) from metakaoline in alkali solution is slow. Because the process of geopolymerisation takes place only when we have enough dissolved alumosilicate and enough solution of water glass, and this observation is in agreement with the literature [1].

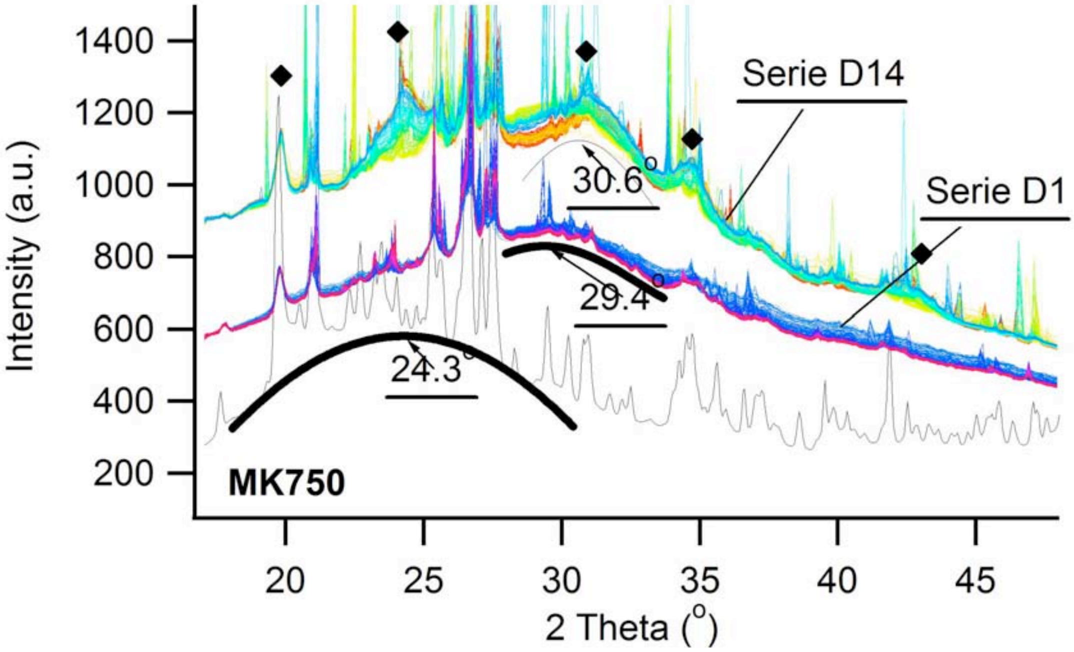

Figure 1. WAXS patterns of the geopolymer series denoted as D1 and D14, prepared at 70°C (with up to 12 hours of geopolymerization). The black line shows the WAXS pattern of metakaoline, and the peaks marked with ♦ are characteristic for Sodalite (PDF 037-0476).

The WAXS pattern of the sample denoted as MK750 is characterized by a very diffuse diffraction maximum centred at 2Theta 24.3° which arises from amorphous alumosilicate. A second diffuse diffraction maximum which belongs to the product of geopolymerization is centred at 29.4° (in the series D1) and 30.6° (in the series D14). The different positions of the diffuse diffraction maxima indicate different structural arrangements for the series D1 and D14. Another difference in the WAXS pattern is that only the D14 series shows in addition to the dominant diffuse diffraction maximum at 2Theta = 30.6 another three correlated diffuse diffraction maximums at the positions 2Theta = 24.2°, 34.9°, 42.9°. The positions of these diffraction peaks suggest the presence of structural forms, which are isostructural with the sodalite crystal form (empirical formula $Na_4Al_3Si_3O_{12}Cl$). The interpretation of the scattering curves relays, among others, on their analytical behaviour in different q regions. The SAXS measurements can determine whether the scatterers are fractal, and allow the estimation of the fractal dimension D by analysing the scattering power law. In Figure 2a and 2b are shown the scattering curves obtained for the series D1 and D14. These scattering curves were analysed in terms of fractals.

The analysis of the SAXS scattering curves indicates two areas that correspond to two different surface fractals dimensions, in both series D1 and D14. For the series D1, the characteristic q-value ranges for the two fractal dimensions are denoted as A1 ($0.10 \leq q \leq 0.20$ nm^{-1}) and A2 ($0.34 \leq q \leq 0.64$ nm^{-1}) in Figure 2a. The change of the fractal dimensions in dependence of the reaction time indicates that a major change of the fractal dimension has happened in the early phase of the geopolymerization process (up to 4 hours after thermal

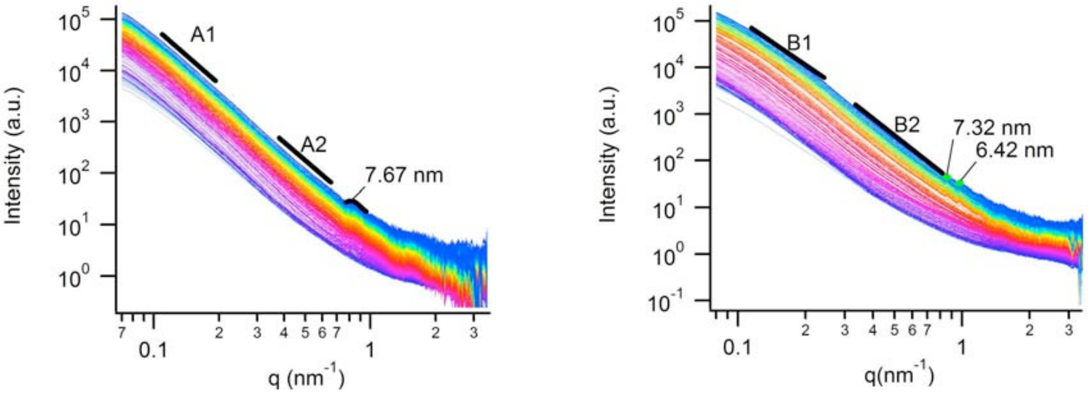

Figure 2. SAXS curves of series D1 (a) and D14 (b).

activation), while after this period the fractal dimensions remain almost constant. The final values for the fractal dimensions are D_s(A1) = 2.4 and D_s(A2) = 2.2. In Figure 2b are shown the SAXS curves of the series D14: the first fractal denoted as B1 appears in the region $0.09 \leq q \leq 0.18$ nm^{-1} and the second fractal denoted as B2 in the region $0.36 \leq q \leq 0.80$ nm^{-1}. Compared to series D1, the series D14 shows much more fluctuations of the fractal dimension, and has a longer period of the geopolymerization process (up to 11 hours). The final value of the fractal dimensions are D_s(B1)=2.8 and D_s(B2)=2.3. The SAXS curves show further, that after 8 hours starts to appear a new phase at the position d=7.67nm (series D1), and d=7.32 and 6.42 nm in series D14.

References:

[1] D. Jozić,S. Zorica, D. Tibljaš, S. Bernstorff, Insitu SAXS/WAXS study of the developing process of geopolymer structures, Proceedings of the 15th European Conference on Composite Materials. Venice, Italy, 24-28 June 2012 1-8

CRYOGENIC SYSTEM-ASSISTED SELF ASSEMBLY PROCESS IN HIGHLY ORDERED MESOSTRUCTURED THIN FILMS

H. Oveisi[1], H. Amenitsch[2], S. Bernstorff[3], B. Sartori[2] and B. Marmiroli[2]

1.) Department of Materials and Polymer Engineering, Hakim Sabzevari University, Sabzevar 9617976487, Iran
2.) Institute of Anorganic Chemistry, Graz University of Technology, Stremayrgasse 9/IV, 8010 Graz, Austria
3.) Elettra-Sincrotrone Trieste, S.S.14, km 163,5 in AREA Science Park, 34149 Basovizza, Trieste, Italy

The processing of mesoporous materials as thin films is especially important to achieve thoroughly controlled pore systems. Mesoporous films are typically produced through solvent evaporation. In this method, the films are produced after evaporation of solutions containing inorganic precursors, organic surfactants as a template, some additives (in general, acidic or complex molecules to control pH), and volatile solvents. The final mesostructures are finely controlled by adjusting initial precursor compositions, pH, aging periods, and atmospheres during solvent evaporation. Adjustment of the pore architecture of mesoporous materials strongly affects their properties, such as adsorption affinity toward guest molecules and photocatalytic properties of materials. The mesostructural ordering is strongly dependent on the aging condition after the coating process [1, 2, 3]. Recently, Oveisi et al. pointed out that the low aging temperature slowed down the hydrolysis and condensation reactions of alkoxide which favored the formation of a highly ordered mesostructure [1]. We have also found out the synchrotron SAXS can give fundamental information to investigate the self-assembly process and formation of highly ordered mesostructure during aging at -20°C.

We carefully investigated the effect of low temperature and low humidity condition by using the cryogenic system and synchrotron radiation. This was done on a cooling stage which allows simulating the -20°C aging condition used for the preparation of the highly ordered mesostructued titania film. In-situ GISAXS measurements during aging at -20°C were successfully performed on as-made film coated on micro slide glass.

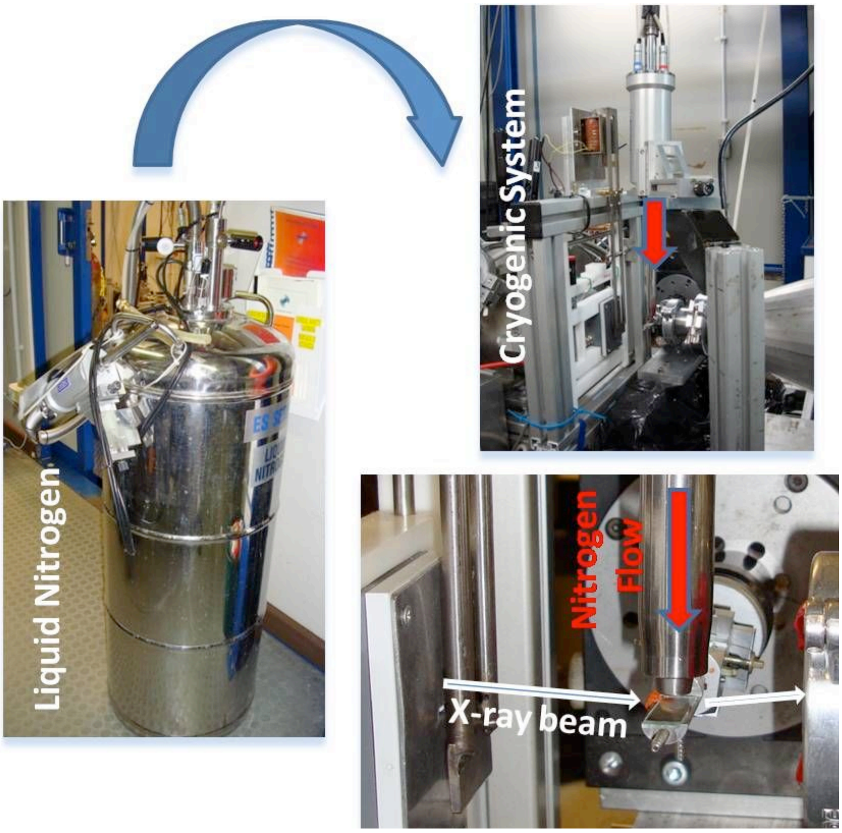

Figure 1. Illustration of the set-up combining synchrotron SAXS with a cryogenic system.

In the present investigation, we followed the procedure for making titania precursor sol with optimum synthesis parameters such as composition and pH. The solution was spin coated on micro slide glass with 3000 rpm. In order to study the structural transitions from disordered structure into well-ordered structure by aging, the as-made sample was then aged at -20°C for various time and *in-situ* SAXS measurements were done at the same time. Figure 1 illustrates the applied set-up and position of sample.

The 473 GISAXS patterns were recorded by the means of a Dectris 100K Pilatus 2D detector configured to provide scattering information in the range of 40-80 angstroms. Figure 2 shows series of GISAXS patterns of the mesostrutured titania films collected at different aging times.

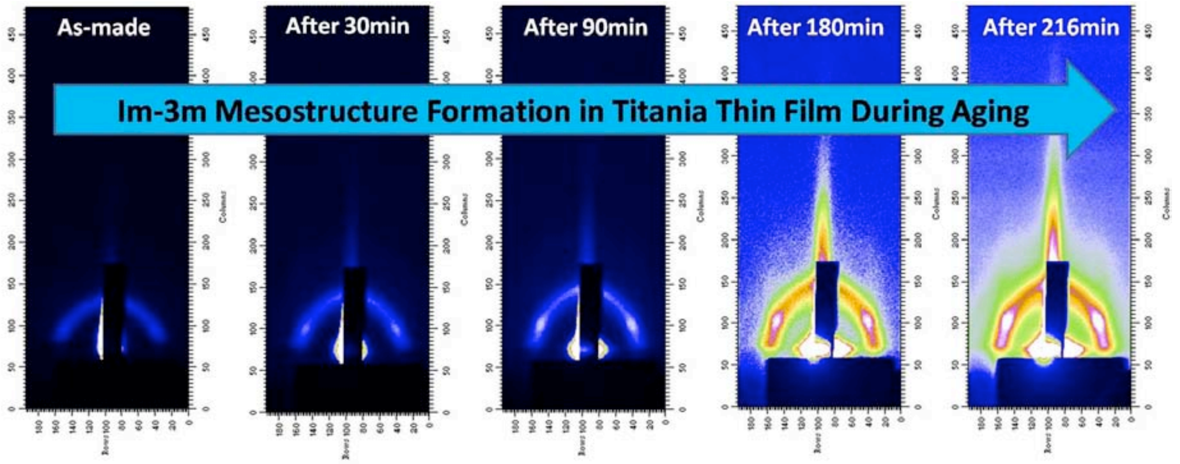

Figure 2. *In-Situ* GISAXS scattering pattern of titania thin film during aging at -20°C.

After 30 min aging at −20°C, two different spots gradually appeared. These two intense spots correspond to (110) planes in a BCC mesostructure with *Im–3m* symmetry. The *Im–3m* mesostructure was also confirmed by TEM analysis after calcinations. The (110) spots were derived from the mesostructural ordering in out-of plane direction. The basal spacing and the intensities of the (110) peaks gradually increased, as the aging periods reached to 90min. The most intense peak which was the highest ordered mesostructure appeared after 216 min aging at -20°C.

The patterns show the shrinkage along the perpendicular direction to the substrate by increasing the aging time. The significant changes in the evolution of SAXS patterns are based on a self-assembly mechanism which is in accompanied by the solvent evaporation. By increasing the aging time, the position and the intensity of (110) plane spots in out-of-plane changed. As is clear from Figure 2, by increasing the aging time up to 216 min, position of the (110) plane spots in the out-of-plane gradually moved to the higher angle. In other words, the shrinkage of the structure was unidirectional (normal direction of the substrate plane); while no contraction parallel to the substrate was observed, indicating the shrinkage along the normal direction to the substrate. The sudden enhancement of the intensity of out-of-plane (110) spots after 30min aging is due to the increase in the X-ray scattering contrast after removal of the volatile species inside the film and formation of a well ordered mesostructure. The (110) spots became stronger with a large domain up to 216 min aging time, indicating that the X-ray beam was scattered by a large number of (110) planes.

In the formation of mesostructured titania films, as the solvents such as water and ethanol evaporate gradually, the self-assembly process of the surfactants starts and their micellization is carried out. At the same time, the hydrolysis and condensation reactions of metal alkoxides also proceed. For making highly ordered mesostructures, it is ideally required that the condensation reaction of metal alkoxides should be occurred after the formation of liquid crystals (i.e., complete evaporation of solvents). Our aging condition under lower temperature (−20 °C) and low humidity (20%RH) can achieve such a suitable condition. The lower temperature avoids high rate reactions of hydrolysis and condensation of metal alkoxides. Also, low humidity accelerates the evaporation rate of water and ethanol. On the other hand, under the typical aging conditions reported previously at room temperature and 80%RH, the condensation reaction of titanium species probably proceeds before complete evaporation of the solvent [2]. Therefore, the titania aggregates are unable to form a network between micelles and ordered mesostructured films with large order domain could not be formed.

Through the present systematical study, we clarified that temperature and humidity significantly affect the mesostructural ordering. Therefore, both the low temperature and low humidity are vital for making the highest quality of mesostructured titania films. Based on the obtained results, it is considered that “low temperature” can avoid high rate reactions of hydrolysis and condensation of metal alkoxides and “low humidity” can accelerate the evaporation rate of water and ethanol. We clarified that an aging period of least 4hrs is necessary to achieve the ordered titania mesostructure. Furthermore, aging condition under low temperature and low humidity allows the formation of ordered mesostructure titania films over a wide range from pH=0.3 to pH=−0.5. Such a wide applicability to various pH conditions leads to the high reproducibility of the films.

References:

[1] H. Oveisi, N. Suzuki, Y. Nemoto, P. Srinivasu, A. Beitollahi, Y. Yamauchi; Critical effect of aging condition on mesostructural ordering in mesoporous titania thin film; Thin Solid Films, 518, 6714–6719 (2010)

[2] E.L. Crepaldi, G.d.A. Soler-Illia, D. Grosso, F. Cagnol, F. Ribot, C. Sanchez; Controlled Formation of Highly Organized Mesoporous Titania Thin Films: From Mesostructured Hybrids to Mesoporous Nanoanatase TiO_2; J. Am. Chem. Soc. 125, 9770-9786 (2003)

[3] C.J. Brinker, Y. Lu, A. Sellinger, H. Fan; Evaporation-Induced Self-Assembly: Nanostructures Made Easy; Adv. Mater. 11, 579-585 (1999)

RADIATION-INDUCED GROWTH OF CERIA NANOPARTICLES IN MESOPOROUS ORDERED FILMS

A. Pinna[1], B. Marmiroli[2], H. Amenitsch[2], P. Falcaro[3], Luca Malfatti[1] and P. Innocenzi[1]

1.) Laboratorio di Scienza dei Materiali e Nanotecnologie, LMNT-D.A.D.U., Universita`di Sassari and CR INSTM, Palazzo Pou Salit, Piazza Duomo 6, 07041 Alghero, Sassari, Italy
2.) Institute of Inorganic Chemistry, Graz University of Technology, Stremayrgasse 9/IV 8010 Graz, Austria
3.) Division of Materials Science and Engineering, CSIRO, Private Bag 33, Clayton South MDC 3169, Australia

Combination of bottom-up and top-down approach has been recently introduced for microfabricating nanodevices with advanced functional properties. In particular coatings in a "soft matter" state have been patterned with high-energy X-rays by a fast and extremely versatile protocol [1]. Integration of self-assembly method and lithography could be used to design mesoporous ordered film with metal nanoparticles (NPs) inside the porous, however patterning mesoporous film by controlled nucleation and growth of nanoparticles requires a careful optimization of the processing parameters. The controlled formation of NPs into a porous matrix would open the route to several important applications, especially in the field of nanobiotechnology [2].

In this work we have developed a method with a combination of bottom-up and top-down processing to induce ceria NPs formation within the porous of ordered titania film. Deep X-ray lithography allows controlling the nanoparticles dimension inside the mesoporous titania matrix. Crystalline cerium oxide (ceria) NPs have been chosen for their catalytic and radical scavenging properties. The functional properties of ceria NPs are related to the presence of oxygen vacancies or defects in the lattice structure, that allow switching the cerium oxidation state between III and IV [3].

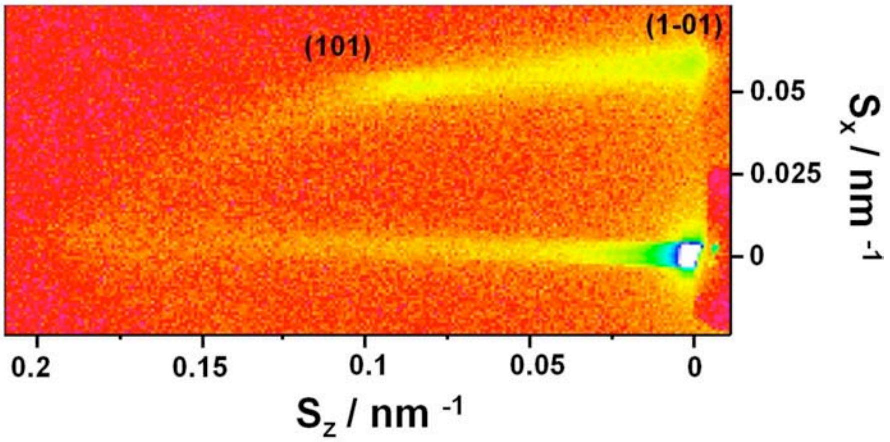

Figure 1. GISAXS pattern of a titania mesoporous film after thermal treatment at 130 °C for 24 h and 350 °C for 2 h. The pattern is characteristic of a body centered cubic mesoporous structure ($Im\bar{3}m$ space group) contracted along the [110] direction.

The synthesis of mesoporous ordered films has been achieved by self-assembly of a pore templating agent, tri-block copolymer Pluronic F127, triggered by solvent evaporation. As shown in figure 1, the obtained films showed a high degree of pore order, even after the thermal treatment at 350°C used for template removal. After calcination, the films have been impregnated with a solution containing ceria nitrate as the NP precursor and urea, CTAB or F127 as the coordinating agents. Afterwards, the samples have been exposed to hard X-rays, provided by the DXRL beamline, to induce the formation of ceria NPs within the pores. Mesoporous titania films impregnated with ceria precursor solution have been exposed to increasing radiation doses: 163 J cm^{-2}, 326 J cm^{-2} and 653 J cm^{-2}. As expected, the exposure to hard X-rays, particularly at higher doses, induced the formation of ceria NPs with selective control of the areas. In particular, we observed that only when some threshold dose value is reached, the ceria nanoparticles form. Figure 2 shows an X-ray fluorescence mapping of the patterned film after exposure and washing with ethanol to remove the residue of NP precursor. The Ce distribution provides a clear evidence of the growing of CeO_2 NPs inside the porous matrix. This result has been also cross-checked by XRD (not shown).

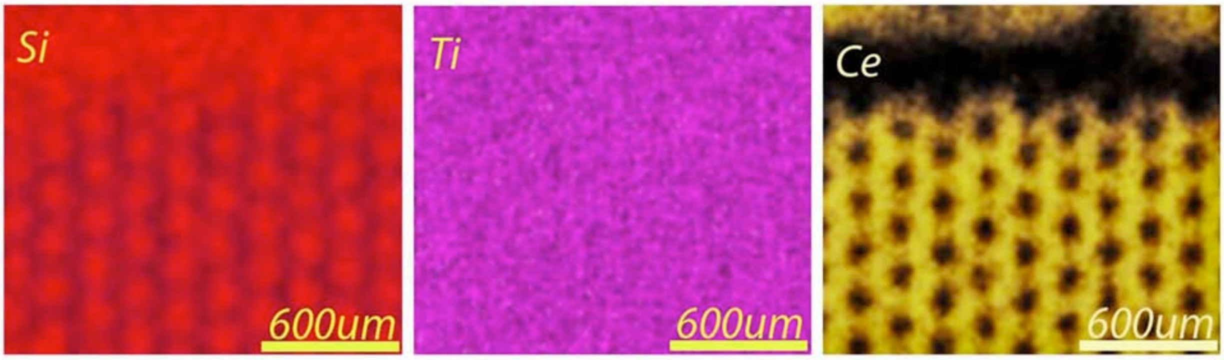

Figure 2. X-ray fluorescence map of patterned titania mesoporous film containing ceria NPs (653 J cm^{-2} exposure dose). The three different panels are reporting the signal of Si (red, left side); Ti (purple, center); and Ce (yellow, right side).

The formation of ceria nanoparticles is effective with urea and, to some extent, with Pluronic F127, however does not work with CTAB. The amines in urea play a primary role by favoring the nucleation process of ceria nanocrystals via coordination of Ce^{4+} ions, and a similar mechanism should be activated in the presence of triblock copolymers. On the other hand the CTAB, characterized by a cationic moiety, is not able to coordinate the Ce^{4+} because of the charge repulsion that disfavors the nucleation process.

Finally, to test the radical scavenging properties of the samples, we have impregnated the samples with rhodamine 6G and monitored the dye photo-degradation at increasing times. The dye degradation on the films containing ceria nanoparticles is strongly slowed down because of the anti-oxidation effect of cerium oxide. The development of these preliminary results might lead to the optimization of functional devices, such as nanocomposite NPs-mesoporous films, acting as antioxidant substrates for cell cultures.

References:

[1] P. Innocenzi, L. Malfatti, P. Falcaro; Hard X-rays meet soft matter: when bottom-up and top-down get along well; Soft Matter **8**, 3722–3729 (2012)

[2] A. Pinna, C. Figus, B. Lasio, M. Piccinini, L. Malfatti, P. Innocenzi; Release of Ceria Nanoparticles Grafted on Hybrid Organic−Inorganic Films for Biomedical Application: ACS Appl. Mater. Interfaces **4**, 3916−3922 (2012)

[3] B. A. Rzigalinski,, I. Danelisen, E. T. Strawn, C. A. Cohen, C. Liang; Nanoparticles for Cell Engineering – A Radical Concept; Nanotechnologies for the Life Sciences; Wiley: New York, (2007)

Reference to original paper: A. Pinna, B. Lasio, M. Piccinini, B. Marmiroli, H. Amenitsch, P. Falcaro, Y. Tokudome, L. Malfatti and P. Innocenzi. ACS Appl. Mater. Interfaces **5**, 3168−3175 (2013).

Used beamlines and laboratories: SAXS and Deep x ray lithography

SUPRAMOLECULAR NANOSTRUCTURES OF PHOTOSENSITIZER AND POLYOXOMETALATE DYADS

Z. Syrgiannis[1], A. Bonasera[1], A. Sartorel[2], M. Carraro[2], F. Cacho-Nerin[3], H. Amenitsch[3], G. La Ganga[4], F. Puntoriero[4], S. Campagna[4], M. Bonchio[2] and M. Prato [1]

1.) University of Trieste, Department of Chemical and Pharmaceutical Sciences, via L. Giorgieri n°1, 34127 Trieste, Italy
2.) University of Padova, Department of Chemical Sciences, via F. Marzolo n°1, 35131 Padova, Italy
3.) Graz University of Technology - Institute of Inorganic Chemistry, Stremayergasse 9/4, 8010 Graz, Austria
4.) University of Messina, Department of Inorganic, Analytical and Physical Chemistry, via F. Stagno D'Alcontres n°31, 34166 Messina, Italy

During the recent years polyoxometalate species (POMs) received the attention of international scientific community because they demonstrated how, using relatively simple and basic synthetic protocols, it's possible to produce catalytic structures able to promote several interesting chemical transformations [1]; in particular, their peculiar robustness and the possibility to combine POMs with photosensitizer (PS) make them suitable for artificial photosynthesis [2].

Recently, Ru_4POM specie showed its attitude to promote water oxidation in presence of photocatalyst $Ru(bpy)_3$, with results worthy of note [3]. With the aim to improve the performances of the system described above, a short library of pyrene-based photosensitizers has been tested in combination of Ru_4POM; the presence of the aromatic unit lengthens exited state lifetime of the transition metal centre so to make more effective the energy transfer towards POM unit. We soon recognized an improved catalytic activity from the novel materials, but also the formation of fibrous aggregates.

SAXS measurements have been performed in order to obtain information about the observed nanostructures. As blank experiment, POM solution have been analysed first, and we found one correlation peak at q = 4.32 1/nm, corresponding in a structural repeat distance of 1.45 nm, as shown in Figure 1; form this data, a natural tendency by Ru_4POM to self-organization has been put on evidence.

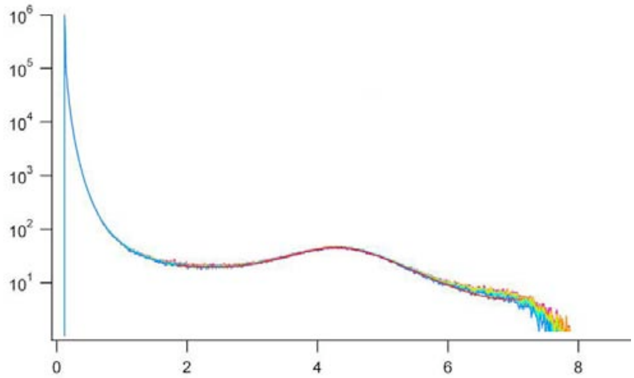

Figure 1. Ru_4POM SAXS spectrum.

Moreover we have analysed Ru_4POM with PS $Ru1(bpy)_2$ mixed 1:4 molar ratio as suggested from conductivity experiments; scanning the sample at different times, we have observed an evolution of the system which, from small and spherical nanoparticles (see Figure 2), evolves towards 2-D system, with q = 4.27 1/nm and q = 1.944 1/nm. The first distance is closer to the value of Ru_4POM solution and can be recognized as the vertical distance between POMs, while the second is compatible with the distance between 2 POM units with 2 photosensitizer molecules. According to the proposed model, the material is organized as a pyramidal-like network with each POM surrounded by 4 molecules of $Ru1(bpy)_2$, and every molecule of $Ru1(bpy)_2$ is able to π-π interact with another one, so to give further stabilisation to the network. From theoretical studies the proposed model in Figure 3 is in excellent accordance with experimental data.

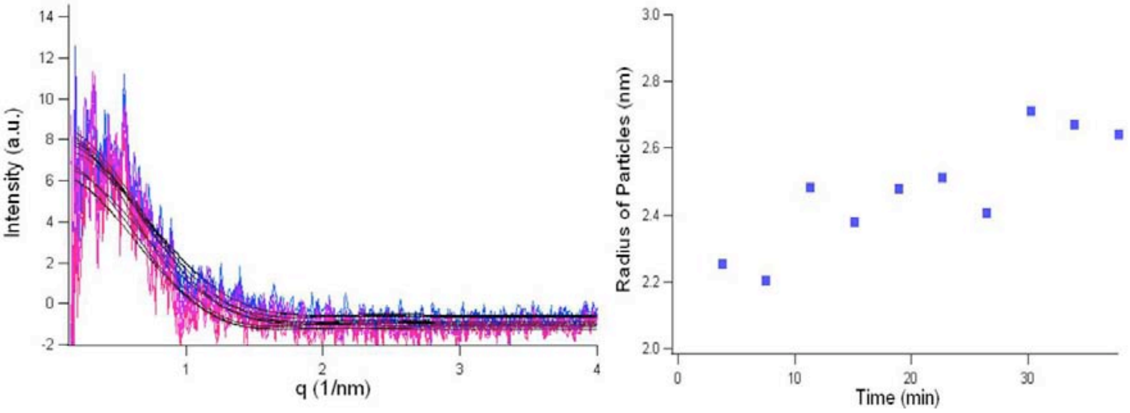

Figure 2. Ru1(bpy)$_2$@Ru$_4$POM SAXS spectrum after mixing the 2 components and size distribution diagram of the particles.

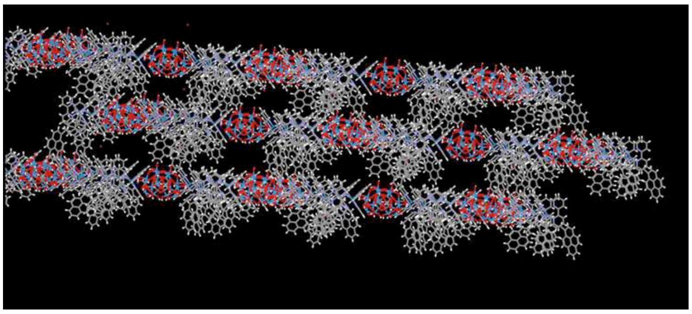

Figure 3. Theoretical model proposed for Ru1(bpy)$_2$@Ru$_4$POM system.

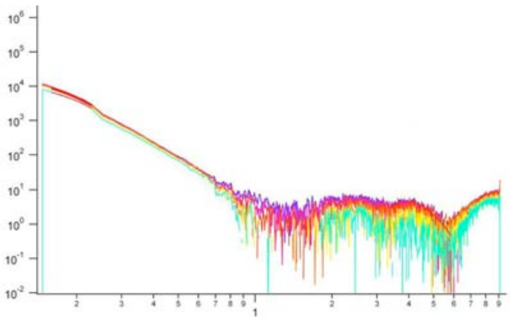

Figure 4. Ru3(bpy)$_2$@Ru$_4$POM SAXS spectrum.

We proceeded our analysis for the system Ru2(bpy)$_2$@Ru$_4$POM, Ru3(bpy)$_2$@Ru$_4$POM and Ru4(bpy)$_2$@Ru$_4$POM where we supposed to find similar evidences in the structural motif but different d-spacing values due to the more rigid or flexible connection between pyrene unit and *bipyridyl* unit, or the presence of other functional groups (-OH) able to create other intermolecular interactions. As expected, d-spacing values change a little as reported in Table 1, in particular in the case of Ru3(bpy)$_2$@Ru$_4$POM the pyramidal organization have been lost in flavour of 1-D organization (H-bonds imposed a conformation which unflavoured π-π interactions).

Surprisingly, Ru4(bpy)$_2$@Ru$_4$POM revealed that the presence of Ru(bpy)$_2$ moiety is not so important for what concerns the formation of the supramolecular aggregate; the substitution with an ammonium salt gave similar pyramidal organization, so we concluded that simple electrostatic interactions are guiding the aggregation phenomena, plus the π-π interactions between photosensitizer molecules one each other.

Summarizing, we characterized a library of catalytic nanostructures based on the combination of a POM unit and a series of pyrene-based photosensitizer; we recognized and described the evolution of the system from the mixing of the two components till the formation of the larger aggregates; we observed a common supramolecular network under the organization of the different materials due to 2 main kinds of interactions, both electrostatic and π-π stacking. Further studies are under progress to evaluate the correlation between structural organization and catalytic activity.

Table 1. Short description of samples and relevant data extracted from SAXS spectra.

Sample	pyrene-based ligand	POM/PS ratio (in moles)	d-spacing values
blank	/	Ru_4POM only	1.45 nm
Ru1$(bpy)_2$@Ru_4POM	4-methyl-4'-(2-(pyren-1-yl)ethyl)-2,2'-bipyridine	4:1	1.47 nm 3.23 nm
Ru2$(bpy)_2$@Ru_4POM	2-(4'-methyl-[2,2'-bipyridin]-4-yl)-1-(pyren-1-yl)ethanol	4:1	1.68 nm
Ru3$(bpy)_2$@Ru_4POM	(E)-4-methyl-4'-(2-(pyren-1-yl)vinyl)-2,2'-bipyridine	4:1	1.58 nm 2.57 nm
4@Ru_4POM	N,N,N-trimethyl-3-oxo-3-(pyren-1-yl)propan-1-ammonium chloride	4:1	1.36 nm 2.08 nm

References:

[1] A. Sartorel, M. Bonchio, S. Campagna, F. Scandola, Tetrametallic molecular catalysts for photochemical water oxidation, Chem. Soc. Rev. **42**, 2262-2280 (2013)

[2] N. D. McClenaghan, Y. Leydet, B. Maubert, M. T. Indelli, S. Campagna, Excited-state equilibration: a process leading to long-lived metal-to-ligand charge transfer luminescence in supramolecular systems, Coord. Chem. Rev. **249**, 1336-1350 (2005).

[3] a) M. Orlandi, R. Argazzi, A. Sartorel, M. Carraro, G. Scorrano, M. Bonchio, F. Scandola, Ruthenium polyoxometalate water splitting catalyst: very fast hole scavenging from photogenerated oxidants, Chem. Comm. **46**, 3152-3154 (2010); (b) M. Natali, M. Orlandi, S. Berardi, S. Campagna, M. Bonchio, A. Sartorel, F. Scandola, Photoinduced water oxidation by a tetraruthenium polyoxometalate catalyst: ion-paring and primary processes with $Ru(bpy)_3^{2+}$ photosensitizer, Inorganic Chemistry **51**, 7324-7331 (2012)

Publications

Publications in Journals and Reviewed Proceedings 2012

V. Allain, C. Bourgaux, P. Couvreur
Self-assembled nucleolipids : from supramolecular structure to soft nucleic acid and drug delivery devices
Nucleic Acids Research 40(5), 1891-1903 (2012)

M. Bitenc, P. Podbrščеk, P. Dubček, S. Bernstorff , G. Dražić , B. Orel and Z. Crnjak Orel
The growth mechanism of zinc oxide and hydrozincite: a study using electron microscopy and in-situ SAXS
CrystEngComm 14 (9), 3080-3088 (2012)

I. Bogdanović-Radović, M. Buljan, M. Karlušić, N. Skukan, I. Božičević, M. Jakšić, N. Radić, G. Dražić and S. Bernstorff
Conditions for formation of germanium quantum dots in amorphous matrices by MeV ions: Comparison with standard thermal annealing
Physical Review B 86 (16), 165316 [8 pages] (2012)

B. Boulgaropoulos, M. Rappolt, B. Sartori, H. Amenitsch, G. Pabst
Lipid sorting by ceramide and the consequences for membrane proteins
Biophysical Journal, Vol. 102 (9), pp. 2031-2038 (2012)

M. Buljan, N. Radić, S. Bernstorff, G. Dražić, I. Bogdanović-Radović,V. Holý
Grazing-incidence small-angle X-ray scattering: Application to the study of quantum dot lattices
Acta Crystallographica A 68 (1), pp. 124-138 (2012)

M. Buljan, U.V. Desnica, I. Bogdanović-Radović, N. Radić, M. Ivanda, G. Dražić,
S. Bernstorff and V. Holý
Preparation of regularly ordered Ge quantum dot lattices in amorphous matrices
Vacuum 86 (6), pp. 733-736 (2012)

M. Buljan, M. Karlusic, I. Bogdanovic-Radovic, M. Jaksic, K. Salamon, S. Bernstorff, N. Radic
Determination of ion track radii in amorphous matrices via formation of nano-clusters by ion-beam irradiation
Appl. Phys. Lett. 101 (10), 103112, 4 pages (2012)

D. Buso, J. Jasieniak, M.D.H Lay, P. Schiavuta, P. Scopece, J. Laird, H. Amenitsch, A.J. Hill, P. Falcaro
Highly luminescent metal-organic frameworks through quantum dot doping
Small, Vol. 8 - 1, pp. 80-88 (2012)

G. Caracciolo and H. Amenitsch
Cationic liposome/DNA complexes: from structure to interactions with cellular membranes
European Biophysics Journal, Vol. 41 - 10, pp. 815-829 (2012)

C. Cervellati, K. Montin, M. Squerzanti, C. Mischiati, C. Ferrari, F. Spinozzi, P. Mariani, H. Amenitsch, C.M. Bergamini, V. Lanzara
Effects of the regulatory ligands calcium and GTP on the thermal stability of tissue transglutaminase
Amino Acids 42(6), 2233-42 (2012)

P. Chatterjee, S. Hazra, H. Amenitsch
Substrate and drying effect in shape and ordering of micelles inside CTAB-silica mesostructured films
Soft Matter, Vol. 8 (10), pp. 2956-2964 (2012)

A. Fischereder, T. Rath, W. Haas, H. Amenitsch, D. Schenk, A. Zankel, R. Saf, F. Hofer, G. Trimmel
Investigation of CuInS2 thin film formation by a low-temperature chemical deposition method
ACS Applied Materials and Interfaces, Vol. 4 - 1, pp. 382-390 (2012)

C. Fotakis, G. Megariotis, D. Christodouleas, E. Kritsi, P. Zoumpoulakis, D. Ntountaniotis, M. Zervou, C. Potamitis, A. Hodzic, G. Pabst, M. Rappolt, G. Mali, J. Baldus, C. Glaubitz, M.G. Papadopoulos, A. Afantitis, G. Melagraki, T. Mavromoustakos
Comparative study of the AT1 receptor prodrug antagonist candesartan cilexetil with other sartans on the interactions with membrane bilayers
Biochimica et Biophysica Acta - Biomembranes, Vol. 1818 - 12, pp. 3107-3120 (2012) doi:

D. Gracin, K. Juraić, J. Sancho-Parramon, P. Dubček, S. Bernstorff, M.Čeh,
Amorphous-Nano-Crystalline Silicon Thin Films in Next Generation of Solar Cells
Physics Procedia, Vol. 32, pp. 470-476 (2012)

A. Hodzic, P. Zoumpoulakis, G. Pabst, T. Mavromoustakos, M. Rappolt
Losartan's affinity to fluid bilayers modulates lipid-cholesterol interactions
Physical Chemistry Chemical Physics, Vol. 14 - 14, pp. 4780-4788 (14 April 2012)

D. Jozić, S. Zorica, D. Tibljaš and S. Bernstorff
Insitu SAXS/WAXS study of the developing process of geopolymer structures
Proceedings of 15TH European conference on "composite materials" (ECCM15), pp. 2481-1 to 2481-8 (2012)

S. Kler, R. Asor, C.L. Li, A. Ginsburg, D. Harries, A. Oppenheim, A. Zlotnick, U. Raviv
RNA Encapsidation by SV40-Derived Nanoparticles Follows a Rapid Two-State Mechanism
Journal of the American Chemical Society **2012,** 134, (21), 8823-8830

K. Kowlgi, U. Lafont, M. Rappolt and G. Koper
Uniform metal nanoparticles produced at high yield in dense microemulsions
Journal of Colloid and Interface Science 372 (1), pp. 16–23 (15 April 2012)

S. Kralj, G. Cordoyiannis, D. Jesenek, A. Zidansek, G. Lahajnar, N. Novak, H. Amenitsch and Z. Kutnjak
Dimensional crossover and scaling behavior of a smectic liquid crystal confined to controlled-pore glass matrices
Soft Matter, Vol. 8 (8), pp. 2460-2470 (2012)

I. Krastanova, V. Sannino, H. Amenitsch, O. Gileadi, F.M. Pisani and S. Onesti
Structural and functional insights into the DNA replication factor Cdc45 reveal an evolutionary relationship to the DHH family of phosphoesterases
Journal of Biological Chemistry, Vol. 287 - 6, pp. 4121-4128 (2012)

M. Lucic Lavcevic, S. Bernstorff, P. Dubcek, D. Jozic, I. Jerkovic and Z. Marijanovic
GISAXS/GIXRD View of ZnO Films with Hierarchical Structural Elements
Journal of Nanotechnology, Vol. 2012, pp. 354809-1-354809-10 (2012)

S.S. Mandal, S. Bhaduri, H.Amenitsch and A.J. Bhattacharyya
Synchrotron Small Angle X-Ray Scattering Studies of Hemoglobin Non-aggregation Confined Inside Polymer Capsules
J. Phys. Chem. B 116, 9604−9610 (2012)

B. Marmiroli and H. Amenitsch
X-ray lithography and small-angle X-ray scattering: A combination of techniques merging biology and materials science
European Biophysics Journal, Vol. 41 - 10, pp. 851-861 (2012)

T. H. Nguyen, M. Vayer, D. Grosso, H. Amenitsch, C. Sinturel
Using sol-gel replications to assess the porosity of block-copolymer derived thin films
Journal of Physical Chemistry C, Vol. 116 (9), pp. 5295-5302 (2012)

D. Ntountaniotis, G. Mali, S.G. Grdadolnik, M. Halabalaki, A. Skaltsounis, C. Potamitis, E. Siapi, P. Chatzigeorgiou, M. Rappolt and T. Mavromoustakos
Corrigendum to "Thermal, dynamic and structural properties of drug AT1 antagonist olmesartan in lipid bilayers" [Biochim. Biophys. Acta 1808 (2011) 2995-3006]
Biochimica et Biophysica Acta (BBA) - Biomembranes, Vol. 1818 - 5, pp. 1436 (2012)

G. Pabst, R. Prassl, H. Amenitsch, M. Rappolt and K. Lohner
Scattering techniques in biology-marking the contributions to the field from Peter Laggner on the occasion of his 68th birthday
European Biophysics Journal, Vol. 41 - 10, pp. 777-779 (2012)

G. Pabst, D. Zweytick, R. Prassl and K. Lohner
Use of X-ray scattering to aid the design and delivery of membrane-active drugs
European Biophysics Journal, Vol. 41 - 10, pp. 915-929 (2012)

S. R. C. Pinto, M. Buljan, A. Chahboun, M.A. Roldan, S. Bernstorff, M. Varela. S.J. Pennycook, N.P. Barradas, E. Alves, S.I. Molina, M. M.D. Ramos and M. J. M. Gomes
Tuning the properties of Ge-quantum dots superlattices in amorphous silica matrix through deposition conditions
J. Appl. Phys. **111**, 074316 (2012)

S.R.C. Pinto, M Buljan, L. Marques, J. Martín-Sánchez, O. Conde,, A. Chahboun, A.R. Ramos, N.P. Barradas, E. Alves, S. Bernstorff , J. Grenzer, A. Mücklich, M.M.D. Ramos, and M.J.M. Gomes
Influence of annealing conditions on formation of regular lattices of voids and Ge quantum dots in amorphous alumina matrix
Nanotechnology 23 (2012) 405605 (9pp)

P. Pivette, V. Faivre, L. Mancini, C. Gueutin, G. Daste, M. Ollivon, S. Lesieur
Controlled release of a highly hydrophilic API from lipid microspheres obtained by prilling: Analysis of drug and water diffusion processes with X-ray-based methods Journal of Controlled Release, 158 (3), 393-402 (2012)

G. Polt, F. Spieckermann, H. Wilhelm, E. Schafler, M. Kerber, M.J. Zehetbauer
Effects of dislocations in γ-phase polypropylene and comparison with other semi-crystalline polymers
Extended Abstract, Proceedings of the 15th international conference on Deformation, Yield and Fracture of Polymers (DYFP), Kerkrade, The Netherlands, 2012

D. Pozzi, C. Marchini, F. Cardarelli, H. Amenitsch, C. Garulli, A. Bifone, G. Caracciolo *Transfection efficiency boost of cholesterol-containing lipoplexes*
Biochimica et Biophysica Acta - Biomembranes, Vol. 1818 (9), pp. 2335-2343 (2012)

A.V. Radhakrishnan, S. K. Ghosh, G. Pabst, V. A. Raghunathan, and A. K. Sood
Tuning DNA-amphiphile condensate architecture with strongly binding counterions
Proc. Natl. Acad. Sci. 109: 6394 - 6398 (2012)

G. Rogl, Z. Aabdin, E. Schafler, J. Horky, D. Setman, M. Zehetbauer, M. Kriegisch, O. Eibl, A. Grytsiv, E. Bauer, M. Reinecker, W. Schranz and P. Rogl
Effect of HPT processing on the structure, thermoelectric and mechanical properties of Sr0.07Ba0.07Yb0.07Co4Sb12
Journal of Alloys and Compounds 537, 183-189 (2012)

J. Schuster, R. Köhn, M. Döblinger, A. Keilbach, H. Amenitsch, T. Bein
In Situ SAXS Study on a New Mechanism for Mesostructure Formation of Ordered Mesoporous Carbons: Thermally Induced Self-Assembly
J. Am. Chem. Soc. *134 (27),* 11136-11145 (2012)
Highlighted in: Science (Editors Choice by Phil Szuromi), Science 2012, 337 (6092), 270

F. Spieckermann, G. Polt, H. Wilhelm, M. Kerber, E. Schafler, M.J. Zehetbauer
The role of dislocations for the plastic deformation of semicrystalline polymers as investigated by multireflection X-ray line profile analysis
Journal of Applied Polymer Science 125 (6), 4150-4154 (2012)

A. Steiner, P. Szekely, O. Szekely, T. Dvir, R. Asor, N. Yuval-Naeh, N. Keren, E. Kesselman, D. Danino, R. Resh, A. Ginsburg, V. Guralnik, E. Feldblum, C. Tamburu, M. Peres, U. Raviv
Entropic Attraction Condenses Like-Charged Interfaces Composed of Self-Assembled Molecules
Langmuir **2012,** 28, (5), 2604-2613

L. Suber and G. Campi
Hierarchic self-assembling of silver nanoparticles in solution
Nanotechnology Reviews 1 (1), 57–78 (2012)

P. Szekely, R. Asor, T. Dvir, O. Szekely, U. Raviv
Effect of Temperature on the Interactions between Dipolar Membranes
Journal of Physical Chemistry B **2012,** 116, (11), 3519-3524

P. Szuromi
Hot Templating (Editors' Choice)
Science, Vol. 337 - 6092, pp. 270-270 (2012)

A. Turković, P. Dubček, M. Rakić, M. Lončarić, B. Etlinger, S. Bernstorff *SAXS/DSC/WAXD study of TiO2 nanoparticles and the effect of γ-radiation on nanopolymer electrolyte*
Vacuum, Vol. 86 - 6, pp. 750-753 (2012)

A. Turkovic, P. Dubcek , K. Juraic, S. Bernstorff
SAXS/DSC/WAXD Study of Temperature Evolution in Nanocomposite Polymer Electrolytes with Different Nanofillers
Journal of Nanoscience and Nanotechnology, Vol. 12 - 11, pp. 8686-8689 (2012)

V. Valeš, V. Holý, M. Buljan, V. Janicki, S. Bernstorff
Structural and morphological properties of Fe2O3/TiO2 nanocrystals in silica matrix
Thin Solid Films 520 (14), pp. 4800-4802 (2012)

E. M. F. Vieira, J. Martín-Sánchez, A. G. Rolo, A. Parisini, M. Buljan, I. Capan, E. Alves, N. P. Barradas, O. Conde, S. Bernstorff, A. Chahboun, S. Levichev, and M. J. M. Gomes
Structural and electrical studies of ultrathin layers with $Si_{0.7}Ge_{0.3}$ *nanocrystals confined in a* $SiGe/SiO_2$ *superlattice*
Journal of Applied Physics, Vol. 111 (10), art. no. 104323, 9 pages (2012)

A. Yaghmur, M. Rappolt
Structural characterization of lipidic systems under nonequilibrium conditions
European Biophysics Journal, Vol. 41 - 10, pp. 831-840 (2012)

A. Yaghmur, M. Rappolt, J. Oøstergaard, C. Larsen, S.W. Larsen
Characterization of bupivacaine-loaded formulations based on liquid crystalline phases and microemulsions: The effect of lipid composition
Langmuir 28 (5), pp. 2881-2889 (2012)

A. Yaghmur, B. Sartori and M. Rappolt
Self-Assembled Nanostructures of Fully Hydrated Monoelaidin-Elaidic Acid
and Monoelaidin-Oleic Acid Systems
Langmuir 28, 10105-10119 (2012)

J. Zupanc, D. Drobne, B. Drasler, J. Valant, A. Iglic, V. Kralj-Iglic, D. Makovec, M. Rappolt, B. Sartori, K. Kogej
Experimental evidence for the interaction of C-60 fullerene with lipid vescicle membranes
Carbon 50 (3), pp. 1170-1178 (2012)

Publications January to Aug 2013

I. Andreou, H. Amenitsch, V. Likodimos, P. Falaras, P.G. Koutsoukos, E. Leontidis
Organized silica films generated by evaporation-induced self-assembly as hosts for iron oxide nanoparticles
Materials, Vol. 6 - 4, 1467-1484 (2013)

L. Bonaccorsi, P. Calandra, H. Amenitsch, E. Proverbio and D. Lombardo
Growth of fractal aggregates during template directed SAPO-34 zeolite formation
Microporous and Mesoporous Materials, Vol. 167, pp. 3-9 (2013)

L. Bonaccorsi, P. Calandra, M.A. Kiselev, H. Amenitsch, E. Proverbio, D. Lombardo
Self-assembly in poly(dimethylsiloxane)-poly(ethylene oxide) block copolymer template directed synthesis of linde type A zeolite
Langmuir, Vol. 29 - 23, pp. 7079-7086 (2013)

M. Buljan, N. Radić, M. Ivanda, I. Bogdanović Radović, M. Karlusic, J. Grenzer, S. Prucnal, G. Dražić, G. Pletikapić, V. Svetličić, M. Jerčinović, S. Bernstorff, V. Holy
Ge quantum dot lattices in Al_2O_3 *multilayers*
Journal of Nanoparticle Research 15 (3), article number 1485, 13 pages (2013)

M. Buljan, O. Roshchupkina, A. Šantić, V. Holý, C. Beahtz, A. Mücklich, L. Horák, V. Valeš, N. Radić, S. Bernstorff, J. Grenzer
Growth of a three-dimensional anisotropic lattice of Ge quantum dots in an amorphous alumina matrix
Journal of Applied Crystallography, Vol. 46, pp. 709-715 (2013)

G. Cordoyiannis, V.S.R. Jampani, S. Kralj, S. Dhara, V. Tzitzios, G. Basina, G. Nounesis, Z. Kutnjak, C.S.P. Tripathi, P. Losada-Perez, D. Jesenek, C. Glorieux, I. Muševič, A. Zidanšek, H. Amenitsch and J. Thoen
Different modulated structures of topological defects stabilized by adaptive targeting nanoparticles
Soft Matt. **9 (15)**, 3956-3964 (2013)

L.F. Dumée, K. Sears, B. Marmiroli, H. Amenitsch, X. Duan, R. Lamb, D. Buso, C. Huynh, S. Hawkins, S. Kentish, M. Duke, S. Gray, P. Innocenzi, A.J. Hill and P. Falcaro
A high volume and low damage route to hydroxyl functionalization of carbon nanotubes using hard X-ray lithography
Carbon, Vol. 51 - 1, pp. 430-434 (2013)

S. Haviar, M. Dubau, I. Khalakhan, M. Vorokhta, I. Matolinova, V. Matolin, V. Vales, J. Endres, V. Holy, M. Buljan, S. Bernstorff
X-ray small-angle scattering from sputtered CeO2/C bilayers
Journal of Applied Physics 113 (2), article 024301, 7 pages (2013)

M. Lučić Lavčević, P. Dubček, S. Bernstorff, M. Pavlović, and L. Šilović
A Grazing-Incidence Small-Angle X-Ray Scattering View of Vertically Aligned ZnO Nanowires
Journal of Nanomaterials, Volume 2013 (2013), Article ID 381519, 9 pages,

S.S. Mandal, B. Nagarajan, H. Amenitsch, A.J. Bhattacharyya.
Probing hemoglobin confinement inside submicron silica tubes using synchrotron SAXS and electrochemical response
European Biophysics Journal, Vol. 42 - 5, pp. 371-382 (2013)

S. Manso, F. Cacho-Nerin, R. Becerril, C. Nerin
Combined analytical and microbiological tools to study the effect on Aspergillus flavus *of cinnamon essential oil Contained In Food packaging*
Food Control 30 (2), 370–378 (2013)
10.1016/j.foodcont.2012.07.018

P. Pandit, A. Gupta, D. Kumar, M. Banerjee and S. Bernstorff
Effect of confinement on melting behaviour of cadmium arachidate Langmuir-Blodgett multilayer
Langmuir, 2013, *29* (12), pp 3950–3956

B. Pivac, P. Dubček, I. Capan, H. Zorc, Jasna Dasović, S. Bernstorff, M. Wu, B. Vlahovic
GISAXS study of Si nano structures in SiO_2 matrix for solar cell applications
Physica Status Solidi A 210 No. 4, 755-759 (2013)

M. Rappolt, F. Cacho-Nerin, C. Morello, A. Yaghmur
How the chain configuration governs the packing of inverted micelles in the cubic Fd 3 m-phase
Soft Matter 9, 6291-6300 (2013)

M. Rittman, H. Amenitsch, M. Rappolt, B. Sartori, B.M.D. O'Driscoll and A.M. Squires
Control and Analysis of Oriented Thin Films of Lipid Inverse Bicontinuous Cubic Phase using Grazing Incidence Small Angle X-ray Scattering
Langmuir, **2013**, *29* (31), pp 9874–9880

K. Salamon, O. Milat, N. Radić, P. Dubček, M. Jerčinović and S. Bernstorff
Structure and morphology of magnetron sputtered W films studied by X-ray methods
J. Phys. D: Appl. Phys. **46** (2013) 095304 (10pp)

A. Turković, P. Dubček, K. Juraić, S. Bernstorff, M. Buljan
Study of polymer electrolyte for Zn rechargeable nanostructured galvanic cells via combined in situ SAXS/DSC/WAXD measurements
American Journal of Nanoscience and Nanotechnology; 1(1), 6-10, (2013)

International Conferences and Workshops in 2012

N. Akhtar, T. T. M. Palstra, and P. Rudolf
Ultra-Thin Molecular based Conductors and Conducting Magnets
International workshop on Spintronics and Moltronics, Groningen, The Netherlands, 18-21 November 2012 (invited talk)

H. Amenitsch
The Austrian SAXS beamline - at the interface between nano & bio
Seminar, Elettra-Sincrotrone Trieste, Trieste, Italy, 2.3.12 (Lecture)

H. Amenitsch
SAXS Beamline@ ELETTRA & Institute of Biophysics and Nanosystems Research (IBN)
C-Eric Meeting, Airport Munich, Germany, 26.3.12 (Lecture)

H. Amenitsch
Small Angle Scattering
Workshop "From Genes to Atomic Structures: an Introduction to Synchrotron-Based Structural Biology", ICTP, Trieste, Italy, 23 - 27 April 2012 (Lecture)

H. Amenitsch
The Collaboration Program between the Austrian Academy of Sciences and Elettra
SAC Meeting of Elettra-Sincrotrone Trieste, Basovizza, Italy, 18.6.12 (talk)

H. Amenitsch
Simultaneous small and wide angle scattering – the in-situ tool for nano-scale materials
NANO2012, Rhodos, Greece 26-31.08.2012 (talk)

H. Amenitsch, B. Marmiroli, F. Cacho-Nerin, B. Sartori, K. Jungnikl, I. Shyjumon, P. Laggner and M. Rappolt
Self Assembly of Mesoporous Materials in the Gas-Phase: An in-situ SAD Study
62nd Annual Meeting of the Austrian Physical Society, University of Graz, Austria, 18.-21.9.2012 (Invited talk)

H. Amenitsch
The Outstation at "ELETTRA in Trieste"
NAWI Graz Tag, Graz, Austria, 2.10.2012 (talk)

H. Amenitsch
Small Angle Scattering, Synchrotron and Peter Laggner - The story behind
Farewell-IBN-Symposium, Graz, Austria, 19.10.2012 (talk)

H. Amenitsch
Materialforschung an der Österreichischen Außenstelle der Synchrotronquelle ELETTRA
Berufungsvortrag, Technical University of Graz, Austria, 07.11.2012 (talk)

H. Amenitsch
Exploring the self-assembly of mesoporous materials in the gas-phase in situ
Small Angle Scattering Conference SAS2012, Sydney, Australia, 18.11.12, 2012 (talk)

H. Amenitsch
The Austrian SAXS beamline - at the interface between bio- and nano
Science@CERIC, Trieste, Italy, 11.12.2012 (invited talk)

H. Amenitsch
The Austrian SAXS beamline and ELETTRA
Seminar Festkörperphysik, TU Graz, Austria, 19.12.2012 (talk)

R. Asor (presentor)
RNA encapsidation by SV40-derived nanoparticles follows a rapid two-state mechanism
7th International Virus Assembly Symposium, Menorca, May 2012 (poster)

R. Asor (presentor)
RNA encapsidation by SV40-derived nanoparticles follows a rapid two-state mechanism
The Hebrew University Faculty Day, June 2012 (poster)

R. Asor (presentor)
RNA encapsidation by SV40-derived nanoparticles follows a rapid two-state mechanism
Virus Structure and Assembly, Saxtons River, Vermont, USA, June 2012 (poster)

R. Asor and A. Ginsburg (posters presented by them):
1. RNA encapsidation by SV40-derived nanoparticles follows a rapid two-state mechanism
2. SAXS data analysis tool: X+
The Nanoscience and Nanotechnology Annual Conference of the Hebrew University, Kibbutz Hagoshrim, June, 2012 (posters)

R. Asor and A. Ginsburg (posters presented by them):
1. *RNA encapsidation by SV40-derived nanoparticles follows a rapid two-state mechanism*
2. *SAXS data analysis tool: X+*
The first HUJI-UK Nano-Life Workshop, the Hebrew University, June, 2012 (posters)

A.J. Bhattacharyya
Prospect of neutron in soft matter
DAE-BRNS-Theme Meeting on Neutron Scattering Science and Application, Mumbai, India, March 12-13, 2012 (Oral Presentation)

A.J. Bhattacharyya
Porous inorganic materials as sensors and encapsulators for biologically relevant molecules
2nd Discussion Meeting of Indo-French International Associated Laboratory on Solid State Chemistry, Bangalore, India, July 3-4, 2012 (Oral Presentation)

S. Bernstorff, KC.Sekhar, S.Levichev, O.Karzazi, M. Buljan, A. Chahboun, A. Almeida, J. Agostinho Moreira, M.J.M. Gomes
Correlation between structural and optoelectronic properties of ZnO nanocrystals in Alumina matrix
JVC-14 / EVC-12 / AMDVG-11 / CroSloVM-19, Dubrovnik, Croatia, 4-8 June 2012
(talk 20 min)

S. Bernstorff, M. Buljan, N. Radic, I. Bogdanovic-Radovic, and V. Holy
GISAXS analysis of quantum dot lattices
15th International Small-Angle Scattering Conference SAS2012, 18-23 November 2012, Sydney, Australia (talk)

S. Bernstorff, M. Erceg, D. Jozić, S. Perinović and I. Banovac
Analysis of melt intercalated poly(ethylene oxide)/montmorillonite nanocomposites
15th International Small-Angle Scattering Conference SAS2012, 18-23 November 2012, Sydney, Australia (poster)

S. Bernstorff, P. Dubček, B. Pivac and N. Radić
Germanium nitride quantum dots formation by nitrogen assisted sputtering
15th International Small-Angle Scattering Conference SAS2012, 18-23 November 2012, Sydney, Australia (poster)

S. Bernstorff, D. Gracin, K. Juraić, P. Dubček and M. Čeh
The structural and optical properties of amorphous-nanocrystalline silicon thin films
15th International Small-Angle Scattering Conference SAS2012, 18-23 November 2012, Sydney, Australia (poster)

L. Bonaccorsi, P. Calandra, E. Proverbio and D. Lombardo
Porous Nanoparticles formation using a Dendrimer Template
"MAMA-HYBRIDS - Multifunctional Hybrids and Organics" Ischia (Italy), October 22-24, 2012 (poster)

M. Buljan, N. Radić, M. Ivanda, I. Bogdanović-Radović, M. Karlušić, G. Dražić, G. Pletikapić, V. Svetličić, M. Jerčinović, S. Bernstorff and V.Holý
Germanium Quantum Dots in Alumina Based Multilayers: Self-Assembly for Advanced Properties
JVC-14 / EVC-12 / AMDVG-11 / CroSloVM-19, Dubrovnik, Croatia, 4-8 June 2012 (oral)

M. Buljan, N. Radić, I. Bogdanović-Radović, M. Karlušić, S. Bernstorff, V.Holy *Formation of three dimensional quantum dot lattices in amorphous systems*
EMRS Fall meeting, Warsaw, Poland, September 19-21.2012 (invited talk)

M. Buljan, C. Baehtz, V. Holý, N. Radić, O. Roshchupkina, S. Prucnal, A. Muecklich, V. Valeš, S. Bernstorff and J. Grenzer
Manipulation of Ge quantum dot ordering in alumina matrix by deposition conditions
76. Jahrestagung der DPG und DPG-Frühjahrstagung, TU Berlin, Berlin, 25. - 30. March 2012 (talk)

F. Cacho-Nerin
Microfluidics as driver for beamline development
Seminar talk at Diamond Light Source, UK, 30.5.2012

F. Cacho-Nerin,
Recent research relevant to high-throughput SAXS activities
Seminar talk at Diamond Light Source, UK, 30.5.2012

C. Carboni, D. Carboni, D. Jozic, S. Bernstorff and M. Rappolt
Synchrotron X-ray investigation of the layer spacing in a series of low molar mass bi-mesogen organosiloxane smectic materials
24th International Liquid Crystal Conference, August 19th - 24th 2012, Mainz, Germany (poster*)*

M. De March
Structural studies on the RecJCDC45 archaeal protein
ESMAX School - EMBL Hamburg, Germany, November 2012 (poster)

Y. Dong, H. Amenitsch, M. Rappolt, A. Tilley, and B. Boyd
Effect of surfactants on the internal structure and solubilization of cubosomes and hexosomes
15th International Small-Angle Scattering Conference SAS2012, 18-23 November 2012, Sydney, Australia

P. Dubček, B. Pivac, N. Radic and S. Bernstorff
Nitrogen assisted formation of Germanium Nitride Quantum dots
JVC-14 / EVC-12 / AMDVG-11 / CroSloVM-19, Dubrovnik, Croatia, 4-8 June 2012 (poster)

D. Gracin; K.Juraić; P.Dubček; A.Marinović; S. Bernstorff; A. Lausi; D. Balzar; M.Čeh
The properties of amorphous-nanocrystalline silicon thin films for next generation of solar cells
JVC 14, EVC 12, AMDVG 11, CROSLOVM 18, Dubrovnik, Croatia, June 4-8, 2012 (oral)

D. Gracin, K. Juraić, A. Gajović, S. Bernstorff, V. Tudić, M. Čeh
Amorphous-nanocrystalline silicon thin films for single and tandem solar cells
Photovoltaic Technical Conference-Thin Film &Advanced Silicon Solutions 2012, Aixen, France, June, 6-8, 2012 (poster)

J. Grenzer, M. Buljan, V. Holý, C. Baehtz· L. Horák, S. Bernstorff, N. Radić
In-situ real-time observation of the self-assembled growth of ordered germanium nanocrystals embedded within a dielectric matrix
Xtop 2012 (The 11th Biennial Conference on High Resolution X-Ray Diffraction and Imaging), Saint-Petersburg, Russia, September 15-20, 2012 (oral)

J. Grenzer, M. Buljan, O . Roshchupkina, C. Baehtz, V. Holy
In-situ observation of the self-assembled growth of ordered Ge nanocrystals embedded within a dielectrical matrix
DPG Berlin, Germany, 25-30.03. 2012 (oral)

P. Heftberger, B. Kollmitzer, M. Rappolt and G. Pabst
Temperature Behavior of Physical Properties of Coexisting Lipid Domains
Biomembrane Days, Potsdam, Germany, 19.-21. 09. 2012

V. Holy
Synchrotron-related methods for investigation of nanostructures
Winter School of Synchrotron Radiation, Liptovský Ján, Slovakia, 31.1. – 4.2. 2012

P. Innocenzi
Sel-assembled thin films with hierarchical porosity
I. Japan-Italy Workshop on Sol-Gel for Advanced Functional Materials, , Osaka, Japan, 9.2.2012

S. Joseph, M. Rappolt & H. Bunjes
Simultaneous synchrotron X-ray diffraction/DSC studies on the polymorphic transitions in solid triglyceride drug carrier nanoparticles
8. World Meeting on Pharmaceutics, Biopharmaceutics and Pharmaceutical Technology,, Istanbul (Turkey), 19.-22.03.2012 (Poster)

D. Jozic, Sinisa Zorica and S. Bernstorff
Insitu SAXS/WAXS study of the developing process of geopolymer structures
15th conference on "Composite material", Venice, Italy, June 24-28, 2012

D. Jozić, M. Lučić-Lavčević, M. Erceg, S. Perinović, S. Bernstorff
Simultaneous insitu SAXS/WAXS study of processes and products of geopolymerization
15th International Small-Angle Scattering Conference SAS2012, 18-23 November 2012, Sydney, Australia (poster)

O. Karzazi, K.C. Sekhar, S. Levichev, M. Buljan, S. Doyle, S. Bernstorff, D. Czekaj, A. Chahboun, M.J.M. Gomes
Effect of Co doping on structural and electrical properties of ZnO nanocrystals embedded on alumina matrix
ELSPEC 2012, (la 5ème Conférence francophone sur les spectroscopies d'électrons), Louvain-la-Neuve, Belgium, 22.-25. 5.2012

G. Khelashvili, M. P. Rappolt, S.-W. Chiu, G. Pabst and D. Harris
Impact of sterol tilt on membrane bending rigidity in cholesterol and
7DHC-containing DMPC membrane
56th Annual Meeting of the Biophysical Society, San Diego, USA, 25.02.2012 (invited talk)

S. Kler, R. Asor, C.L. Li, A. Ginsburg, D. Harries, A. Oppenheim, A. Zlotnick, U. Raviv
RNA Encapsidation by SV40-Derived Nanoparticles Follows a Rapid Two-State Mechanism
15th International Small-Angle Scattering Conference SAS2012, Sydney, Australia, 18-23 November 2012 (talk)

B. Kollmitzer, P. Heftberger, M. Rappolt, and G. Pabst
Structure and Elasticity of Liquid Ordered Lipid Domains
EBSA Biophysics Course, Bordeaux, France, 24.-29. 06. 2012

B. Kollmitzer, P. Heftberger, M. Rappolt, and G. Pabst
Structure and Elasticity of Liquid Ordered Lipid Domains
Biomembrane Days, Potsdam, Germany, 19.-21. 09. 2012

K. Kornmueller
Can amphiphilic designer peptides act as detergents?
PhD Seminar, Graz, Austria, 11. 05. 2012 (talk)

K. Kornmueller
Can amphiphilic designer peptides act as detergents?
EBSA Biophysics Course on: Membrane Biophysics & Lipid/Protein Interaction, Bordeaux-Lacanau, France, 24.-29. 6. 2012 (talk)

K. Kornmueller, C. Vonach, F. Cacho-Nerin, C. Mikl, H. Amenitsch and R. Prassl
Membrane Activity of Amphiphilic Designer-Peptides
DocDay 8, Graz, Austria, 13.7.2012 (poster)

K. Kornmueller, C. Vonach, F. Cacho-Nerin, C. Mikl, H. Amenitsch and R. Prassl
Membrane Activity of Surfactant-Like Designer-Peptides
ÖGMBT Annual Meeting 2012, Graz, Austria, 17.-19. 9. 2012 (poster)

K. Kornmueller, C. Vonach, F. Cacho-Nerin, C. Mikl, H. Amenitsch and R. Prassl
Surfactant-Like Designer Peptides as Solubilizing Agents for Apolipoprotein B-100
11th Greta Pifat-Mrzljak International School of Biophysics, Biomacromolecular Complexes and Assemblies, Primošten, Croatia, Sep 29-Oct 9, 2012 (poster)

K. Kornmueller, C. Vonach, F. Cacho-Nerin, K. Gradauer, G. Leitinger, H. Amenitsch and R. Prassl
Helical properties of an amphiphilic designer-peptide
7th Christmas Biophysics Workshop (XBW 2012), Riegersburg, Austria, 17. – 18. 12. 2012 (talk)

M. Kriechbaum
Small-Angle X-ray Scattering (SAXS): A modern tool in nanostructure research
School of Chemical and Mathematical Sciences, Murdoch University, Perth, Australia, 14.11.2012 (talk)

M. Kriechbaum, M. Rappolt and P. Laggner
A novel laboratory-based instrument combining SAXS/WAXS and microcalorimetry
SAS2012: International Small-Angle Scattering Conference, Sydney, Australien,
November 2012 (poster)

P. Laggner, H. Amenitsch and M. Kriechbaum
Quality factor in SAXS instrumentation
SAS2012: International Small-Angle Scattering Conference, Sydney, Australien,
November 2012 (talk)

R.T. Lechner
Colloidal Functional Nanoparticles and Nanocrystal Solids: Structural Impact on Magnetism and Optics
Seminar on Semiconductor and Solid State Physics, Nov. 11 (2012), Institute of Semiconductor and Solid State Physics, JKU Linz, Austria (talk)

E. Lepeltier, C. Bourgaux, J. Caron, E. Sliwinski, D. Desmaële, A. Maksimenko, P. Couvreur
Nanoassemblies of nucleoside analogues coupled to squalene: Structural analysis
8th PBP World Meeting, Istanbul, Turkey, 19-22 March 2012

E. Lepeltier, C. Bourgaux, V. Rosilio, E. Sliwinski, F. Zouhiri, S. Lepêtre-Mouelhi, D. Desmaële, P. Couvreur
Supramolecular organization of nucleoside analogues coupled to terpenoids : an original platform for drug delivery
AAPS Annual Meeting and Exposition, Chicago, USA, 12-14 october 2012

E. Lepeltier, C. Bourgaux, J. Caron, E. Sliwinski, D. Desmaële, A. Maksimenko, P. Couvreur
Nanoassemblies of nucleoside analogues coupled to squalene: Structural analysis ICOMF14, Paris, France, 10-13 July 2012 (oral communication)

D. Lombardo
Branched Polymer Nanosystems: Interaction in solution and applications
"SOLEIL Users' Meeting 2012" École Polytechnique Palaiseau, (France) January 18th - 19th, 2012 (talk)

M. Loncaric, H. Zorc and J. Sancho-Parramon
Thin copper films on glass substrates produced by e-beam evaporation - optical properties and structure
JVC-14 / EVC-12 / AMDVG-11 / CroSloVM-19, Dubrovnik, Croatia, 4-8 June 2012 (poster)

M. Lucic Lavcevic, S. Bernstorff, P. Dubcek, L. Silovic
Simultaneous GISAXS/GIXD measurements of nanostructures in ZnO thin films
JVC-14 / EVC-12 / AMDVG-11 / CroSloVM-19, Dubrovnik, Croatia, 4-8 June 2012 (poster)

L. Malfatti
Combined top-down and bottom-up approach for the design of functional nanostructures
I. Japan-Italy Workshop on Sol-Gel for Advanced Functional Materials, , Osaka, Japan, 9.2.2012

L. Malfatti
Hierarchical Porous thin films
Eurasia Conference on Chemical Science, Corfù, Greece, 16-21.4.2012

L. Malfatti
A combined bottom-up and top-down approach towards the design of thin films on multiple length scales
IV. FORUM Nazionale dei Giovani Ricercatori di Scienza e Tecnologia dei Materiali, Padova, Italy, 28-30.5.2012

L. Malfatti
Mesoporous ordered thin films: the templating approach and functional properties
Symposium on "Bottom-up and Top-down Approaches for the design of Advanced Nanomaterials", Melbourne (Australia) 17.6.2012

S.S. Mandal, A.J. Bhattacharyya
Synchrotron SAXS and electrochemical response of hemoglobin confined within organic and inorganic matrices
12th International Conference on Surface X-ray and Neutron Scattering (SXNS-12), Kolkata, India, July 25-28, 2012 (Poster Presentation)

B. Marmiroli, F. Cacho-Nerin, B. Sartori, J. Perez, H. Amenitsch
Quantitative analysis of liquid jets breakup with SAXS
ÖPG Tagung 2012, 18-21.9.2012, Graz, Austria (invited talk)

B. Marmiroli
Microfluidics for nanoanalytic techniques
University of Nova Gorica, Graduate School-Environmental Sciences Study Programme, Gorizia (Italy), 08/11/2012 (invited lecture)

B. Marmiroli, F. Cacho-Nerin, B. Sartori, P. Falcaro, Luca Malfatti, G. Grenci, M. Faustini, S. Costacurta, D. Grosso, P. Innocenzi, and H. Amenitsch
Combining X-ray lithography and small angle X-ray scattering for biology and material science
MNE 2012 (Micro Nano Engineering Conference), 16-20.9.2012, Toulous, France (talk)

B. Marmiroli, H. Amenitsch
What can be obtained by bringing together small angle X-ray scattering and deep X-ray lithography?
ÖPG Tagung 2012, 18-21 september, Graz, Austria (talk)

B. Marmiroli, F. Cacho Nerin, B. Sartori, J. Perez and H. Amenitsch
Analysis of the breakup of liquid jets in air by SAXS
SAS 2012, International Small-Angle Scattering Conference, Sidney, Australia, November 2012 (poster)

B. Marmiroli and H. Amenitsch
SAXS and deep X-ray lithography for material science and biology
SAS 2012, International Small-Angle Scattering Conference, Sidney, Australia, November 2012 (poster)

B. Marmiroli
SAXS + Deep X-ray lithography = (biology + material science)!
Second Small Angle XmaS Workshop, Trieste, Italy, 14.12.2012 (talk)

J. Martin-Sanchez, M. Buljan, A.G. Rolo, E. Alves, O. Conde, S. Bernstorff, A. Chahboun, R. Serna, M.J.M. Gomes
Structural and optical studies of ordered self-assembled Ge quantum dots lattices embedded in amorphous Al_2O_3 *matrix*
E-MRS 2012 Fall Meeting, Warsaw, Poland, September 17 - 21, 2012 (oral)

S. Onesti
An integrated approach to structural biology: the interplay of MX, EM, NMR and SAXS to tackle complex biological problems
Science@C-ERIC workshop, Trieste, Italy, December 2012 (Invited Speaker)

S. Onesti
Towards an integrated approach to protein structures
SESAME 10th User meeting, Amman, Jordan, November 2012 (Invited Speaker)

S. Onesti
Using multiple techniques to tackle macromolecular complexes @ Elettra
TAC Light Sources User Meeting, Ankara, Turkey, October 2012 (Invited Speaker)

S. Onesti
An integrated structural and biochemical approach to human DNA replication
Sabanci University, Istanbul, Turkey, October 2012 (invited talk, Host: Z. Sayers)

S. Onesti
Structural and functional insights into the DNA replication factor Cdc45
Istituto di Genetica e Biologia Evoluzionistica, Naples, Italy, February 2012 (invited talk)

S. Onesti
Structural and functional insights into the DNA replication machinery
Istituto di Biochimica delle Proteine, CNR, Napoli, Italy, March 2012 (invited talk)

G. Pabst
Elastic Properties of Lipid Domains
Institute of Solid State Physics, Sofia, Bulgaria, 31.08.2012

G. Pabst
Physics of Membrane Function
7th International School on Condensed Matter, Varna, Bulgaria, 02. 09. – 07. 09. 2012

G. Pabst, B. Boulgaropoulos, B, Sartori, H. Amenitsch, and M. Rappolt
Physical control of ion-channel function in lipid domains
Meeting on "Lipid-Protein Interactions in Membranes: Implications for Health and Disease", sponsored and organized by the Biophysical Society, Hyderabad, India, 01. – 05. 11. 2012 (poster)

G. Pabst
Physics of cellular signaling
Raman Research Institute, Bangalore, India, 7. 11. 2012

P. Pandit, M. Banerjee, A. Gupta, D. Kumar and S. Bernstorff
Effect of confinement on melting behaviour of cadmium arachidate Langmuir-Blodgett Multilayer
12th International Conference on Surface X-ray and Neutron Scattering, Kolkata, India. 25- 28 July 2012

P. Parisse
Enzymatic reactions on DNA modified gold nanoparticles & other stories
The second Small Angle XmaS workshop : "SAXS applications and perspectives", Trieste, Italy, 14.12.2012 (Oral contribution)

S. R. C. Pinto, M. Roldan, Maja Buljan, S. Bernstorff, A. Chahboun, N.P. Barradas, E. Alves, S I.Molina, M. M.D. Ramos, M. J. M. Gomes
Controlling the properties of layered self-organized Ge clusters in silica matrix
EMRS Spring-Meeting, Strasbourg, France, 14.-18.5.2012

G. Polt, F. Spieckermann, H. Wilhelm, E. Schafler, M.J. Zehetbauer
Rate mechanism and dislocation generation in semicrystalline polymers
5th International Conference on Polymer Behaviour (ICPB5), Aveiro, Portugal, September 2012 (oral)

G. Polt, F. Spieckermann, H. Wilhelm, M. Kerber, E. Schafler, and M.J. Zehetbauer
E*ffects of dislocations in γ-phase polypropylene and comparison with other semi-crystalline polymers*
15th International Conference on Deformation, Yield and Fracture of Polymers (DYFP15), Kerkrade, The Netherlands, April 2012 (poster)

G. Polt, F. Spieckermann, H. Wilhelm, M. Kerber, E. Schafler and M.J. Zehetbauer
Plastic Deformation and Thermal Stability of Polyethylene-terephthalate (PET)
International Conference on Strength of Materials (ICSMA16), Bangalore, India, August 2012 (poster)

D. Pozzi, G. Caracciolo, F. Cardarelli, A. Bifone and H. Amenitsch
Confocal microscopy makes visible cholesterol-mediated gene delivery mechanisms Optics Within Life Science 2012, Genova, Italy, 4-6 July 2012

N. Radić, P. Dubček, S. Bernstorff, Z. Skoko, M. Ristić, and Z. Siketić
Structural study of Ni-Nb thin films
15th International Small-Angle Scattering Conference SAS2012, 18-23 November 2012, Sydney, Australia (poster)

M. Rappolt, K. Lohner, Y. Kaconis, T. Gutsmann & K. Brandenburg
Interactions of Novel Antibiotics with Bacterial Cell Membranes Identified by SAXS
Faraday Discussion 161, Lipids and Membrane Biophysics, Burlington House, London (UK), 11.-13.09.2012 (Poster)

M. Rappolt
X-ray scattering of bacterial cell wall compounds: the world beyond flatland
Workshop on GLYCOLIPIDS, STRUCTURES, FUNCTION AND INTERACTIONS organized by Klaus Brandenburg (Forschungszentrum Borstel) at the University of Hamburg, 25.05.2012 (Invited lecture)

M. Rappolt
What can we learn from drug/membrane interactions?
Institutes Seminar at the Forschungszentrum Borstel, Germany, 15.05.2012

M. Rappolt
Interview with *M. Rappolt* transmitted in a two-minute TV report "Unterwegs beim Nachbarn" produced by the ORF (Österreichischer Rundfunk), 29.03.2012

M. Rappolt
Synchrotron Light in Biology and Medicine
"Membrane Biophysics Course" at the University of Ljubljana, 17.01.2012 (lecture)

M. Rappolt
The power of SAXS: Exploration of the Magic World of Bio- and Nanomaterials
Workshop SUNGREEN: "Strengthen the University of Nova Gorica's REsearch Potential in Environmental Sciences and Novel Nano-materials", Ajdovscina, Slovenia,
14.11.12, 2012 (invited talk)

U. Raviv
RNA-induced assembly of SV40-derived nanoparticles is very fast and with no detectable intermediates
Nano-Israel, The 3rd International Nanotechnology Conference, March 2012

U. Raviv
RNA encapsidation by SV40-derived nanoparticles follows a rapid two-state mechanism
Israel Crystallography Society meeting, Jerusalem, May 2012

U. Raviv
Regulating the Size and Stabilization of Lipid Raftlike Domains and Using Calcium Ions as Their Probe
Seminar "Materials and Interfaces", Weizmann Institute, March 2012

U. Raviv
Intermolecular Interactions and Dynamic Structures of Biomolecular Self-Assemblies
Seminar at Nanocenter, Ben Gurion University, April 2012

U. Raviv
RNA encapsidation by SV40-derived nanoparticles follows a rapid two-state mechanism
Seminar at Israel Institute for Biological Research, May 2012

U. Raviv
Intermolecular Interactions and Dynamic Structures of Biomolecular Self-Assemblies
Seminar at Northwestern University, Material Science and Engineering department, June 2012

U. Raviv
RNA encapsidation by SV40-derived nanoparticles follows a rapid two-state mechanism
Biophysical Society 56th Annual Meeting, San Diego, USA, February 2012 (poster)

K. Salamon, O. Milat, N. Radić, P. Dubček, M. Jerčinović, S. Bernstorff
X-ray study of structure and morphology of magnetron sputtered W thin films
JVC-14 / EVC-12 / AMDVG-11 / CroSloVM-19, Dubrovnik, Croatia, 4-8 June 2012 (poster)

E. Schafler
Microstructural characterisation of deformed materials by X-ray line profile analysis
Institute of Mineralogy and Crystallography, University of Vienna, November 2012 (invited oral)

E. Schafler
Effect of hydrostatic pressure on the microstructure and mechanical properties during and after high pressure torsion
DPG-Frühjahrstagung, Berlin, März 2012

A. Schiener and A. Magerl
Ultrafast in-situ SAXS and WAXS on the Nucleation of II-VI Quantum Dots
EAM summer school, Kloster Banz, Germany, 28.6. – 30.6.12 (poster)

A. Schiener, T. Wlochowitz H. Amenitsch, A.A. Rempel, and A. Magerl
Nucleation and growth of CdS nanoparticles observed by ultrafast SAXS
SAS 2012, Sydney, Australia, 18.-23.11.12 (poster)

A. Schiener, T. Wlochowitz, S. Gerth, T. Unruh, A. Rempel, H. Amenitsch and A. Magerl
Nucleation and growth of CdS nanoparticles observed by ultrafast SAXS
MRS Fall Meeting, Boston, USA, November 25-30, 2012

W. Schmidt
Dynamics of gas adsorption on CMK-5 monitored by in-situ XRD
Conference on "Characterization of Porous Materials (CPM) VI", 30 Apr - 2
May 2012 Delray Beach, USA (talk)

KC.Sekhar, S.Levichev, O.Karzazi, S.Doyle, S. Bernstorff, O. Conde, A. Chahboun. A. Almeida, J. Agostinho Moreira, M.J.M. Gomes
Structural and optical properties of $Zn_{1-x}Co_xO$ *nanocrystals embedded in* Al_2O_3 *thin films*
EMRS Spring-Meeting, Strasbourg, France, 14.-18.5.2012

F. Spieckermann, H. Wilhelm, G Polt, E. Schafler, M. Kerber, M.J. Zehetbauer
Dislocation kinetics in plastically deformed α and γ polypropylene
5th International Conference on Polymer Behaviour (ICPB5), Aveiro, Portugal, September 2012 (oral)

F. Spieckermann, G. Polt, H. Wilhelm, M. Kerber, E. Schafler, M.J. Zehetbauer
Dislocation Contrast Factors of Semicrystalline Polymers
International Conference on Strength of Materials (ICSMA16), Bangalore, India, August 2012 (oral)

Z. Syrgiannis, A. Bonasera
Supramolecular nanostructures of ruthenium photosensitizer and polyoxometalate dyads
Nanosolar Project meeting, Padova (PD), Italy, 20.4.2012

Z. Syrgiannis, A. Sartorel, M. Carraro, H. Amenitsch, G. La Ganga, F. Puntoriero, S. Campagna, M. Bonchio, M. Prato
Supramolecular nanostructures of photosensitizer and polyoxometalate dyads: structural aspects as a driving force for new routes
FUTURMAT 2, Second International Meeting on Organic Materials for a Better Future, Brindisi, Italy, 16.-20.9.2012

C.V.Teixeira, M.C.A.Fantini, T.S.Martins, J.R.Matos, H.Amenitsch,
The form factor of cubic mesoporous sílica in FCC structure
XXXV Brazilian Meeting on Condensed Matter Physics, Águas de Lindoia, SP, Brazil, 14-18 May 2012 (Poster)

M. Torrell, A.G. Rolo, J. Sancho-Parramon, M. Buljan, I. Bogdanovic-Radovic, Z. Siketic, C. Kubel, S. Bernstorff, J.A. Santos and F. Vaz
Evolution of surface plasmon resonance of $Au:TiO_2$ *nanocomposites with annealing temperature*
E-MRS 2012 Fall Meeting, Warsaw, Poland, September 17-21, 2012

G. Trimmel, A. Fischereder, A. Schenk, E. Strunz, W. Haas, M. Edler, A. Pein, H. Amenitsch, R. Saf, F. Hofer and T. Rath
Solution Based Routes towards Copper Indium Sulfide and Copper Zinc Tin
Sulfide Layers for Photovoltaic Applications
27th European PV Solar Energy Conference and Exhibition, Frankfurt, Deutschland,
2012

F. Valle, B. Marmiroli, H. Amenitsch and R. Taccani
SAXS characterization of the catalyst layer of a HT-PEM Fuel Cell
Second Joint Doctorate Summer School on Nanotechnology, Udine, Italy, 2-5 July 2012

F. Valle, B. Marmiroli, H. Amenitsch and R. Taccani
Electron microscopy and Small-Angle X-ray Scattering analysis of the catalyst layer degradation in PBI-based HT-PEM Fuel Cells
67° Congresso Nazionale ATI, Trieste, Italy, 11-14 September 2012

F. Valle, N. Zuliani and R. Taccani
Nano-morfological analysis for PEM Fuel Cell characterization
Primo workshop italiano su celle a combustibile, Perugia, Italy, 22-23 November 2012

F. Valle, B. Marmiroli, H. Amenitsch and R Taccani
SAXS Analysis of the Catalyst Layer Degradation in Fuel Cells
2nd Small Angle XmaS workshop, Elettra, Trieste, Italy, 14 December 2012

E.M.F.Vieira, J. Martín-Sánchez, S. Levichev, M. Buljan, S. Bernstorff, M. A. Roldan, A.G. Rolo, A. Chahboun, S.I. Molina, M. Varela, S. J. Pennycook, M.J.M. Gomes
Evidence of self-organized $Si_{1-x}Ge_x$ *nanoparticles in* Al_2O_3 *multilayer structure*
EMRS Spring-Meeting, Strasbourg, France, 14.-18.5.2012 (15 min talk)

E.M.F.Vieira, S. Pinto, J. Martín-Sánchez, S. Levichev, M. Buljan, S. Bernstorff, M. A. Roldan, S.I. Molina, I. Capan, A.G. Rolo, O. Conde, A. Chahboun, E. Alves, N. Barradas, M.J.M. Gomes
SiGe and Ge nanocrystals embedded in dielectrics for carrier's retention application
EMRS Spring-Meeting, Strasbourg, France, 14.-18.5.2012 (poster)

H. Wilhelm, F. Spieckermann, Gerald Polt, Erhard Schafler, M.J. Zehetbauer
Modified Williamson Hall analysis - a powerful method for the determination of microstructural parameters of semi-crystalline polymers
5th International Conference on Polymer Behaviour (ICPB5), Aveiro, Portugal September 2012 (invited oral)

H. Wilhelm, F. Spieckermann, G. Polt, M. Zehetbauer
Physikalische Modellvorstellungen zur Beschreibung des mechanischen Verhaltens von teilkristallinen Polymeren
4a Technologietag 2012 „Kunststoffe auf dem Prüfstand“, Schladming, Austria, February 2012 (oral)

A. Yaghmur, B. Sartori & M. Rappolt
Self-assembled nanostructures of fully hydrated monoelaidin-elaidic acid and monoelaidic-oleic acid systems
ECIS 2012, 26th Conference of the European Colloid and Interface Society, Malmö (Sweden), 2.-7.09.2012 (Poster)

M.J. Zehetbauer, F. Spieckermann, G. Polt, H. Wilhelm, M. Kerber, S. Bernstorff, E. Schafler
Multiple Whole X-Ray Line Profile Analyses for investigating the role and nature of dislocations in plastic deformation of semicrystalline polymers
TMS Annual Meeting & Exhibition, Orlando (Florida), USA, March 2012 (invited oral)

ELETTRA Highlights 2011-2012

J. Schuster, R. Köhn, M. Döbl inger, A. Keilbach, H. Amenitsch and Th. Bein
In Situ SAXS Study on a New Mechanism for Mesostructure Formation of Ordered Mesoporous Carbons: Thermally Induced Self-Assembly
Elettra Research Highlight, pp. 34-35 (2011-2012)

G. Caracciolo, D. Pozzi, A. L. Capriotti, C. Cavaliere, P. Foglia, H. Amenitsch and A. Laganà
Evolution of the protein corona of lipid gene vectors as a function of plasma concentration
Elettra Research Highlight, pp. 98-99 (2011-2012)

I. Krastanova, V. Sannino, H. Amenitsch, O. Gileadi, F.M. Pisani and S. Onesti
Structural insights into the human DNA replication factor Cdc45 using small angle x ray scattering
Elettra Research Highlight, pp. 100-101 (2011-2012)

Contributions to "communicate science in public"

"Lange Nacht der Forschung" - an open day at Austrian research facilities, IBN, Graz, Austria, and Outstation (SAXS-beamline at Elettra), Trieste, Italy, 27.04.2012 (presentations life from the members of the SAXS beamline to Graz by connection via Skype).

SAXS training courses

The **second Tutorial of "Advanced Synchrotron Techniques at ELETTRA (AST 2)**", for 20 students from the Montan University of Leoben, Austria, was performed at several beamlines of ELETTRA (Basovizza, Italy) during 19+20.3.2012. This course was organized by Heinz Amenitsch (Austrian Academy of Science), Oskar Paris (Montan University Leoben, Austria), and Sigrid Bernstorff (Elettra-Sincrotrone Trieste).

During the first day, the students followed a general presentation of the Elettra-Sincrotrone given by Luca Gregoratti, and got a tour (guided by Stefano Cleva) of ELETTRA and the free electron laser FERMI. Afterwards, the students visited several beamlines.

The second day of the course was dedicated to tutorials and "hands-on experimental experience" on 5 different beamlines: SAXS, DXRL, XAFS, XRD, SISSI. There, the following persons contributed to the success of this initiave: Heinz Amenitsch, Sigrid Bernstorff, Michael Rappolt, Fernando Cacho (SAXS), Benedetta Marmiroli, Andrea Allemandi (DXRL), Luca Olivi, Antonella Iadecola, Sameh Ahmed (XAFS), Nicola Demitri, Giorgio Bais (XRD), Andrea Perucchi, Diana Bedolla, Paolo Ferraris (SISSI).

The **“School on Synchrotron and Free-Electron-Laser Sources and their Multidisciplinary Applications"** was organized during 19-30.3.2012 by the International Center for Theoretical Physics (ICTP, Trieste), the Sincrotrone Trieste and the International Atomic Energy Agency (IAEA).

45 PhD students, postdocs and also experienced researches participated, coming from all over the world. Regarding the SAXS technique, Peter Laggner gave a lecture, while introductions into the SAXS beamline and "practical experimental experience" were given by Heinz Amenitsch, Sigrid Bernstorff and Michael Rappolt.

PhD Thesis / Doktorarbeiten 2012

Dimitris Doudaniotis
Conformational study of antihypertensive drugs and their interactions with lipid bilayers using physicochemical methodologies
University of Patras, Greece

K.Juraić
Amorphous-nano-crystalline thin films: structure and optical properties
University of Zagreb, Croatia

Alessandra Mari
Synthesis of functional magnetic nanoparticles for catalytic applications
University of Rome "La Sapienza", Italy

Francesca Marino
Structural and functional characterization of human RecQ helicases
Scuola Normale Superiore, Universita' di Pisa, Italy

Tri Truong Cong
Innovative compartmented nanoparticles for quercetin administration
Université Paris-Sud, France

Master Theses (Tesi di Laurea, Diplomarbeit) 2012

Elena Marcassa
Analisi strutturale e biochimica della proteina umana MCM10
University of Trieste, Italy

Italia Peschiera
Studi Strutturale e funzionali della proteina MCM10 di S. cerevisiae
University of Trieste, Italy

Francesco Valle
SAXS characterization of a HT-PEMFC Membrane Electrolyte Assembly
University of Trieste, Italy

Authors Index

SCIENCE ▪ PASSION ▪ TECHNOLOGY

TU Graz

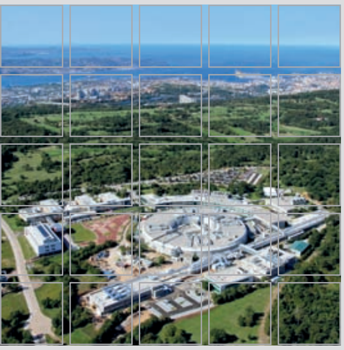
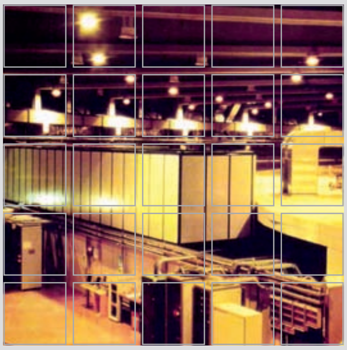
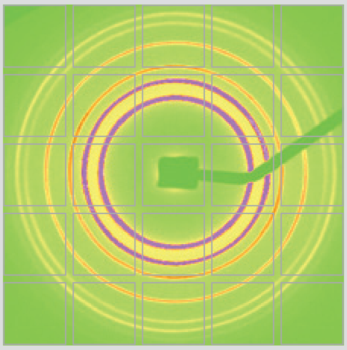
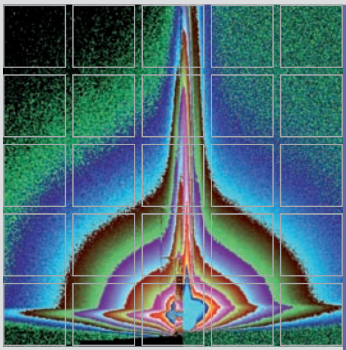
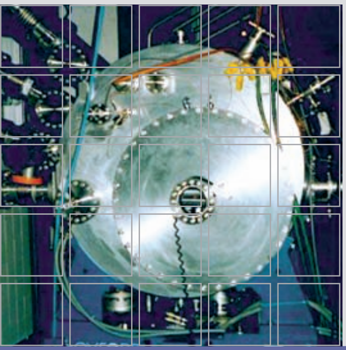

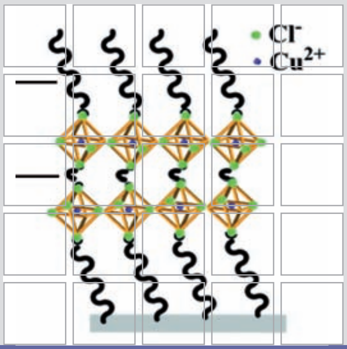

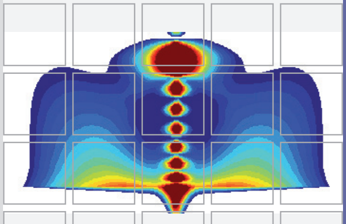

Institute of Inorganic Chemistry
Graz University of Technology
Faculty of Technical Chemistry,
Chemical and Process Engineering,
Biotechnology – TCVB
Stremayrgasse 9/IV, 8010 Graz, Austria
Tel.: +43 316 873 32145
Fax: +43 316 873 32102
E-mail: amenitsch@tugraz.at
Web: http://ac.tugraz.at

Austrian SAXS Beamline
Outstation of the Institute of
Inorganic Chemistry
Graz University of Technology
c/o Elettra-Sincrotrone Trieste
Strada Statale 14, km 163.5
34149 Basovizza (TS) Italy
E-mail: amenitsch@tugraz.at

Elettra Sincrotrone Trieste

Elettra-Sincrotrone Trieste
Strada Statale 14, Km 163,5
34149 Basovizza (TS), Italy
Tel.: +39 040 375 8572
Fax: +39 040 9380 902
E-mail: bernstorff@elettra.eu
Web: www.elettra.eu

ÖAW Austrian Academy of Sciences

IBN INSTITUTE OF BIOPHYSICS AND NANOSYSTEMS RESEARCH

Former:
Institute of Biophysics and
Nanosystems Research
Austrian Academy of Sciences
Schmiedlstraße 6, 8042 Graz, Austria